5-2014

A Computational Fluid Dynamics Validation Experiment for Forced and Mixed Convection on a Vertical Heated Plate

Jeff Robert Harris
Utah State University

Recommended Citation

Harris, Jeff Robert, "A Computational Fluid Dynamics Validation Experiment for Forced and Mixed Convection on a Vertical Heated Plate" (2014). *All Graduate Theses and Dissertations*. 2792.
https://digitalcommons.usu.edu/etd/2792

A COMPUTATIONAL FLUID DYNAMICS VALIDATION EXPERIMENT FOR FORCED AND MIXED CONVECTION ON A VERTICAL HEATED PLATE

by

Jeff Robert Harris

A dissertation submitted in partial fulfillment
of the requirements for the degree

of

DOCTOR OF PHILOSOPHY

in

Mechanical Engineering

Approved:

Dr. Barton L. Smith Major Professor	Dr. Robert Spall Committee Member
Dr. Heng Ban Committee Member	Dr. Aaron Katz Committee Member
Dr. Blake Tullis Committee Member	Dr. Mark R. McLellen Vice President for Research and Dean of the School of Graduate Studies

UTAH STATE UNIVERSITY
Logan, Utah

2014

Abstract

A Computational Fluid Dynamics Validation Experiment for Forced and Mixed
Convection on a Vertical Heated Plate

by

Jeff Robert Harris, Doctor of Philosophy
Utah State University, 2014

Major Professor: Dr. Barton L. Smith
Department: Mechanical and Aerospace Engineering

A computational fluid dynamics (CFD) validation experiment is conducted for convection flow from a heated plate in buoyancy aided and opposed orientations. The design of the experiment to meet CFD validation completeness standards is described. Previous experiments and simulations have been completed, but none measure or present the necessary boundary conditions to define the simulation boundary conditions. Experimental measurements of forced and mixed convection are presented, along with measured boundary conditions sufficient to compute simulations for validation purposes. Some simulation results are described, but a complete validation study is not included. Simulations are conducted to ensure all necessary boundary conditions are being measured. This document and the corresponding website will provide sufficient explanation and data to repeat the experiment and speed the setup of future validation experiments. The data and boundary conditions are available for download on a website dedicated to validation data dissemination. Along with the validation data, the response quantities provide some insight into the flow characteristics of the boundary layer for convective flow from a vertical flat plate.

(192 pages)

Public Abstract

A Computational Fluid Dynamics Validation Experiment for Forced and Mixed Convection on a Vertical Heated Plate

by

Jeff Robert Harris, Doctor of Philosophy

Utah State University, 2014

Major Professor: Dr. Barton L. Smith
Department: Mechanical and Aerospace Engineering

A computational fluid dynamics (CFD) validation experiment is conducted for flow over a heated vertical plate. The design of the experiment to meet CFD validation standards is described. Many experiments and simulations have been completed in past studies, but none measure or present the necessary boundary conditions to define the simulation. Experimental measurements of heated flow are presented, along with corresponding boundary conditions sufficient to define the simulation's boundary conditions. Some simulation results are described, but a complete validation study is not included. The simulations are conducted by the experimentalist to ensure all necessary boundary conditions are being measured. This document will provide sufficient explanation and data to repeat the experiments and speed the setup of future validation experiments.

Acknowledgments

I gratefully recognize Dr. Barton Smith, Blake Lance, and Brandon Wilson for their guidance, mentoring, and continual support. My colleagues in the Experimental Fluid Dynamics Laboratory for their assistance, advice, and patience, including Scott Warner, Kyle Jones, David Reynolds, Tucker Smith, Shaun Harris, Andrew Ostler. My family for being patient with me, in spite of my impatience, thank you.

Thanks also to Utah State University for allowing me to work on the beautiful campus and in their facilities. To the Department of Mechanical and Aerospace Engineering faculty and staff, thanks for your support.

This research is being performed using funding received from the DOE Office of Nuclear Energy's Nuclear Energy University Programs and a fellowship from the Nuclear Regulatory Commission.

Jeff Harris

Contents

List of Tables

List of Figures

Notation

Lower-case Roman

c_f	The coefficient of friction.
dy	The height of the near wall cell in a CFD mesh.
e_a^{21}	The absolute relative error between the second and first refined grid.
g	The standard gravity constant, 9.81 $\mathrm{m/s^2}$.
k	The turbulence kinetic energy.
p^+	The nondimensional pressure.
r_{21}^p	The ratio of the characteristic length for the first and second grid refinements.
r_{32}^p	The ratio of the characteristic length for the second and first grid refinements.
u	The velocity component in the x direction.
$\overline{u}_\infty$	The free-stream velocity.
u^+	The nondimensional streamwise velocity.
v	The velocity component in the y direction.
w	The velocity component in the z direction.
x	The stream-wise position in the test section.
y	The position measured perpendicular from the surface of the heated plate.
y_0	The wall position.
y^+	The nondimensional distance from the plate.
z	The span-wise position normal to x and y.

Upper-case Roman

B	The intercept in the wall coordinate profiles.
C	A constant to compute Nu_f.
D_h	The hydraulic diameter of the test section.

$\mathrm{Gr_x}$	The Grashof number based on the local position x, $g\beta(T_s - T_\infty)x^3/\nu^2$.
H	The shape factor and ratio of δ_1/δ_2
K	The acceleration parameter in accelerating flow.
L	The length of the heated plate.
Nu_f	The forced convection Nusselt number for developing flow with variable properties used to understand buoyancy effects on heat transfer.
Nu_F	The forced convection Nusselt number.
Nu_{mix}	The mixed convection Nusselt number.
Nu_n	The natural convection Nusselt number.
Nu_x	The Nusselt number as a function of x position.
$\overline{P}$	The average pressure.
Pr	The Prandtl number based of air.
Ra_x	The Rayleigh number as a function of x position.
$\mathrm{Re_x}$	The Reynolds number based on the local position x, $U_\infty x/\nu$.
St	The Stanton number based on the local position x.
T	A generic reference to temperature.
T_s	The temperature of the surface of the heated plate.
T_∞	The free-stream temperature of the air in the test section.

Lower-case Greek

α_{21}	The error between the second and first refined grid solutions.
α_{32}	The error between the third and second refined grid solutions.
β	The volumetric thermal expansion coefficient of a fluid (air).
δ	The boundary layer thickness.
δ_1	The displacement thickness of the boundary layer.
δ_2	The momentum thickness of the boundary layer.
δy	The wall position error
ϵ	The turbulence dissipation rate.

ϵ_M	The eddy diffusivity for the CFD turbulence models.
ϵ_{21}	The difference of a quantity (such as heat flux) between the second and first grid refinements.
ϵ_{32}	The difference of a quantity (such as heat flux) between the third and second grid refinements.
η	The second shape factor of a boundary layer.
κ	The von Kármán constant for wall coordinate transformation.
λ	The wavelength of the laser light sheet.
μ	The dynamic viscosity of the fluid.
μ_t	The turbulent viscosity for the CFD models.
ν	The kinematic viscosity of the fluid.
ρ	The density of the fluid.

Upper-case Greek

$\Delta\overline{u}_{F,G}$	The relative difference of velocity for forced convection due to a change in gravity direction.
$\Delta\overline{u}_{F,T}$	The relative difference of velocity for forced convection due to a change in heated plate temperature.
$\Delta\overline{u}_{M,G}$	The relative difference of velocity for mixed convection due to a change in gravity direction.
$\Delta\overline{u}_{M,T}$	The relative difference of velocity for mixed convection due to a change in heated plate temperature.
Δp	A pressure drop.
Δt	The time interval between images for PIV measurements.
$\Delta\overline{u}$	Streamwise velocity residual.
$\Delta\overline{u'u'}$	Normal Reynolds stress residual.
Δx	The particle image displacement in PIV measurements.

Acronyms

ASME	American Society of Mechanical Engineers
CFD	Computational Fluid Dynamics
GCI	Grid Convergence Index
LDA	Laser Doppler Anemometry
M&S	Modeling and Simulation
NGNP	Next Generation Nuclear Plant
PIV	Particle Image Velocimetry
RMS	Root Mean Square; in PIV data, the standard deviation
SRQ	System response quantity
TKE	Turbulence kinetic energy
VEC	Validation Experiment Completeness
VHTR	Very High Temperature Reactor
V&V	Verification and Validation

Chapter 1

Introduction

This project is to provide high fidelity experimental validation data for use in computational fluid dynamics simulation validation. Computer simulations are often used to predict the flow of coolant and heat transfer characteristics in nuclear reactors. Most cost effective simulations require models to predict the flow characteristics. These models will yield erroneous predictions if used in scenarios where they are not wholly valid because the assumptions and approximations inherent in the model are not applicable. Validating the model with experimental results is necessary for simulation accuracy [5]. This chapter will describe the motivation for the project, validation of computational fluid dynamics simulations, and convection. The objectives of the project are discussed in Chapter 2. The design of the experimental apparatus and the instrumentation are described in Chapter 3. The procedures used to conduct the tests and the methods of data analysis are included in Chapter 4. The results from the experiments and discussion of the results are contained in Chapter 5. Lastly, the conclusions are presented in Chapter 6.

1.1 Motivation

As the next generation of nuclear reactors are designed, numerical analysis of the reactor and its new features must be performed for operating and accident conditions. However, without experimental validation, a simulation of fluid flow should not be considered as a reliable prediction of real-world behavior [5].

The Next Generation Nuclear Plant (NGNP) uses a High Temperature Gas-cooled Reactor (HTGR) to generate the heat. The core and containment buildings have many surfaces that are cooled by forced/mixed/free convection, depending on the situation. As a specific example, consider the core and reactor vessel shown in Fig. 1.1. The convection on the several vertical surfaces can be simplified to vertical planes for validation purposes. The core is cooled using buoyancy-opposed forced convection under normal operating conditions. In the up-comer leading into the core, the flow is buoyancy-aided forced convection. In an accident situation such as a loss of flow accident (a loss of power to the pumps forcing the coolant through the reactor), the downward forced flow may stop and the coolant would transition to natural convection (flowing opposite of the arrows in Fig. 1.1).

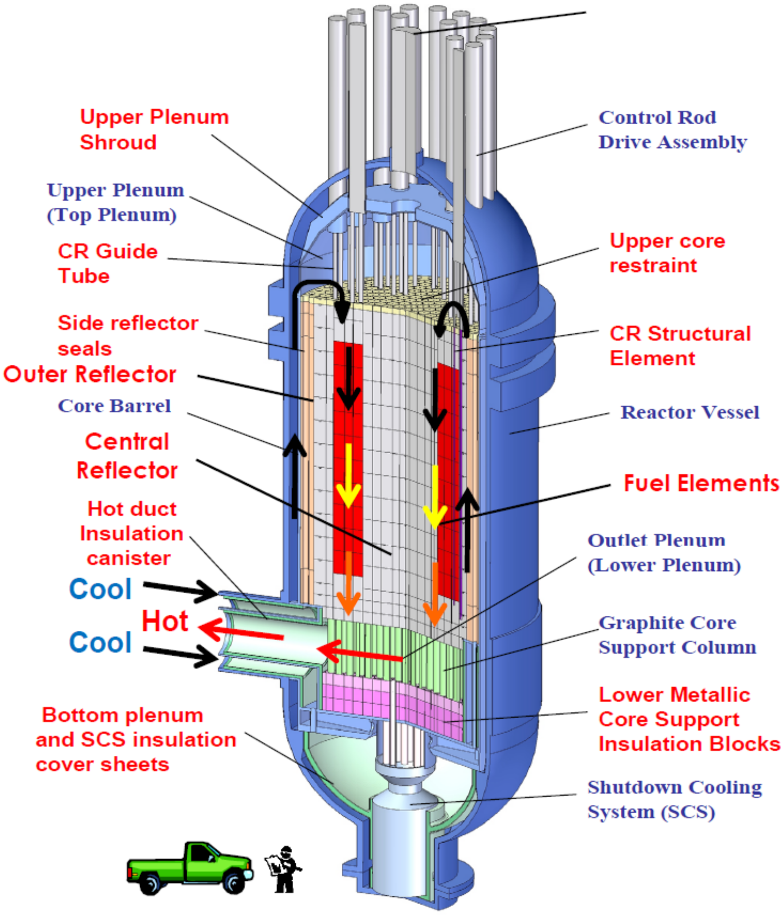

Fig. 1.1: A diagram of a HTGR showing the flow directions for convection over a vertical surface and the relative size of the core design [1].

The Rotatable Buoyancy Tunnel (RoBuT) was constructed to allow for measurement of all the convection regimes that exist in the core in Fig. 1.1. Both buoyancy aided and opposed, with the blower speed adjusting to make the convection forced, mixed, natural, or transitioning between the three. The blower can be programmed to create a transient case where the convection transitions from forced to natural. The design of the test section and experiments are described in Chapter 3 and Chapter 4.

Simulations are used to predict the flow, heat transfer, and the transition of flow in an accident scenario, but transient simulations often have high uncertainty. Experimental data is necessary to validate the models used in the simulations, but it is not feasible to build a reactor or scale model. The simplified geometry used in the RoBuT is sufficient for modeling and simulation (M&S) validation purposes. Some basic theory of validation is presented in the following section. Relevant studies of convection are also presented in the following sections.

1.2 Validation

The word validation is often used interchangeably with verification. The two terms mean very different processes in ensuring simulation reliability. The ASME Standard is useful in providing a background of validation, and additional detail is available in literature from the AIAA Guide for the Verification and Validation of Computational Fluid Dynamics Simulations [2] and Oberkampf *et al.* [3, 6]. Validation experiments often compare computer simulations to benchmark data or experimental data. The simulation and experimental system response quantities are compared using a validation metric, which is an objective mathematical operator [3, pg. 473]. It is important to know the difference between verification and validation and the AIAA definitions are included below [2, 3, 6].

> Verification: the process of determining that a model implementation accurately represents the developers conceptual description of the model and the solution to the model.
>
> Validation: the process of determining the degree to which a model is an accurate representation of the real world from the perspective of the intended uses of the model.

The present work is focused on validation, so validation is discussed in more detail. A major component of validation includes quantification and identification of errors and uncertainties in the experiment and simulations [6]. When comparing the simulation and the experimental results, it is assumed that the experiment is "our best measure of reality" [6]. For a comparison of experimental data and computational results to be useful, the errors and uncertainties of both must be quantified [6]. In very basic terms, a validation study would include measuring a physical phenomena and at the same time measuring all of the relevant boundary conditions. A simulation is then conducted based on the measured boundary conditions. Several different mathematical models would be used in the simulations. Finally, the simulation response quantities are compared with the experimental response quantities using validation metrics. The models can be selected based on the quantification of model error when compared with the experiment.

Because of the complex nature of systems that would benefit from predictive models, a complete system is separated into several tiers of detail for validation experiments, as described by Oberkampf and Roy [3]. These tiers are shown in Fig. 1.2 with a summarized description of each tier. This dissertation describes an apparatus made for Benchmark Tier validation experiments. All model inputs are measured, most model outputs are measured, and experimental uncertainty is computed for all measured quantities [3]. Since the heat transfer and the fluid flow are coupled, this problem cannot be considered as a unit problem. The unit problem is often referred to as a separate effects test. To meet the requirements of the benchmark tier in the validation hierarchy, the hardware used in this wind tunnel is specially fabricated to validate specific aspects of flow over a heated flat plate. The complete system of interest is the passively cooled high temperature gas-cooled nuclear reactor discussed above (the accurate simulation of which, in addition to its validation, is extremely costly). The heated flat plate is meant to represent a component in the reactor and/or containment building. The wind tunnel and plate then become the simplified hardware meant to improve understanding of flow physics and the simulation accuracy in predicting real-world scenarios [3].

The inputs required to define the simulation (boundary conditions) are measured in the test section walls (tunnel geometry and wall temperature) and flow at the wind tunnel

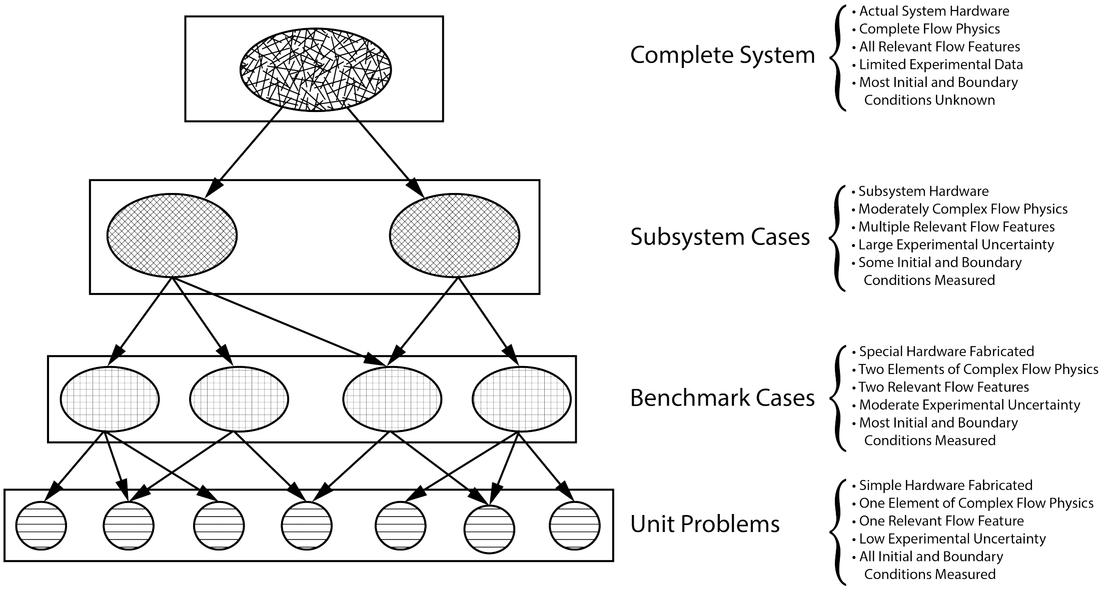

Fig. 1.2: Graphical description of the validation hierarchy, after [2].

inlet (inlet temperature, inlet velocity). These measurements include uncertainty estimates and the turbulence quantities at the inlet which can be computed from the inlet velocity data. The experimental data to be documented to meet the requirements for this tier of validation include [3]:

1. Detailed inspection of all hardware
2. Characterization of the variability of materials used in the experiment
3. Detailed information concerning assembly of the hardware
4. Detailed measurement of boundary conditions and excitation that were produced by the experimental apparatus or testing equipment

The hardware inspection and materials variability is included in the measurement of the boundary conditions. The hardware inspection is done whenever the geometrical boundary conditions are changed. The atmospheric variability is measured, and the conditions are recorded for each data set, including the data constituting the boundary conditions. The test section assembly procedures are recorded for repeatability. The last point is the measurements themselves, which include the boundary conditions and the system response to excitation.

The boundary conditions are measured in the experiment at the same time as the measurement of the system response quantities. The system response quantity (SRQ) is the quantity used in the validation metric to compare the simulation to the experiment. Measured and computed SRQ's are compared to validate the simulation with experimental measurements where both the simulation and the experiment are based on the same boundary conditions. For the purposes of this project, convection from a vertical heated plate with several convection regimes (forced, mixed, etc.) is considered. The SRQ's include the boundary layer velocity over the heated plate, the heat flux from the plate, and the shear velocity.

Another aspect of the validation study is determining the SRQ's to be used in the validation study. The procedures described by Oberkampf and Roy [3], and Wilson and Boyack [7] outline methods that can be used to define what aspects of the system should be used as SRQ's. Oberkampf and Roy [3] also describe the difficulty spectrum of measurements and computed quantities, as shown in Fig. 1.3. Using SRQ's from a wider range on the spectrum will ensure a more robust validation study. For instance, a model in a simulation that best predicts boundary layer velocity or temperature profile (a dependent variable) may not predict the heat flux very accurately (a first derivative). Using SRQ's from a wide range on the spectrum will aid in determining which simulation and model is the best predictor of the physical phenomena.

Often, analysts use approximate or idealized boundary conditions in simulations. To illustrate the importance of using measured boundary conditions in a simulation, we observe Fig. 1.4. In many CFD simulations, a parabolic or uniform inlet profile is used. For the wind tunnel considered herein, a uniform inlet velocity assumption is valid for most of the inlet area, but not in the boundary layer. The parabolic assumption is totally erroneous for this application.

The turbulence levels at the inlet of the simulation are often assumed to be a percentage

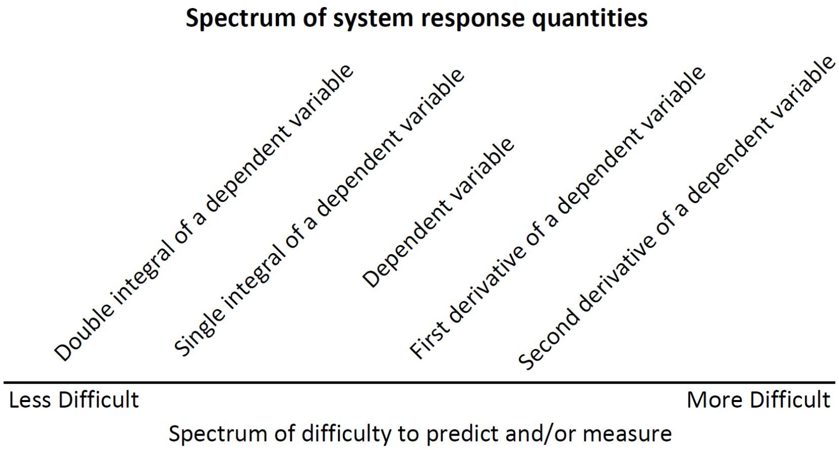

Fig. 1.3: The difficulty spectrum of SRQ's, after [3].

of the inlet velocity. The profiles in Fig. 1.4 show these assumptions to be invalid for this wind tunnel. A 10% of free stream turbulence level provides a trend that gives high turbulence in the center of the test section. However, the peak values are actually in the boundary layer with very little turbulence in the free-stream. The slight asymmetry of the inlet turbulence levels would be missed if the incorrect assumptions were made. Without measurements of the inlet, the assumptions used in simulations for the inlet are likely to be invalid. This would then make the validation study irrelevant, as the SRQ's from the experiment and the simulation are not based on the same boundary conditions.

One purpose of this work is to provide data for CFD validation, but obtaining such data from a written article is difficult, if not impossible. An online database is better suited for dissemination of data and documentation of the experiment. Though many validation datasets are available from several online databases, these normally lack the necessary detail to provide CFD simulation boundary and inflow conditions. Many such sources are listed at the CFD-Online website [8], including the National Aeronautics and Space Administration (NASA) NPARC Alliance Verification and Validation Archive [9] and the European Research Community on Flow, Turbulence and Combustion database [10]. Though valuable, these databases lack completeness for CFD validation as discussed in [11]. As part of the present effort, a database was developed to enable users to download the boundary condi-

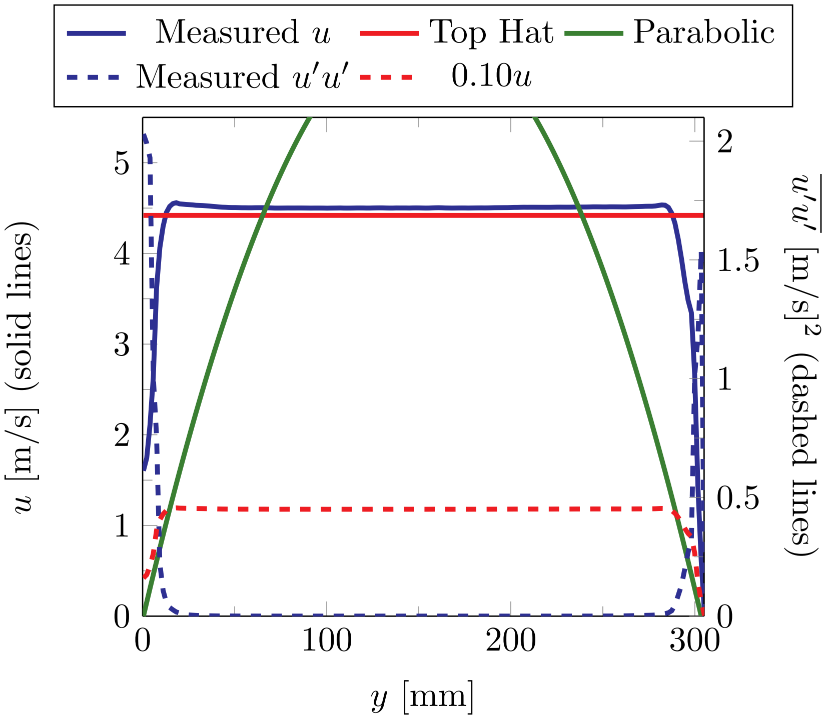

Fig. 1.4: A velocity profile for the inlet of the test section is shown, along with a top hat profile and a parabolic profile. The Reynolds Stress is also plotted along with a line of 10% of the free stream.

tions, SRQ data, and other relevant information to conduct their own validation studies, using the same boundary conditions to which the SRQ data correspond [12].

A more detailed outline of required measurements and documentation is found in the validation experiment completeness (VEC) table [11]. The detailed description of the information relating to the completeness level of the data are found on the project website, as it is too difficult to present all of the necessary data here. The information on the website is outlined following the layout of the VEC table. Most of the information is also contained in this dissertation, but the website eases the navigation of the relevant documentation.

As the uncertainty of the SRQ's is critical for computing the validation metrics, documentation of the uncertainty is included for both the SRQ's and the boundary conditions. The uncertainty of the velocity measurements is computed using the methods described by Timmins *et al.* [13], Warner *et al.* [14], and Wilson and Smith [15, 16]. Uncertainty of dimensions are found using methods presented by Coleman and Steele [17]. The heat flux uncertainty was provided by the sensor manufacturer. The methods used to quantify the uncertainties of the measurements (except velocity) are discussed in Chapter 4 and Chapter 5.

1.3 Convection

Many studies have been conducted to measure convective flows over heated flat plates. Few have used modern non-intrusive measurement techniques, and none have complete measurement systems sufficient to define a simulation's boundary conditions. A collection of studies is included herein, separated into their respective convection regimes (although some sources cover several of the regimes). Though not an exhaustive treatise of convection and boundary layer flow, the cited sources are useful in showing the difference between a discovery experiment (which includes most of the cited works) and a validation experiment (the proper implementation of which is impossible to find).

1.3.1 Forced Convection

Forced convection is commonly considered as flow with a convection ratio greater than 0.3, or $\mathrm{Gr_x}/\mathrm{Re_x^2} < 0.3$ [18]. The local Grashof number $\mathrm{Gr_x} = \mathrm{g}\beta(\mathrm{T_s}-\mathrm{T_\infty})\mathrm{x}^3/\nu^2$ and the local Reynolds number is defined as $\mathrm{Re_x} = \overline{\mathrm{u}}_\infty \mathrm{x}/\nu$. Lloyd and Sparrow conducted a theoretical analysis of forced convection over an isothermal vertical surface and cite experimental data for the same flow scenario [19]. Another experimental study of convection from a vertical heated plate is presented by Gryzagoridis [20]. This study (and many experiments of that time) used hot-wire anemometry to measure the flow velocity. Temperature profiles were used to find heat transfer rates. The available measurement equipment of the time limited the measurements rendering them insufficient for CFD validation.

McEligot and Jackson [21] discuss decades of research in convection and appropriate parameters that should be used when studying turbulent convection. The laminarization of accelerating flow is discussed. They also present the parameters in a form that can be used to compare non-circular ducts to circular tubes. These parameters would make more previous research applicable to this study. However, the caveat of turbulent flow at the inlet is required for their analysis to be valid.

Wang *et al.* present an experimental study of a vertical plane similar to the one considered in this work [4]. The velocity was measured using a two-component laser Doppler anemometry (LDA) system, which provides a point velocity rather than a velocity field. Temperature measurements were acquired using a thermocouple rake. The optical velocity measurements are beneficial and measurement of some boundary conditions were acquired, but the study was not meant for CFD validation and cannot be used for such (though it does provide much useful insight). The necessary boundary conditions were not all measured and the measurement uncertainties were not reported. The flow regimes and measurements reported are similar to those considered in this work.

Finally, a study that uses particle image velocimetry (PIV) to study the flow velocity is described by Hattori *et al.* [22]. The measurements were also acquired using hot-wire anemometry. The studies focused on the laminarization of the flow and provide valuable information using PIV measurements and convection data. However, the measurements obtained are also not intended for CFD validation (and are thus insufficient). Wall shear stress was also measured using the velocity and temperature data [23] using what appears to be the same apparatus as the study in [22].

The studies cited (and there are many more) show the depth of knowledge about forced convection from a heated vertical plate. The studies lack presentation of the acquisition of the boundary conditions, nullifying their use for simulation validation purposes. In essence, they are discovery experiments rather than validation experiments, and should not be used solely for validation purposes.

This flow regime was studied mostly to prove the wind tunnel characteristics and that the measurements acquired are sufficient to define the simulation boundary conditions. One reason to study the buoyancy aided forced convection is for the initial characterization of the new wind tunnel. Buoyancy aided forced convection is a well understood and documented flow regime. Comparison of the experimentally measured results with previous well understood studies is critical if the results for less understood flow regimes are to be trusted. The buoyancy opposed forced convection is studied to characterize the wind tunnel, and to provide a solid foundation for the future transient studies. The NGNP reactor normally operates in buoyancy opposed forced convection. Providing validation data for the transient from buoyancy opposed forced convection to natural convection is the end goal of the NEUP project.

1.3.2 Mixed Convection

Mixed convection is commonly considered as flow with a convection ratio greater than 0.3 and less than 16, or $0.3 < \mathrm{Gr_x}/\mathrm{Re_x^2} < 16$ [18], where the Grashof and Reynolds numbers are defined in Section 1.3.1. Mixed convection is a more interesting flow regime than forced convection because the buoyancy of the fluid has a larger impact on the flow, making it more difficult to accurately match the experiment with CFD simulations. Several studies of mixed convection are referenced by Jackson *et al.* [24], but are focused on convection in tubes. Much of the theory presented is valid for mixed convection from vertical surfaces. The turbulent characteristics of the flow changes with buoyancy effects. The studies of convection in tubes might prove more useful using the theory presented in [21]. Jackson also describes many studies of mixed convection for various flow scenarios in vertical passages [25].

Correlations are presented by Chen *et al.* [26] for mixed convection from a vertical plate for both buoyancy aiding and buoyancy opposing flow. Those correlations are compared with experimental measurements by Ramachandran *et al.* [27]. The measurements provided valuable data for the correlations, but could not provide detailed information for CFD validation. The study by Wang [4] is again presented, as mixed convection is studied therein. Again, this study lacks the detail necessary for CFD validation.

Hattori *et al.* [28] present hot and cold wire measurements of convection from a vertical plate. A study of transition and heat transfer rates is presented. The authors discovered a transition from random to harmonic fluctuations with laminarization of the flow. Again, the focus of the study was for discovery, not validation, and presents valuable information about convective flow.

The transition to turbulence was studied by Krishnamurthy and Gebhart [29] for mixed convection from a uniform heat flux vertical surface. Several key parameters are presented to quantify thermal and velocity transition. The measurements were acquired using a hot wire and thermocouples, as well as voltage and current to measure the power into the test section.

Gavara *et al.* [30] present a theoretical study of mixed convection for laminar flow. The study did not include simulations (being laminar flow) so the validation mentioned therein is not congruent with CFD validation discussed in this paper. Yadav and Kant [31] describe a validation study of mixed convection. The experiment and analytical solutions are compared. Again, the complexities of a CFD validation effort is not included in the scope of this study.

Abedin *et al.* [32] discuss a direct numerical simulation for convection from a vertical plate for both buoyancy aided and opposed convection. The transition point and laminarization of the flow is discussed, comparing the simulation to the experimental data of the sources previously presented. The mixed convection studies provide much helpful insight into the response of flow to heating. The studies were all meant as discovery experiments, thus the measurements acquired are insufficient for CFD validation.

The laminarization of the flow is another topic briefly considered in this study. The previously mentioned study by Hattori *et al.* [28] present relatively recent work in laminarizing flow. An acceleration parameter K_v less than 2-3$\times10^{-6}$ suggests that the flow would not laminarize [21, 33, 34]. The heat flux can be suppressed in buoyancy aided flow, depending on the significance of the buoyancy forces [21]. Some of the data presented in this dissertation show laminarizing characteristics and its effects on heat transfer. The observations from the measurements by Shehata and McEligot [35] are comparable to the results presented herein. The case 635 in [35] has about the same acceleration parameter as the buoyancy aided mixed convection case considered herein. However, as will be shown, this flow does show signs of laminarization, unlike the case considered in [35].

Chapter 2

Objectives

This paper will show the design process for a CFD validation experiment. The validation of the simulations is not included with the scope of this work. The objectives of this report include:

- Description and demonstration of experimental design for CFD validation experiments and developed a methodology consistent with validation theory explained by Oberkampf and Roy [3].
- Acquisition of experimental data sufficient to define simulation boundary conditions and system response quantity validation for forced and mixed convection in buoyancy aided and opposed orientations with an isothermal and constant flux heated plate (6 cases). These cases are graphically shown in Table 2.1. Data acquisition includes:
    - Inlet velocity profiles for forced, mixed, buoyancy aided, and opposed convection each with an isothermal or constant flux heated plate
    - Boundary layer velocity profiles at three streamwise locations for each case
    - Heat flux from the wall at three streamwise locations
    - Pressure drop through the test section for each case
    - Atmospheric conditions for each case
    - Experimental setup/settings for each case
    - Geometric measurements of the test section
    - Temperature of all four test section walls and wind tunnel inlet for each case
- Dissemination of experimental data (boundary conditions and system response quantities).

Table 2.1: Convection cases for data acquisition. The bottom row shows the plate conditions as isothermal or constant heat flux.

Forced			Mixed		
Aided		Opposed	Aided		Opposed
Isothermal	q”	Isothermal	Isothermal	q”	Isothermal

- Comparison of generic simulations to experimental data (not a complete validation study) for demonstration that the described methods are sufficient and the facility is adequate for CFD validation purposes.

- Development of procedures for data acquisition in the RoBuT to speed future validation efforts.

Chapter 3

Equipment

This chapter will describe the equipment available and what is built for this experiment. Hardware and software integration is necessary for an efficient validation experiment. The hardware is described with the relevant validation information. The experiment control software and data processing parameters were fixed for the final data acquisition and are described in this chapter. The chapter exists for this validation facility to meet the validation requirements described in Chapter 1.

3.1 Wind Tunnel

The experimental apparatus used for this project is a rotatable wind tunnel (RoBuT), built under a previous grant from the Department of Energy. The 12 × 12 × 78 in. test section is fixed to a ferris-wheel like frame that allows the direction of gravity relative to the wind tunnel to be changed. Fig. 3.1 shows the RoBuT and the coordinate system for the measurements and simulations. The origin is at the center of the leading edge of the heated plate. The x coordinate runs the length of the plate, y is the coordinate away from the plate, and z is the coordinate normal to x and y. The velocity components u, v, and w

The wind tunnel is shown in Fig. 3.2, and the components are labeled for future reference. There are flow straighteners and turbulence screens at the inlet of the contraction. The contraction has trips magnetized into its outlet, 4.58 in. upstream of the heated plate leading edge. The blower is on the downstream end of the test section.

3.1.1 Structure

The framework was designed and built by Engineering Design Laboratories [36]. The ferris-wheel is 20 ft. in diameter. Four 4 × 4 in. steel beams were installed off of the

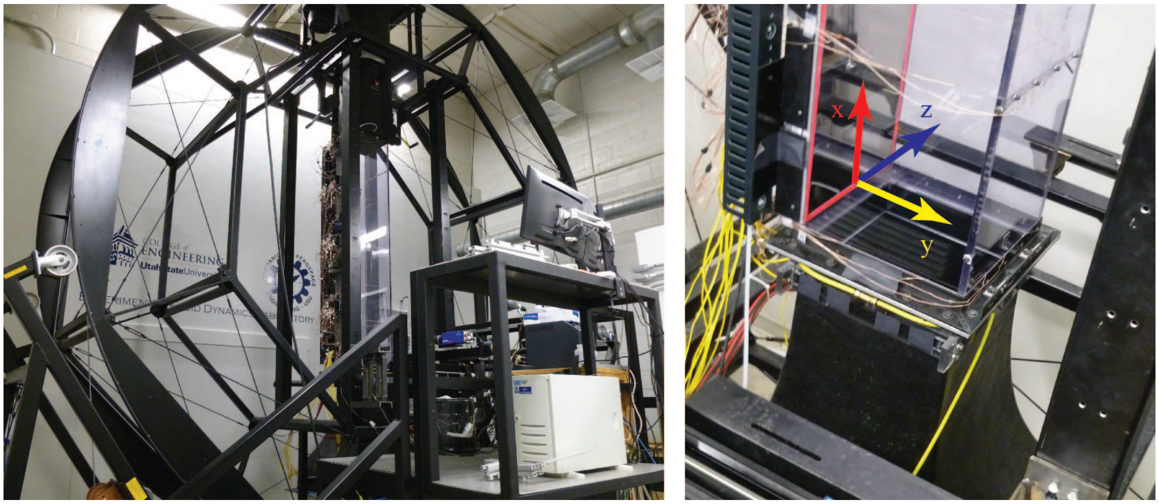

Fig. 3.1: The RoBuT showing the structure, wheel frame on the left. The right image shows the inlet and the coordinate system for the measurements.

corners of the test section and parallel to the direction of flow. These beams exist to mount the camera, laser, and other measurement equipment anywhere in along the test section. Ideally, a traverse stage would be mounted to these beams to ease x direction placement of the PIV equipment. However, the cost was too great for installation. These beams are visible in Fig. 3.1, with a close up of part of one beam on the far right of the right image. A drawing of the design is provided in Appendix B and was provided by the manufacturer.

Several mounting structures were designed to mount to those beams to hold traverse stages, camera, and laser while attenuating vibration caused by the flow inducing fan. Fig. 3.3 shows the completed traverse mounts. The mount toward the bottom of the image (the one with the blue camera and two traverse stages) is vibration dampening and easily removable to move the camera in the x direction, thus overcoming the lack of traverse stages in the x direction. The traverse stages allow the camera to be precisely moved in the y and z directions.

The laser traverse (top, center of Fig. 3.3) allows the laser to be precisely moved in the z direction. The laser traverse is fixed to a cart on rails and linked to the y direction camera traverse. Thus, when the camera is moved in the y direction, the laser moves with it. This linkage speeds data acquisition capabilities by only requiring one calibration at an

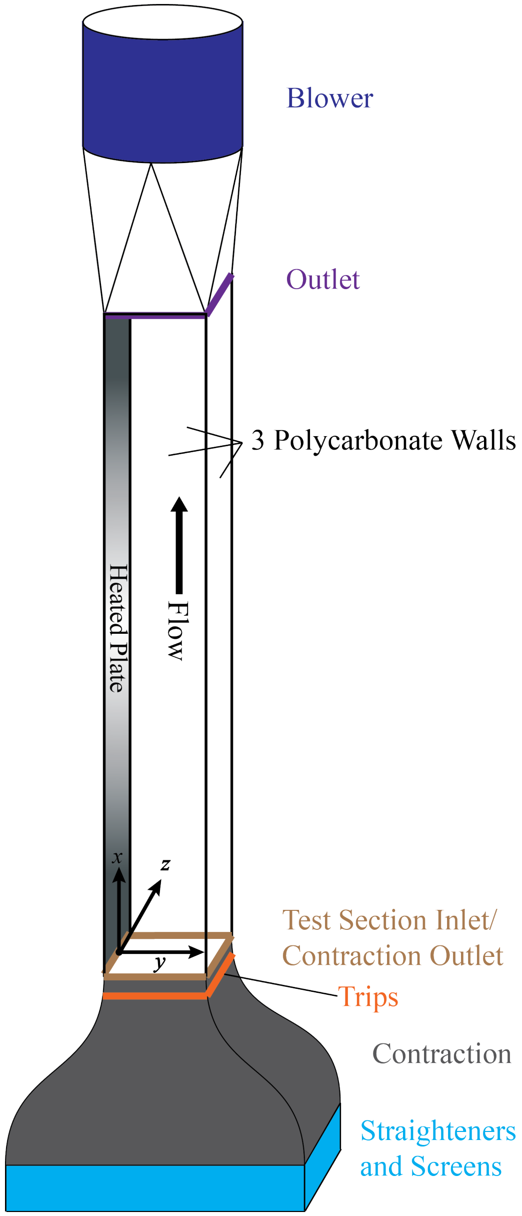

Fig. 3.2: A schematic of the wind tunnel, with nomenclature and coordinate system.

x position. This is most useful when measuring the inlet profile of the test section.

A hoist was also designed to remove the test section from the wind tunnel. Some features of the hoist include the capability to lift the test section and instrumentation from the wind tunnel to the center of the room. The test section can then be set on service stands, or moved to another location while another experiment is placed in the wind tunnel.

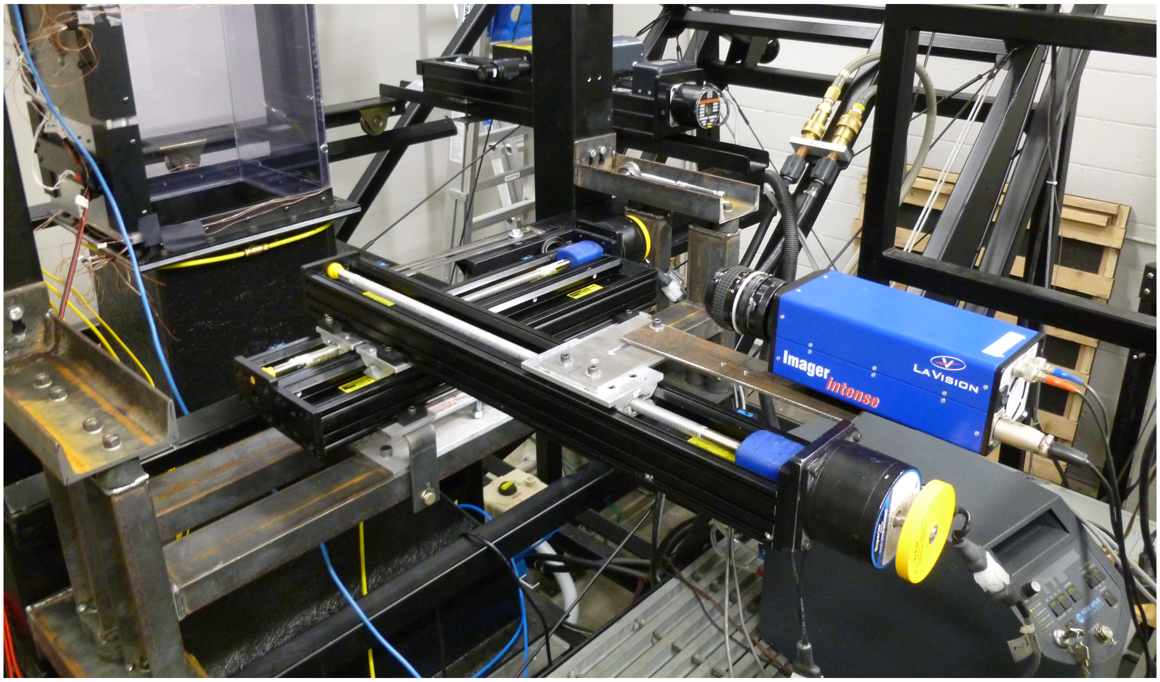

Fig. 3.3: A photograph of the traverse mounting equipment allowing for synchronized movement of the camera and laser in the y and z directions.

3.1.2 Test Section

The test section is made of three optically clear Lexan® polycarbonate walls, 0.5 inches thick. The walls will be referenced using the coordinate system in Fig. 3.1, where the heated plate is at $y = 0$, the left and right walls are at $z = -6$ in. and $z = 6$ in. respectively, and the top wall is at $y = 12$ in. The top wall is split into three sections, with the two ends being fixed into the mounting brackets and the center section removable for cleaning purposes (olive oil tends to build up in the test section over time, making optical measurements less reliable). The drawings for the test section components are included in Appendix C.

The fourth wall is the heated plate and its several components. The design for this plate was not completed as part of this work, and credit for its design goes to Blake Lance. However, it is necessary to understand its construction. The aluminum top plate is plated with nickel to decrease the thermal radiation heat transfer. Fig. 3.4 shows the heated plate assembly and the layout of the insulating layers surrounding the heated plate. The heated plate is surrounded with a layer of Teflon® to allow for thermal expansion and to increase the thermal resistance between the heated plate and the plastic side walls. The silicone rubber gasket at the outlet of the test section is to force pressure on the plate assembly to push it toward the inlet, minimizing gaps at the inlet. Springs are also inside the Teflon® liners at the outlet to push the liners against the inlet. A layer of insulation is under the heaters to maximize the heat from the plate into the test section and resist the heat from being wasted out the backside of the plate. The position of the instrumentation will be discussed in Chapter 3.2 (see also Appendix C).

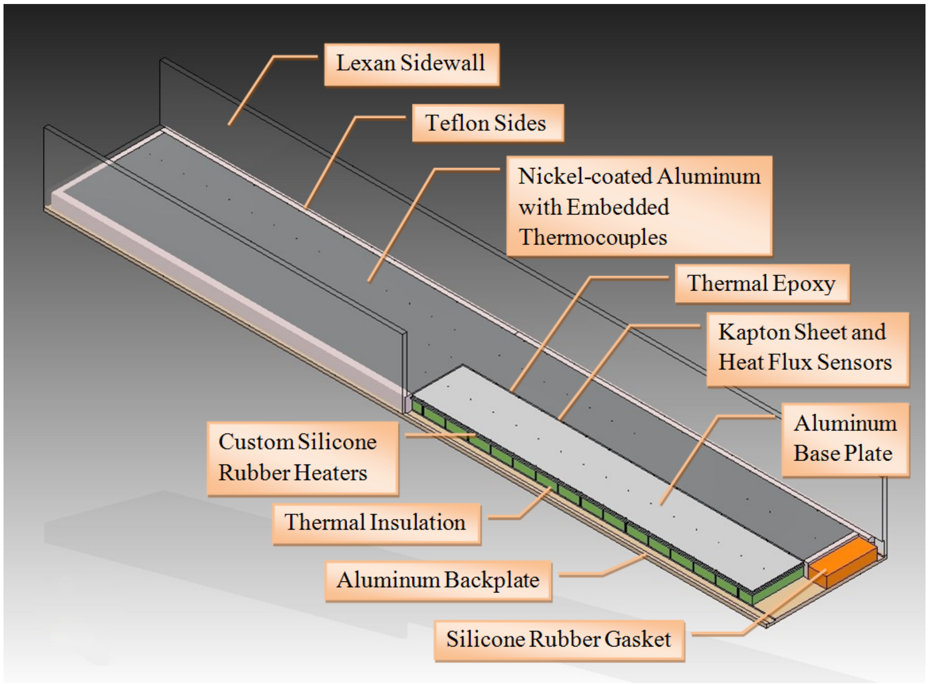

Fig. 3.4: The test section, heated plate and its several layers are shown. The plate is separated from the plastic sidewalls by a layer of Teflon®.

A more zoomed in diagram of the heated plate is shown in Fig. 3.5. The schematic of the layers are scaled relative to each other. The wire leads for a thermocouple and heat flux sensor are shown going through the layers to the outside of the test section (which is to the right).

3.2 Instrumentation

The instrumentation and control systems are run with a .vi code in LabVIEW [37].

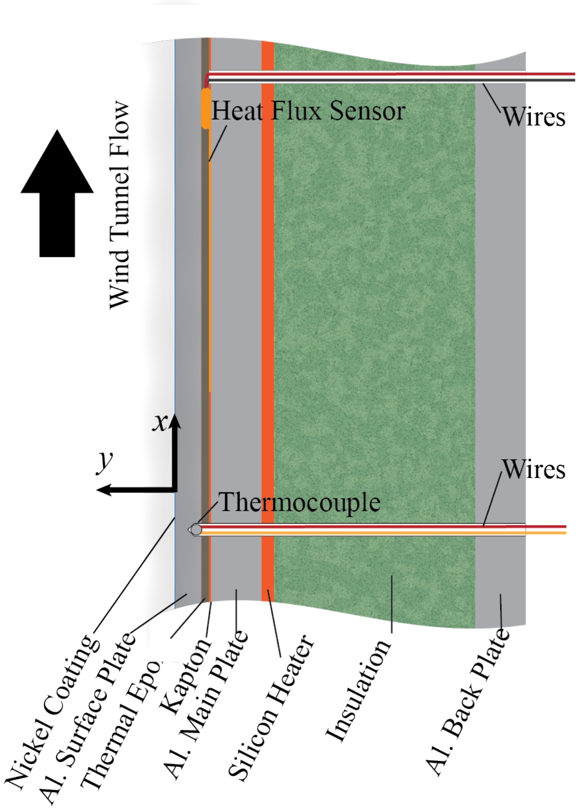

Fig. 3.5: The heated plate and its several layers are shown to relative scale with instrumentation wire leads going out of the test section to the right.

The Master VI is a Labview code that runs all of the hardware except the PIV system. It samples all of the temperatures, controls the room and plate temperatures, the seeding for the PIV, the blower speed, records the boundary conditions and the room conditions. This is a significant contribution to the success of the experiment, but there is no way to include it in this document. The National Instruments hardware includes 5 NI-cDAQ-9188 chassis that hold 20 NI-9213 16 channel thermocouple modules. All thermocouples and heat flux sensors were plugged into the modules for measurement. All thermocouples were calibrated before installation to a 0.03 degree source using a medium IsoTech Fast-Cal Temperature Calibrator. Another module and chassis control the larger voltage equipment, including the three power supplies for the six plate heaters and the room temperature control system. Fig. 3.6 shows the test section assembly and the layout of the heaters and heat flux sensors.

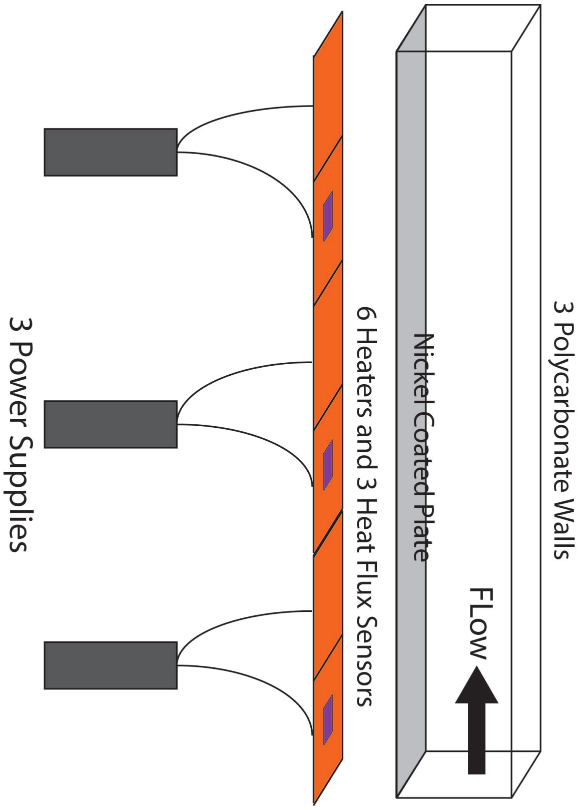

Fig. 3.6: The wind tunnel and control system showing the heaters and power supplies.

Pressure measurements are also acquired with the validation data and boundary condition acquisition. A Baratron 1-Torr pressure sensor with a MKS 270D signal conditioner. The wind tunnel manufacturer installed two pressure taps at the inlet and outlet of the contraction. These taps are used to measure the pressure drop through the contraction. Two more taps were installed at the test section inlet and outlet to measure pressure drop through the test section. These four taps are used to characterize the wind tunnel and to aid in measuring boundary conditions.

3.2.1 Atmospheric Conditions

The temperature of the room housing the RoBuT is kept constant using a control system in LabVIEW, a steam heater, and an air conditioning unit. The Master VI reads the ambient room temperature near the wind tunnel and adjusts the fan speed on the steam heater to compensate. The air conditioning unit holds the temperature at a comfortable level during the summer months, but cycles such that the room temperature fluctuates several degrees. The heater and control system compensate for the fluctuations from the air conditioner.

The air properties in the room are computed using the room temperature, humidity, and atmospheric pressure. The temperature and humidity are measured using Omega's HX92A which is accurate to 0.6°C and 2.5% relative humidity. The atmospheric pressure was sampled using a Barometric Pressure Sensor SB100 from Apogee Instruments, which is accurate to 1.5% of the reading for atmospheric conditions.

A separate .vi was written that samples and records the room air properties every minute. The properties are uploaded to a website in real time for reference purposes. The air properties can be pulled for any specific data acquisition. The code writes .lvm files that can be opened with a text editor. The columns include a date/time stamp, the temperature, pressure, and relative humidity.

3.2.2 Inlet Temperature

The inlet temperature is measured in the flow straightening honeycomb (see Appendix B). Figure 3.7 shows the inlet honeycomb on the downstream side (the contraction has been removed and the wind tunnel is in the buoyancy opposed orientation). There are three thermocouples installed by the manufacturer to control the inlet heat exchanger. The EFDL installed 15 thermocouples spaced uniformly in the honeycomb, as shown. These thermocouples were epoxied into position, leaving the thermocouple joint exposed to the inlet air flow. The position of the thermocouples are included in Appendix E. These thermocouples were fitted with Type K extension wire and plug ends for easy test section removal. The inlet stays fixed when the test section and instrumentation are removed, necessitating the connection between the thermocouples and the extension wire.

3.2.3 Wall Temperatures

Heating the plate is an important feature of the Master VI. There were 160 type K thermocouples are embedded from the underside of the plate to within 0.06 inches from

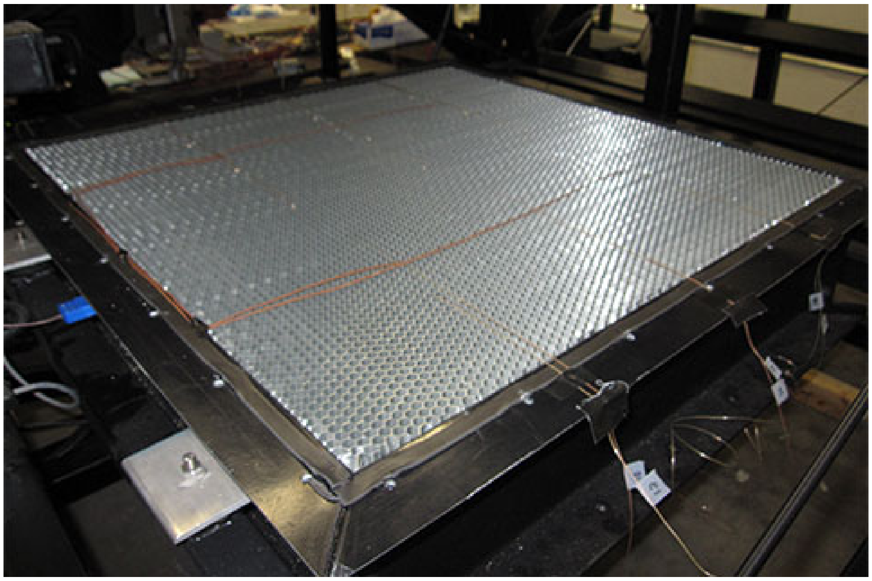

Fig. 3.7: The inlet honeycomb flow straightener viewed from the downstream side and showing the inlet thermocouples.

the surface of the plate using Dow Corning® 3-6751 Thermally Conductive Adhesive. The holes drilled into the plate are measured with a large micrometer several times to account for the uncertainty of the hole depth (and therefore, the position of the thermocouple). The thermocouples were all labeled for sorting after test section assembly, then installed. The epoxy was inserted with the thermocouple using a syringe. The plate was heated to 100°C for 30 minutes to cure the epoxy. Figure 3.8 shows the installation of the thermocouples into the heated plate.

The holes for the clear side walls are drilled in similar fashion to the ones in the heated plate. The thermocouples in the clear walls require an epoxy that would cure at room temperature. Weld On 40™ from IPS Corporation is used to fix the thermocouples into the clear side walls.

The thermocouples are in the clear walls are at x =0.0, 33.66, 62.55, 96.84, 123.8, 166.4, 192.4 cm. On the two side walls, at those x positions, the thermocouples are placed at y =19.05, 95.25, and 247.7 mm. On the top wall, the thermocouples are placed at z =-76.2, 0.0, and 76.2 mm and x =0.0, 33.66, 76.2, 103.2, 137.5, 166.4, 192.4 cm.

Six custom flexible silicone rubber heaters from Tempco are used to heat the plate.

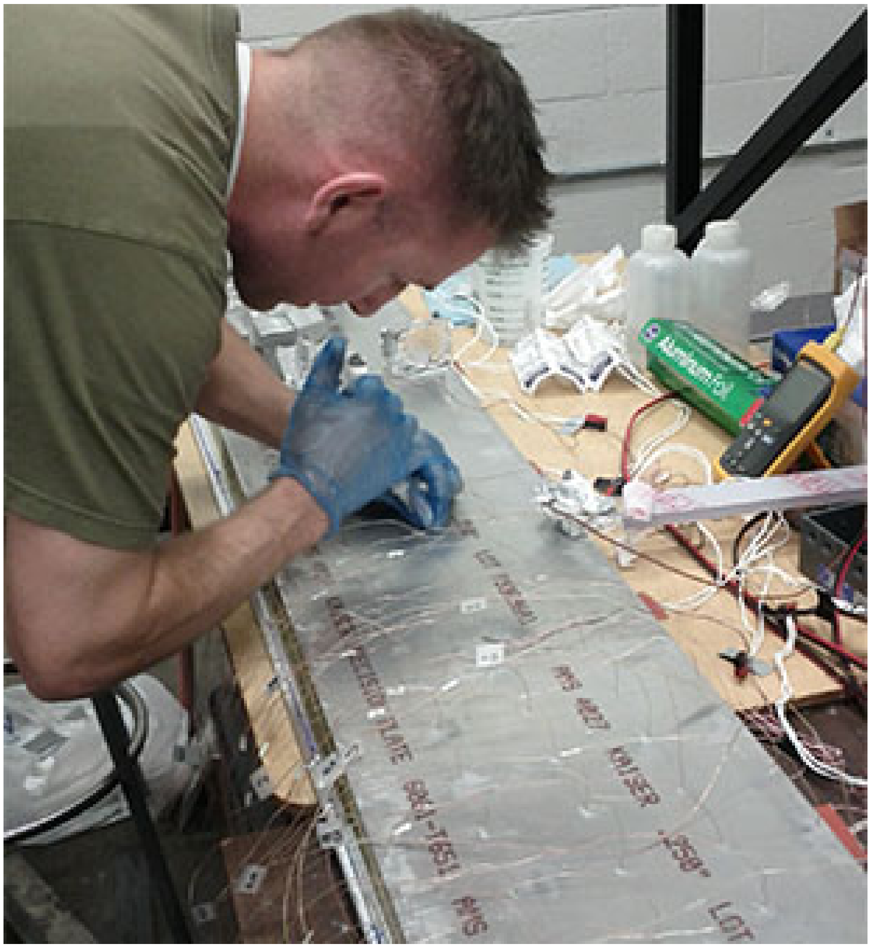

Fig. 3.8: The installation of the plate thermocouples using a syringe to place the epoxy to hold the thermocouples in place.

The heaters under the plate were powered with 3 HP power supplies. More detail regarding the heaters is found in Appendix D.

The plate temperature is controlled in LabVIEW using a PID control system. For the isothermal cases, the temperature is set by the user. For the cases considered herein, the set point is 150°C. The control system parameters (gain and integral constants) were tuned using the LabVIEW software, with gain of 0.5 and the time integral of 2.5 minutes. The isothermal control system can hold the temperature to within the accuracy of the thermocouples (less than 1°C). The constant flux case uses the same control system, but is driven by the measured heat flux.

3.2.4 Plate Heat Flux

Several heat flux sensors are embedded under the surface of the heated plate at positions 5.868, 30.118, and 54.868 inches from the heated plate leading edge. These sensors are centered in the z direction. Three RdF Corporation heat flux sensors, model 20457-3, are used, with each sensor having manufacturer specified properties and uncertainty of 5%. Table 3.1 shows the properties for each sensor.

Table 3.1: The heat flux sensor properties provided by the manufacturer. The x position of the heat flux sensors will be used in later analysis.

Heat Flux Sensor	Output μV/BTU/ft^{2}hr	Thermal Resistance °F/BTU/ft^{2}hr	Heat Capacity BTU/ft^{2}hr/°F	Response Time second
P1 = 5.87 in.	11.5	0.012	0.05	0.400
P2 = 30.12 in.	12.0	0.012	0.05	0.400
P3 = 54.87 in.	11.3	0.012	0.05	0.400

The heat flux measurements of sensor 2 show evidence of higher uncertainty than the manufacturer specifications. Figure 3.9 shows that for constant power to the heaters, the second heat flux sensor reads a lower heat flux than the other two sensors. The dip in heat flux is not driven by a drop in temperature because the temperature of the plate is smooth. The heat flux measurements in Fig. 3.9 are shown with 5% of reading uncertainty bands. As the second heat flux sensor is 10% lower than what it is expected to read, a 10% uncertainty is used in the reported heat flux SRQ for sensor 2. The first and third heat flux sensor readings are reported with the manufacturer specified uncertainty of 5%.

3.2.5 Particle Image Velocimetry

PIV is a major data acquisition component of the validation experiment. The equipment and processing parameters are included herein. For background purposes, PIV is a velocity measurement technique that uses a digital camera and a laser to take images of particles in a flow. The images are specially timed and correlated with each other to compute the velocity field. More detail on PIV can be found in Adrian and Westerweel's book [38], or in Raffel *et. al* [39].

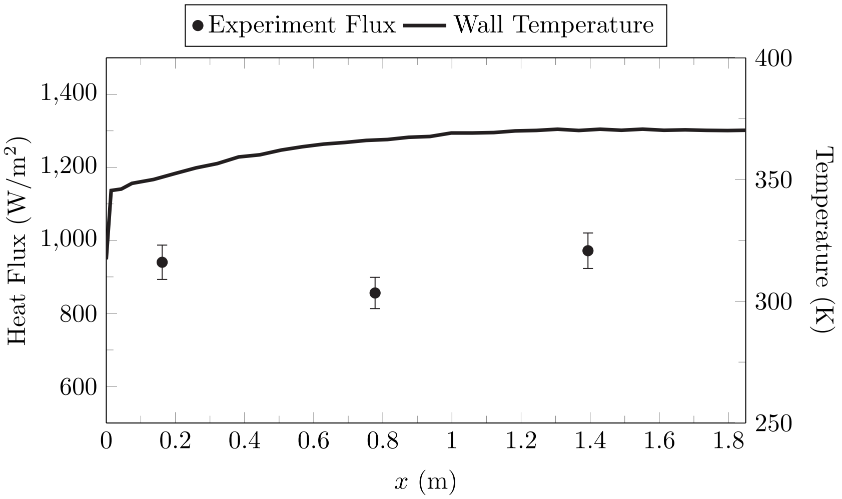

Fig. 3.9: The heat flux for a constant power forced convection case along with the $z = 0$ heated wall temperatures.

The PIV camera is an Imager Intense 12-bit digital camera from LaVision [40]. The CCD sensor is 1376×1040 pixels with a pixel size of 6.45 μm square. Two cameras can be used to acquire stereo PIV data, but the method proved infeasible for this project. The laser is a New Wave Research Solo PIV III 15. Two lasers at 50 mJ/pulse and 532 nm can fire up to 15 Hz with data acquired at 4 Hz in double-pulse mode.

Two different lenses are used on the camera, depending on what measurement is being acquired. A 105 mm. lens with an extension tube is used when acquiring images for the boundary layer flow over the heat flux sensors. A 28 mm. lens is used when acquiring images for the inlet boundary condition. In both cases, a filter is placed over the lens to decrease reflections allowing only 532 nm light is passed through the filter.

The data was acquired and processed using DaVis 8.1.6 [40]. A ruler was used to calibrate the camera for the inlet data, and a single plane calibration plate was used to scale the images for the SRQ data. The dewarping of images using this plate and the pinhole model was inaccurate. The calibration plate uses laser etched circles on an anodized aluminum plate. The dots are 0.980 mm (0.03 in) in diameter and spaced 3.175 mm (0.125 in) apart. The particle displacements were generally around 12 pixels in the free stream, with the particle diameters of 2 pixels. This diameter is near the optimum for small RMS errors due to particle diameter [39]. The uncertainty method accounts for the variation in particle diameter and displacements.

The images for the SRQ data used the entire imaging chip (1376×1040 pixels). The inlet data region of interest was generally 1376×256 pixels, with the focus being at the inlet of the test section. The images were processed using the following steps after the acquisition of the images:

1. The images were corrected for small vibrations and rotation using the wall as a reference (making the wall straight up and down and in the same position for every image).

2. The average image was subtracted from all of the images to decrease the background noise.

3. PIV Processing using 64×64 window with 1 pass, then decreased to a 32×32 windows with 75% overlap for two passes (the SRQ images were processed with image correction, per the dewarping calibration).

4. The PIV data were post-processed with an allowable vector range of 5 m/s (± 5 m/s) in v and 0 m/s (±1 m/s) in u (w was not measured for the validation data). The vectors were deleted if the peak ratio was less than 2. A median filter was used to remove vectors for which the difference to the average was greater than 1.75×RMS of its neighbors and inserted (or reinserted) if the difference to the average was less than 2.5×RMS of its neighbors. Also, groups with less than five vectors were removed and the allowable vector range was computed again.

5. The average and standard deviation (RMS or $\overline{u'u'}$, $\overline{v'v'}$) were also computed.

The laser was mounted such that only a spherical lens and cylindrical lens were used to focus the laser into a thin sheet. The cylindrical lens was selected to provide the maximum intensity to the laser sheet. Meaning, the sheet was just wide enough to obtain the inlet profiles and SRQ data. As measuring the laser sheet thickness inside of the test section was impossible, some simple qualitative sheet thickness techniques were used just outside of the test section ($z > 0.1651$ m.). Laser burn paper was used to aid in focusing the laser sheet. The sheet focal point was near the center ($y \approx 0.127$ m.) of the test section for the inlet profile measurements. The focal point was near the heated wall for the SRQ measurements.

PIV measurements require seed particles to be distributed in the flow. Compressed air is let into canisters using an electronically controlled pressure regulator (controlled using the Maser VI). The canisters are filled to a certain level with olive oil, covering small holes in the inlet pipe by 0.5 in. Olive oil is vaporized using the air and a Laskin nozzle style atomizer to make seed particles that are around 0.8 μm in diameter. The seeder is built similar to the description by Kähler [41], and more details can be found in the literature. Several of these seeding canisters are shown in Fig. 3.10. The particles are blown into a system of PVC pipe that is fixed to the inlet of the wind tunnel. The system is laid out in a grid pattern allowing for even dispersion of the seed particles.

The PVC grid is placed in a framework that is mounted to the wind tunnel frame. Pegboard and clear vinyl are used to disperse the seed uniformly and allow mixing before entering the contraction. The air/seed mixture then passes through a heat exchanger, flow straightener, and turbulence screens before the area contraction and finally entering the test section. The inlet temperature thermocouples are placed in the flow straightening honeycomb.

There were initially several optical problems with the PIV images. The first was high reflections from the laser light off of the Teflon™. Bulldog™ Adhesion Promoter was used to treat the non-stick surface of the Teflon™. After the treatment, Rhodamine paint was applied to the Teflon™ surfaces, allowing the reflections to be filtered out optically.

The second problem with the images was an optical distortion resulting from a change in air properties near the heated wall (like the familiar heat waves observable from car surfaces exposed to sunlight). This was corrected by moving the camera in the positive y direction and looking at the region of interest from an angle of several degrees (this angle changes slightly for each setup). The angle required a dewarping of the images and a small

Fig. 3.10: A photograph of a seeding canister, similar to a Laskin nozzle.

calibration target was designed for the calibration. As the calibration target is not a part of this dissertation, its attributes are included in Appendix A.

The camera and laser were both fixed to Velmex [42] traverse stages that allow for synchronized motion in the y and z directions. The traverses were each independently controlled with LabVIEW and allow for sub-millimeter displacements. To move the equipment in the x direction, the hardware was designed to mount easily at increments of 5 in. (127 mm), with mounts for the laser and camera providing more accurate placement.

Additionally, the room conditions are monitored and logged continuously, including temperature, pressure and relative humidity. These are used to determine the air properties for each run.

3.3 RoBuT Test Section Assembly

To meet the validation requirements, the assembly of the test section is described. The plate assembly is completed first, as shown in Fig. 3.4. The top plate is set upside down (with a protective semi-adhesive layer) on a level, smooth surface. Appropriate thermocouples are then threaded through the heaters and the six heaters are placed in position on the bottom surface of the top plate. Then the thermocouple wire is threaded through a layer of insulation, Kapton, and the aluminum support plate holes, see Fig. 3.5. Then the leads can be inserted into the appropriate channels in the thermocouple modules. With the plate assembly completed, the assemblage can be carefully turned upside up and set on the test section service stand.

The instrumentation is to be kept from being pinched, severed, or otherwise damaged during the assembly process. The plate assembly is set on a stable support constructed for this specific purpose. The Teflon® side pieces are fixed into place with long furniture clamps, with care taken to not damage the smooth nickel surface of the heated plate. The clear walls (previously assembled with the mounting brackets) can then be lowered onto the plate assembly, moving the clamps as needed. Weather stripping is used between the Teflon® and the clear side walls to help seal the wind tunnel. All instrumentation is tested before installation into the wind tunnel. After installation, all seams are checked for leakage.

As the installation or removal of the test section is a delicate task, the hardware required to do so was carefully designed and constructed. The hardware (hoist, test section stand, etc.) is documented in manuals and videos in the Experimental Fluid Dynamics Laboratory.

Chapter 4

Approach

This chapter summarizes the calculations done for the design of the experiment, during the experiment, and after the results were obtained. Discussion of the simulations is also included in this chapter. The results and discussion from the calculations are included in Chapter 5.

4.1 Apparatus Design

The general design of the rotating framework for the wind tunnel was completed previously. The contraction inlet and the test section itself are both designed to enhance the accuracy and spacial resolution of the measurements, thus making the simulation boundary conditions more reliable and the experiments more repeatable. The specifics regarding the equipment are described in Chapter 3 and in the appendices.

The measurement of the SRQ's were also considered in the test section design. The measurement of the boundary conditions could not interfere with SRQ measurements, so thermocouples and wires are strategically placed to not interfere optically with the PIV system. Since the velocity SRQ is at the same position as the heat flux sensor, thermocouples should not be in the way of the camera and laser on the three clear walls. To ensure the thermocouple placement in the test section walls would not interfere with PIV measurements, simple geometric calculations were conducted. The possible orientations of the PIV equipment was considered to enable the system to see the boundary layer flow at the heat flux sensor positions without obstruction. Another feature of the test section is a removable section on the top (y =12 in.) lid. This allowed for parallel experiments to be conducted without removing the entire test section. The removable lid also allowed for test section cleaning, rhodamine repainting, and other minor maintenance procedures.

The radiative properties of the nickel-coated aluminum plate were considered. A high emissivity of the plate would correspond to elevated levels of measured heat flux going to radiative heat transfer rather than convection. Ideally, all of the heat flux would transfer to the air through convection. However, a quantification of the radiative contribution to heat flux is necessary.

To ensure the radiative heat transfer from the plate is small, two methods are used to predict the emissivity of the nickel coated plate. First, from Howell [43], the normal emissivity is

$$\epsilon_n = \frac{4n}{(n+1)^2 + k^2} \tag{4.1}$$

where $n = 5.76$ and $k = 27.34$ are material constants for nickel plated aluminum at 413 K ($\lambda = 7.0\mu$m). Eqn. 4.1 gives a normal emissivity of 0.029. More thorough documentation of of n and k can be obtained from the *Handbook of Chemistry and Physics* [44]. The uncertainty of the emissivity using this method is not obtainable from the sources in the literature.

The second method uses an energy balance on the surface of the nickel plate, written as

$$q'' = h(T_s - T_\infty) + \epsilon_n \sigma T_s^4 - \epsilon_L \sigma T_L^4 \tag{4.2}$$

where all quantities are measured (or reasonably estimated) to find the nickel plate emissivity. The emissivity of the Lexan ϵ_L is set to 0.9. Using data from a natural convection state, the emissivity of the heated plate is 0.034.

Table 4.1: Parameters for computing the plate emissivity using an energy balance in a state of natural convection.

q''	h	T_s	T_∞	T_L	ϵ
400 W/m^2	6.36 W/m^{2}K	410 K	294 K	296 K	0.034

The radiation heat flux is 10% of the total heat flux measured from the plate in natural convection. If the same radiation flux is assumed for forced convection, then radiation is 3% of the forced convection flux. The h for natural convection is computed from a correlation presented by Incropera [45], and is

$$h = k/L \left[0.825 + \frac{0.387 Ra^{1/6}}{\left[1 + \left(\frac{0.492}{Pr}\right)^{9/16}\right]^{8/27}} \right]^2 . \tag{4.3}$$

The energy balance in Eqn. 4.2 is solved for ϵ_n and the Taylor series expansion to find the uncertainty of the emissivity of the nickel coated plate is

$$U_{\epsilon_n}^2 = \left(U_{q''} \frac{\partial \epsilon_n}{\partial q''}\right)^2 + \left(U_h \frac{\partial \epsilon_n}{\partial h}\right)^2 + \left(U_{T_s} \frac{\partial \epsilon_n}{\partial T_s}\right)^2 + \left(U_{T_\infty} \frac{\partial \epsilon_n}{\partial T_\infty}\right)^2 + \left(U_{\epsilon_L} \frac{\partial \epsilon_n}{\partial \epsilon_L}\right)^2 . \tag{4.4}$$

The uncertainty and derivative terms in Eqn. 4.4 are

$$\frac{\partial \epsilon_n}{\partial q''} = \frac{1}{\sigma T_s^4} \quad , \quad U_{q''} = 2\%, \tag{4.5}$$

$$\frac{\partial \epsilon_n}{\partial T_s} = \frac{-4q''\sigma T_s^3}{(\sigma T_s^4)^2} + \frac{3h\sigma T_s^2}{(\sigma T_s^3)^2} + \frac{-4hT_\infty \sigma T_s^3}{(\sigma T_s^4)^2} + \frac{-4\epsilon_L T_L^4 T_s^3}{T_s^8}, \tag{4.6}$$

$$\frac{\partial \epsilon_n}{\partial T_\infty} = \frac{h}{\sigma T_s^4}, \tag{4.7}$$

$$\frac{\partial \epsilon_n}{\partial \epsilon_L} = \frac{T_L^4}{T_s^4}, \tag{4.8}$$

$$\frac{\partial \epsilon_n}{\partial h} = \frac{T_\infty - T_s}{\sigma T_s^4} \quad , \quad U_h = \sqrt{\left(U_k \frac{\partial h}{\partial k}\right)^2 + \left(U_L \frac{\partial h}{\partial L}\right)^2 + \left(U_{\mathrm{Ra}} \frac{\partial h}{\partial \mathrm{Ra}}\right)^2} . \tag{4.9}$$

U_k is the uncertainty of the thermal conductivity of air, and $U_L = U_x = 1/32$ in. is the uncertainty of the plate length. The uncertainty of temperature is $U_{T_s} = U_{T_\infty} = 1°\mathrm{C}$. Equation 4.9 has further uncertainty and sensitivity terms that are

$$U_{\mathrm{Ra}}^2 = \left(U_\nu \frac{\partial \mathrm{Ra}}{\partial \nu}\right)^2 + \left(U_{T_s} \frac{\partial \mathrm{Ra}}{\partial T_s}\right)^2 + \left(U_{T_\infty} \frac{\partial \mathrm{Ra}}{\partial T_\infty}\right)^2 + \left(U_x \frac{\partial \mathrm{Ra}}{\partial x}\right)^2 , \tag{4.10}$$

$$\frac{\partial h}{\partial k} = 1/L \left[0.825 + \frac{0.387 Ra^{1/6}}{\left[1+\left(\frac{0.492}{Pr}\right)^{9/16}\right]^{8/27}} \right]^2 , \tag{4.11}$$

$$\frac{\partial h}{\partial L} = -k/L^2 \left[0.825 + \frac{0.387 Ra^{1/6}}{\left[1+\left(\frac{0.492}{Pr}\right)^{9/16}\right]^{8/27}} \right]^2 , \tag{4.12}$$

$$\frac{\partial h}{\partial \mathrm{Ra}} = k/L \left[\frac{0.1064 Ra^{-5/6}}{\left[1+\left(\frac{0.492}{Pr}\right)^{9/16}\right]^{8/27}} + \frac{0.0215 Ra^{-2/3}}{\left[1+\left(\frac{0.492}{Pr}\right)^{9/16}\right]^{8/27}} \right] . \tag{4.13}$$

Equation 4.10 requires further definition of uncertainty terms and these are presented below. The kinematic viscosity is a function of dynamic viscosity and the air density. Thus, the uncertainty of the kinematic viscosity can be expressed as

$$U_\nu = \sqrt{\left(U_\mu \frac{1}{\rho}\right)^2 + \left(U_\rho \frac{-\mu}{\rho^2}\right)^2} . \tag{4.14}$$

The dynamic viscosity μ is found from a polynomial fit to data contained in [44]. As a function of the temperature in Celsius, the viscosity is

$$\mu = 1.714 \times 10^{-5} + 4.879 \times 10^{-8} T - 4.5675 \times 10^{-11} T^2 + 7.3469 \times 10^{-14} T^3 . \tag{4.15}$$

The uncertainty of the viscosity is governed by the uncertainty of the air properties in [44]. The density is found from the ideal gas law $\rho = P/(TR_{air})$ and the air density uncertainty is

$$U_\rho = \sqrt{\left(\frac{U_P}{TR_{air}}\right)^2 + \left(U_T \frac{-PR_{air}}{(TR_{air})^2}\right)^2 + \left(U_{R_{air}} \frac{-PT}{(TR_{air})^2}\right)^2} \tag{4.16}$$

where the air gas constant is found from $R_{air} = 8.31434/M_{mix}$ and

$$M_{mix} = (1+\omega)/\left(\frac{\omega}{18.02} + \frac{1}{28.97}\right) . \tag{4.17}$$

The humidity ratio ω is found as a function of the measured relative humidity, pressure, and temperature and is defined as

$$\omega = \frac{0.622}{\frac{P}{\phi P_{sat}} - 1} \tag{4.18}$$

with $P_{sat} = 0.57574 + 0.0554T + 4.1195 \times 10^{-4}T^2 + 6.0733 \times 10^{-5}T^3$. The uncertainty of the air gas constant is negligible. The uncertainty of temperature $U_T = 0.6°\text{C}$ and the uncertainty of pressure $U_P = 1.5\%$ of reading. The last few sensitivities in Eqn. 4.10 are

$$\frac{\partial \text{Ra}}{\partial \nu} = \frac{-g\beta(T_s - T_\infty)x^3\alpha}{(\nu\alpha)^2}, \tag{4.19}$$

$$\frac{\partial \text{Ra}}{\partial T_s} = \frac{g\beta x^3}{\nu\alpha}, \tag{4.20}$$

$$\frac{\partial \text{Ra}}{\partial T_\infty} = \frac{-g\beta x^3}{\nu\alpha}, \tag{4.21}$$

$$\frac{\partial \text{Ra}}{\partial x} = \frac{3g\beta(T_s - T_\infty)x^2}{\nu\alpha}. \tag{4.22}$$

Using these equations and data from the experiment, the uncertainty of the emissivity is on the order of the emissivity itself. Thus, the energy balance yields $\epsilon_n = 0.03 \pm 0.03$.

4.2 Wind Tunnel Characterization

Being a brand new wind tunnel, the flow characteristics should be determined [46]. Several components that characterize the wind tunnel flow are included in this section. Further analysis of the characteristics of the flow and boundary layers are included in Chapter 5, as they are only understood after an analysis of the SRQ data.

4.2.1 Pressure Drop

The test-section flow calibration is completed using pressure taps in the contraction and PIV for velocity measurements. The wind tunnel manufacturer did a similar procedure using a pitot probe, but the test section has been replaced and the inlet modified, requiring an updated calibration. The wind tunnel manufacturer completed a characterization that is in closer harmony to that outlined in [46].

Bernoulli's equation is used at the contraction (see Fig. 3.2) to compute the velocity at the inlet of the test section. For Bernoulli's equation to be valid, the flow in the contraction must be steady, incompressible, and with negligible frictional losses. As the flow in this experiment is steady, subsonic, and the contraction is smooth, these are reasonable assumptions and Bernoulli's equation is a reasonable energy balance along streamlines. The pressure taps are at the contraction inlet and the contraction outlet. The pressure is known at the contraction inlet and outlet as well as the area ratio. Bernoulli's equation is

$$P_1 + \frac{1}{2}\rho U_1^2 + \rho g z_1 = P_2 + \frac{1}{2}\rho U_2^2 + \rho g z_2. \tag{4.23}$$

$P_1 - P_2 = \Delta P$ is measured with a Baratron 1-Torr pressure sensor. The air density is found by using the air properties in the room. Pressure taps were also placed the the test section inlet (several inches downstream of the contraction outlet) and test section outlet. These are used to compute the test section pressure drop.

The pressure drop through the inlet contraction and the test section are measured for the wind tunnel in a horizontal configuration (this eliminates any gravitational effects). Figure 4.2.1 shows the measured and predicted pressure drop for the test section and the inlet contraction.

The test section pressure drop is calculated using the Haaland equation [47] with no surface roughness. The test section frictional losses are computed using

$$\Delta P_f = f\frac{L}{D_h}\rho\frac{\overline{u}_\infty^2}{2} \tag{4.24}$$

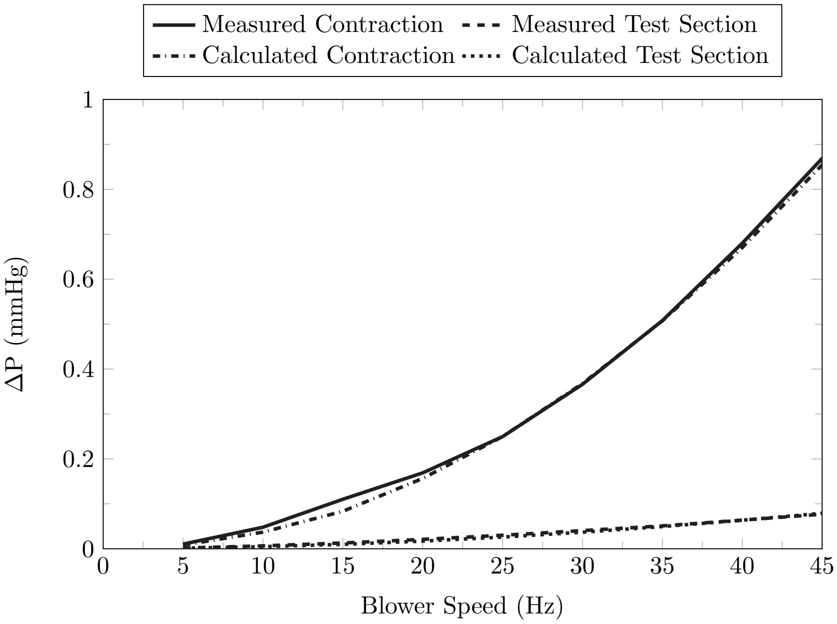

Fig. 4.1: Pressure drop in the contraction and test section with the wind tunnel horizontally oriented. The measured pressure drop is compared with calculations using Bernoulli's equation and frictional losses.

where the friction factor was found using

$$f = \left[-0.782 \ln\left(\frac{6.9}{\mathrm{Re}}\right)\right]^{-2}. \tag{4.25}$$

The contraction pressure drop agrees with the Bernoulli prediction using PIV velocity measurements. The frictional losses agree with the predicted loss from Eqn. 4.24.

4.2.2 Geometry

The test section as-built geometry was measured using a micrometer capable of measuring 12 inches with an accuracy of 0.0005 inches. As the test section when built is too long to measure using human arms, an apparatus was built to hold the micrometer in position and a string turned the micrometer until the measurement could be taken. Figure 4.2 shows a student holding the micrometer apparatus while a measurement is taken.

The as-built dimensions were defined as the height at z = -5.75, 0.0, and 5.75 in. and

Fig. 4.2: Photograph of as-built geometry measurement procedure.

width of the test section at y =0.25, 6.0, and 11.75 in. At each position, the micrometer was reset and the measurement repeated 3 times, providing an estimate of the repeatability of the measurement. Table 4.2 summarizes the last test section as-built measurements and Table 4.3 shows the uncertainty of those measurements.

Table 4.2: The measured as-built dimensions for the test section in inches.

	Height			Width		
Position x	-5.75	0.00	5.75	11.75	6.00	0.25
00.000	11.982	11.995	11.991	11.996	12.001	12.005
13.285	12.020	12.019	12.020	12.023	12.007	12.003
24.635	12.029	12.017	12.023	12.018	12.027	12.013
38.135	12.003	12.023	12.028	12.035	12.035	11.996
48.775	12.040	12.041	12.034	12.036	12.042	12.018
65.525	12.044	12.046	12.025	12.014	12.038	12.001
75.810	12.002	12.018	12.019	12.005	12.025	11.992

These data are used to construct a virtual test section for the simulation geometry definition (see Section 4.4). The measurement geometry and the simulation geometry are

Table 4.3: The measured as-built dimensions uncertainty for the test section in inches.

	Height			Width		
Position x	-5.75	0.00	5.75	11.75	6.00	0.25
00.000	±0.004	±0.001	±0.004	±0.004	±0.001	±0.007
13.285	±0.001	±0.004	±0.004	±0.002	±0.004	±0.007
24.635	±0.012	±0.002	±0.013	±0.001	±0.005	±0.002
38.135	±0.001	±0.007	±0.006	±0.004	±0.005	±0.009
48.775	±0.004	±0.002	±0.001	±0.007	±0.007	±0.007
65.525	±0.007	±0.002	±0.008	±0.005	±0.002	±0.007
75.810	±0.001	±0.001	±0.000	±0.001	±0.003	±0.017

then in agreement, within the stated uncertainty. These measurements are taken any time the test section is taken apart and/or removed. The removable lid does not introduce significant errors in the wall dimensions. A previous study for this project showed that the difference between the as-built geometry and the as-designed geometry was insignificant in the simulation [48].

4.2.3 Temperatures

The thermocouples in the walls, inlet, and room are used to quantify the wall temperatures, inlet temperatures, and atmospheric temperature for the simulations. The air properties are defined by measuring the air temperature, humidity, and atmospheric pressure, as described in Chapter 3.2.1. Every PIV measurement has a corresponding measurement of temperatures.

For example, data for the forced, isothermal case has 12 instances of independent PIV measurements (nine inlet measurement planes and three SRQ planes). Each of these has recorded wall temperatures and atmospheric conditions. The average of the atmospheric conditions and the average of the wall temperatures is computed to define the corresponding simulation boundary conditions. This method also provides data to compute the precision uncertainty of those boundary conditions, where the systematic uncertainty is defined in Chapter 3.2. The code that accomplishes this is included in Appendix F.

The temperatures are recoded in .csv files that are easily imported into StarCCM+

to define the temperature of the walls and inlet. The files also contain the uncertainty of the temperatures. An example of the wall and inlet temperatures in StarCCM+ is shown in Fig. 4.3 for the buoyancy aided mixed convection constant heat flux case. The flow in Fig. 4.3 is from left to right.

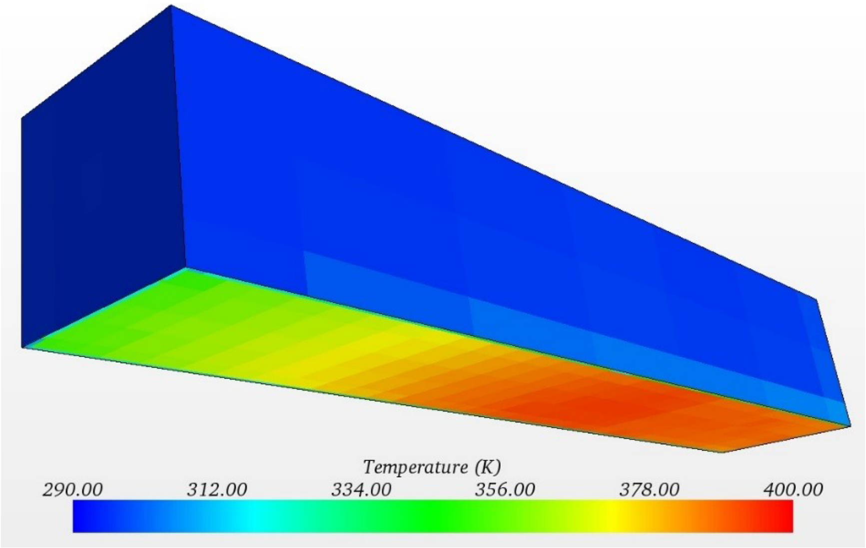

Fig. 4.3: The wall temperatures and inlet temperature viewed in StarCCM+.

4.2.4 Inlet Treatment

The PIV system is used to measure the inlet velocity on 9 planes, measuring u and v. These planes of data are used to define the simulation inflow conditions. The turbulence parameters for a specific model is derived from the measured velocities. An example of the measured inflow is shown in Fig. 4.4.

Rather than measuring the u and v velocities, then moving the PIV gear to measure u and w for every case, as shown in Fig. 4.5, a simplifying assumption can be made requiring the measurement of all three components only once. Data is acquired in Orientation A to obtain u and v at the inlet. The equipment is moved to Orientation B to obtain u and w at the inlet using the same spacial resolution. The results for the center profile of the two orientations are shown in Fig. 4.6.

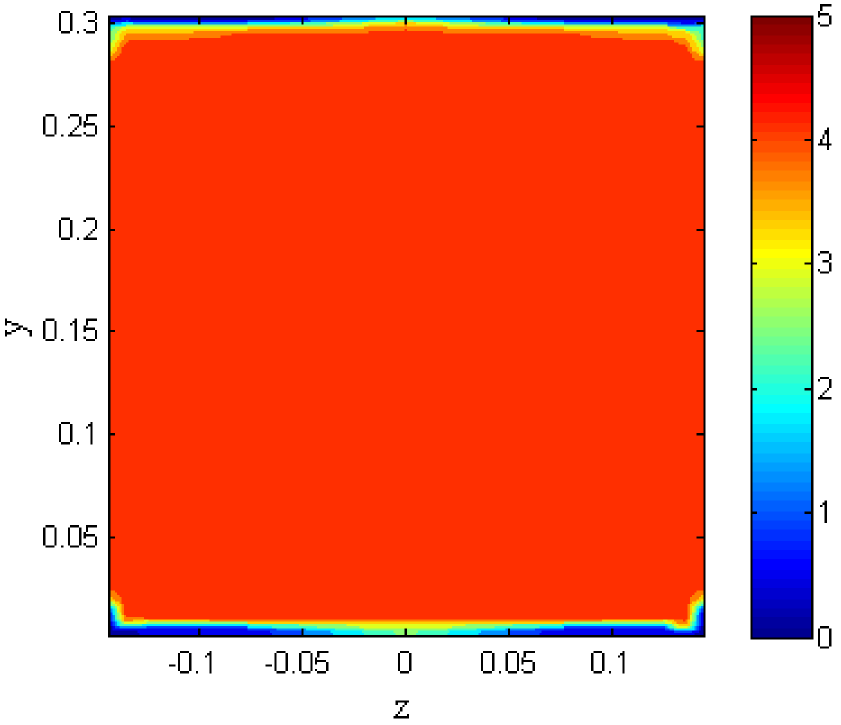

Fig. 4.4: The inlet velocity magnitudes using the nine PIV planes.

In Fig. 4.6, several conclusions can be made. First, v and w are the same over the width of the test section and in the boundary layer. Another observation is that the streamwise fluctuations are significantly higher than the cross-flow fluctuations in the boundary layer, $\overline{u'u'} > \overline{v'v'} = \overline{w'w'}$ and $\overline{v'v'} = \overline{w'w'} < 0.2 \pm 0.017\text{m/s}$. At this location, $\overline{u'u'} = 1.8 \pm 0.17\text{m/s}$ justifying an approximation that $\overline{v'v'} = \overline{w'w'} \approx 0$. These conclusions can be used to simplify the definition of the turbulence dissipation rate [18, p. 64], shown as

$$\epsilon = \nu \overline{\frac{\partial u_i'}{\partial x_j} \frac{\partial u_i'}{\partial x_j}}. \tag{4.26}$$

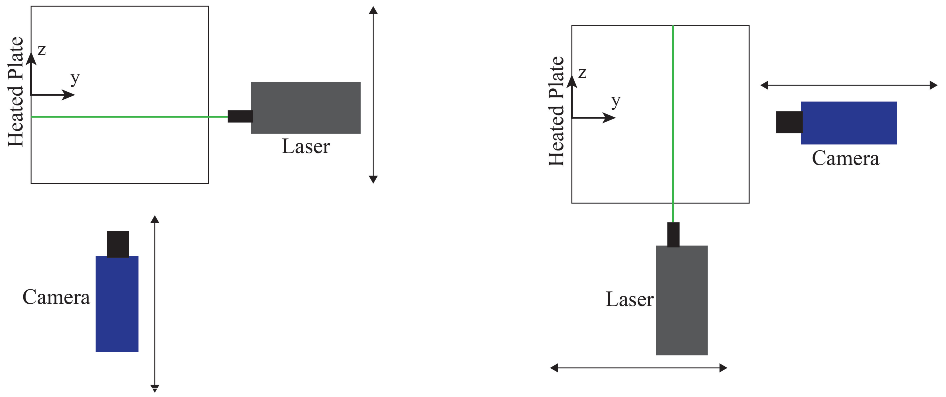

(a) (b)

Fig. 4.5: The orientation of the camera and laser for PIV inflow data acquisition. The laser and camera are traversed across the test section to obtain several planes of velocity data The flow direction is out of the page. (a) shows the nominal setup that is also used to obtain the velocity over the heat flux sensors. (b) shows the inlet profile specific orientation to obtain the w component of velocity.

Equation 4.26 can be written in the form

$$\begin{aligned}\epsilon = \nu \Bigg\{ & 2\left(\frac{\partial \overline{u'}}{\partial x}^2 + \frac{\partial \overline{v'}}{\partial y}^2 + \frac{\partial \overline{w'}}{\partial z}^2\right) + \frac{\partial \overline{u'}}{\partial y}^2 + \frac{\partial \overline{u'}}{\partial z}^2 + \frac{\partial \overline{v'}}{\partial x}^2 + \frac{\partial \overline{v'}}{\partial z}^2 + \frac{\partial \overline{w'}}{\partial x}^2 + \frac{\partial \overline{w'}}{\partial y}^2 \\ & + 2\left(\frac{\partial \overline{u'}}{\partial y}\frac{\partial \overline{v'}}{\partial x} + \frac{\partial \overline{u'}}{\partial z}\frac{\partial \overline{w'}}{\partial x} + \frac{\partial \overline{v'}}{\partial z}\frac{\partial \overline{w'}}{\partial y}\right)\Bigg\} \qquad (4.27)\end{aligned}$$

where $\overline{u'}$, $\overline{v'}$, $\overline{w'}$ are the fluctuating values. We can measure $\frac{\partial \overline{u'}}{\partial x}$, $\frac{\partial \overline{u'}}{\partial y}$, $\frac{\partial \overline{v'}}{\partial x}$, $\frac{\partial \overline{v'}}{\partial y}$. Also, measurements have shown that $v = w$ and $\overline{v'} = \overline{w'}$ at the inlet of the test section. Using these facts, Eqn 4.27 can be rewritten as

$$\begin{aligned}\epsilon = \nu \Bigg\{ & 2\left(\frac{\partial \overline{u'}}{\partial x}^2 + \frac{\partial \overline{v'}}{\partial y}^2 + \frac{\partial \overline{v'}}{\partial z}^2\right) + \frac{\partial \overline{u'}}{\partial y}^2 + \frac{\partial \overline{u'}}{\partial z}^2 + 2\frac{\partial \overline{v'}}{\partial x}^2 + \frac{\partial \overline{v'}}{\partial z}^2 + \frac{\partial \overline{v'}}{\partial y}^2 \\ & + 2\left(\frac{\partial \overline{u'}}{\partial y}\frac{\partial \overline{v'}}{\partial x} + \frac{\partial \overline{u'}}{\partial z}\frac{\partial \overline{v'}}{\partial x} + \frac{\partial \overline{v'}}{\partial z'}\frac{\partial \overline{v'}}{\partial y}\right)\Bigg\}. \qquad (4.28)\end{aligned}$$

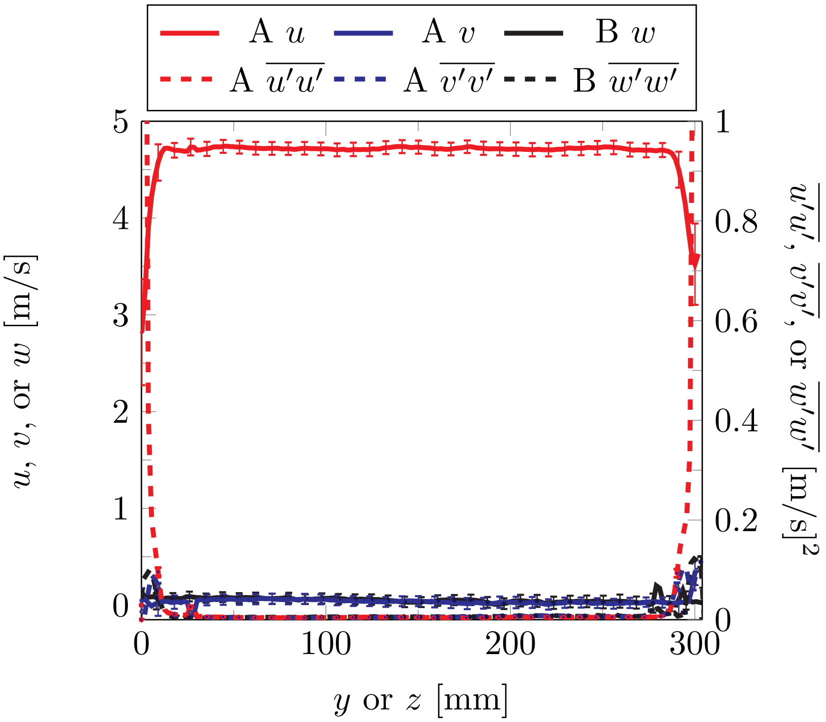

Fig. 4.6: Center profiles for two orientations showing justification for several assumptions at the inlet of the test section.

However, Since $\overline{v'v'} = \overline{w'w'} < \overline{u'u'}$ we can derive an equation for ϵ for our specific case as

$$\epsilon = \nu \left\{ 2\left(\frac{\partial \overline{u'}^{2}}{\partial x}\right) + \frac{\partial \overline{u'}^{2}}{\partial y} + \frac{\partial \overline{u'}^{2}}{\partial z} \right\}. \tag{4.29}$$

The turbulence kinetic energy is also found from the measured inlet data. The definition of the turbulence kinetic energy [18, p. 64] is

$$k = \frac{1}{2}\left(\overline{u'u' + v'v' + w'w'}\right). \tag{4.30}$$

It is assumed that $\overline{v'v'} = \overline{w'w'}$, simplifying the equation to

$$k = \frac{1}{2}\left(\overline{u'u' + 2v'v'}\right). \tag{4.31}$$

However, further simplification eliminates the $\overline{v'v'}$ term making the turbulence kinetic energy a function of $\overline{u'u'}$ only. To be slightly more accurate, the small values of $\overline{v'v'}$ are left in for the computation, as they are measured with $\overline{u'u'}$ at no extra cost.

The procedure for acquiring the inlet data is described in the following list. For the inlet data, 9 planes of 2-component PIV data are acquired in Orientation A. Orientation B is only acquired to prove that it is not a necessary measurement at the inlet. So, 9 planes are acquired at Orientation A. Orientations A and B are shown in Fig. 4.5.

1. Setup laser, camera, and respective traverse stages, and align with the calibration target.
2. Calibrate camera and match laser plane to calibration plane.
3. Set acquisition timing for sufficient particle displacements.
4. Set seeder flow rate.
5. Set laser intensity.
6. Set f-stop (which impacts particle image intensity and size).
7. Stabilize room, wall and flow conditions.
8. Record PIV data, temperatures, heat flux, equipment position, blower speed, heater and seeding settings, camera and laser settings, and room conditions.
9. Move to next plane and repeat.

After the inlet data are acquired, several computer codes were written to analyze the inlet data and prepare them for use in simulations. The computer code would take the mean velocity data from each inlet plane and combine them into a common .csv file with the corresponding z coordinate for each plane. The turbulence parameters discussed above are also computed in this code, but an analyst should independently compute the necessary model parameters. This code is included in Appendix G. This code defines the inlet conditions for the CFD simulations. Post-processing the results from this code is required to use this inlet velocity profile in StarCCM+.

4.2.5 Boundary Layer

In the results obtained, there are several parameters that are used to describe the flow phenomena. These are not necessary considered as SRQ in this study, but some studies might consider them as such. Such parameters include the momentum thickness δ_2 with the corresponding momentum thickness Reynolds number Re_{δ_2}, the displacement thickness, and the boundary layer thickness. These parameters are reported along with the SRQ's in Chapter 5.

The boundary layer thickness is computed as [45]

$$\delta = 0.37x\mathrm{Re}_x^{-1/5}. \tag{4.32}$$

This equation is valid for local Reynolds number less than 10^8. Although this is just an approximation, it is useful for the comparison of turbulent boundary layer thickness growth. Other common boundary layer thickness quantities are discussed below. The approximation in Eqn. 4.32 is used because many of the measurements of the boundary layer velocity do not measure the free-stream velocity. Thus, a simple 99% of the free-stream is not feasible in all cases.

The momentum thickness is computed using its definition [18]

$$\delta_2 = \int_0^\infty \frac{\rho\overline{u}}{\rho_\infty\overline{u}_\infty}\left(1 - \frac{\overline{u}}{\overline{u}_\infty}\right) dy, \tag{4.33}$$

with an assumption. The density of air at the inlet is the same as the density of air in the boundary layer ($\rho = \rho_\infty$). The density at the inlet of the test section is nominally 1.01 kg/m^3 and the boundary layer density for air at the heated plate temperature is 0.9 kg/m^3. Using these two extremes, the ratio of densities is 0.9. Thus, the ratio of the densities is near unity for most of the boundary layer. For increased accuracy, the momentum thickness presented in this report should be corrected with the inlet density and boundary layer density profile. Future experiments will include measurement of the temperature profiles, providing data to compute the density ratio. A Matlab intrinsic trapezoidal integration is used and the code is included in Appendix I.

Another boundary layer quantity of interest is the displacement thickness [18]

$$\delta_1 = \int_0^\infty \left(1 - \frac{\overline{u}\rho}{\overline{u}_\infty \rho_\infty}\right) dy. \tag{4.34}$$

The ratio of the momentum thickness and the displacement thickness defines a boundary layer shape factor [18]. This is discussed in more detail later, when the boundary layer profiles have been presented. Again, the same assumption is made regarding the density ratio for the displacement thickness as was made for the momentum thickness.

4.3 Measurement of System Response Quantities

The measurement of the system response quantities is now described in more detail. Each SRQ section addresses the measurement of the SRQ, the analysis corresponding with the measurement and the uncertainty of the SRQ. Details and discussion of the results are included in Chapter 5 after the results are presented. The PIV equipment for each of these setups was described in Chapter 3.

4.3.1 Experimental Procedure

The procedure for acquiring the SRQ boundary layer velocity data is described in the following list. The SRQ data are all acquired using Orientations A (see Fig. 4.5).

1. Setup laser, camera, and respective traverse stages, and align calibration target.
2. Calibrate camera and match laser plane to calibration plane.
3. Set acquisition timing for sufficient particle displacements.
4. Set seeder flow rate.
5. Set laser intensity.
6. Set f-stop (which impacts particle image intensity and size).
7. Stabilize room, wall and flow conditions.

8. Record PIV data, temperatures, heat flux, equipment position, blower speed, heater and seeding settings, camera and laser settings, and room conditions.

9. Change boundary conditions (i.e. change flow rate from mixed to forced, or isothermal to constant flux), wait for stabilization of conditions, and take another data set.

As the design of the experiment was under consideration, the validation system response quantities were defined. Three heat flux sensors are embedded under the surface of the plate and the heat flux at their respective positions is used for three SRQ's. The sensors are described in more detail in Section 3.2.4.

The velocity field over the plate at the three heat flux sensor positions is used for another set of SRQ's. The velocities include $\overline{u}$, $\overline{v}$, $\overline{u'u'}$, $\overline{v'v'}$, and $\overline{u'v'}$. These velocities are measured using PIV at a high resolution using the calibration and analysis described in Chapter 3.2.5.

The friction velocity u_τ, which is defined as $u_\tau = \sqrt{\nu du/dy}$ where ν is the kinematic viscosity, is also a SRQ. In summary, the SRQ's measured are:

1. Boundary layer profiles at three x locations, including $\overline{u}$, $\overline{v}$, $\overline{u'u'}$, $\overline{v'v'}$, and $\overline{u'v'}$.

2. The heat flux at the same x locations.

3. The friction velocity u_τ.

4.3.2 Boundary Layer Velocity

The first SRQ is the boundary layer velocity profile at the three heat flux sensor positions. The $\overline{u}$, $\overline{v}$, $\overline{u'u'}$, $\overline{v'v'}$, and $\overline{u'v'}$ velocities are measured and used for SRQ's. For many common turbulence models, a CFD simulation may not compute the Reynolds stresses. In such cases, the turbulence kinetic energy is used for validation purposes. The turbulence kinetic energy is easily obtained from the experimental SRQ data.

The measurements are acquired using the steps outlined abaove and in Chapter 3.2.5. The camera and laser are setup in Orientation A (see Fig. 4.5), with the camera at an angle about x of around 5°. The small calibration plate is used to scale and dewarp the images. The plate is heated to 150° and the flow conditions are allowed to stabilize. Details regarding the equipment and measurement of velocity and the analysis of the PIV data was outlined in Chapter 3.2.5.

Uncertainty of all SRQ's must be reported. The repeatability of the boundary layer measurements is discussed in Chapter 5.4, as this analysis is only performed after data acquisition. The method used to determine the uncertainty of the PIV velocity measurements is outlined in the literature using an uncertainty surface method [13, 14]. The uncertainty of the position is discussed later.

4.3.3 Heat Flux

The heat flux is more difficult to both compute and measure than the velocity. It was selected to provide a wider range in the difficulty spectrum for validation [3]. The heat flux is measured using the heat flux sensors at the positions described previously. The sensors are embedded a small distance from the surface of the plate.

A possible limitation of this design is the assumption that no axial conduction takes place. The heat flux sensor has some material between it and the plate surface where conduction could move measured heat flux to another location. The measured heat flux is assumed to be the entire heat flux into the flow (convection/radiation). To mitigate this error, thermal gradients in the plate are kept small and all of the data presented herein is steady-state. Correlations are used to compare with the experimental measurements and CFD computations. These are described for each case in Chapter 5.

4.3.4 Friction Velocity

The friction velocity u_τ is obtained in one of two ways. The first is to use a linear fit of the first several data points of the velocity in the boundary layer near the wall to obtain $\partial u/\partial y$. This method has many limitations, including a high susceptibility to position error. That position error can come from error in wall position (which is normally specified by the experimentalist), or an error from non-uniform seeding in interrogation regions in the PIV processing.

The second method used to obtain the friction velocity is to use a fit to a Spalding profile, as outlined by Kendall and Koochesfahani [49]. The quantities u_τ, κ, B, and y_0 can be found by fitting the measured PIV profiles to the Spalding profile and optimizing the fit to compute the friction velocity, and other relevant parameters, including the wall position. The equation for the Spalding profile is

$$y^+ = u^+ + \exp(-\kappa B)\left[\exp(\kappa u^+) - 1 - \kappa u^+ - \frac{(\kappa u^+)^2}{2} - \frac{(\kappa u^+)^3}{6}\right] \tag{4.35}$$

where $y^+ = (y - y_0)u_\tau/\nu$ and $u^+ = \overline{u}_\infty/u_\tau$.

The Spalding fit method outlined in [49] is only valid for fully turbulent flow. In the forced convection regime where buoyancy forces are insignificant compared to inertial forces, the fit is more applicable than in situations where the buoyancy forces are more dominant. These ratios were discussed in Chapter 1.

The uncertainty of the wall shear velocity u_τ based on examination of the gradient at the wall is found using the Taylor Series Method [17] and the data reduction equation $u_\tau = \sqrt{\nu du/dy}$. The uncertainty of the shear velocity is

$$U_{u_\tau} = \sqrt{\left(U_{du/dy}\frac{\sqrt{\nu}}{2\sqrt{du/dy}}\right)^2 + \left(U_\nu\frac{\sqrt{du/dy}}{2\sqrt{\nu}}\right)^2}, \tag{4.36}$$

where U_ν is the uncertainty of the kinematic viscosity, Eqn. 4.14, and $U_{du/dy}$ is the uncertainty of the velocity gradient

$$U_{du/dy} = \sqrt{\left(\frac{U_{u1}}{dy}\right)^2 + \left(\frac{U_{u2}}{dy}\right)^2 + \left(U_{dy}\frac{u1 - u2}{dy^2}\right)^2} \tag{4.37}$$

where the velocity uncertainties are computed using the methods described in [13–16] and the velocities are data points in the velocity profile. The dy term is the vector spacing of the data and the uncertainty of dy is explained below.

The dynamic viscosity μ was defined in Eqn. 4.15 and its uncertainty described, along with the air density computation and its uncertainty. The uncertainty of temperature

$U_T = 0.6$°C and the uncertainty of pressure $U_P = 1.5\%$ of reading.

The uncertainty of the position of the PIV data can be a significant contributor to the uncertainty of the friction velocity (and velocity itself). The most obvious method for setting an origin is to locate an non-moving object (such as the wall) in the raw PIV images. However, the laser source commonly generates a wide flare in the camera image at the wall making it difficult to pinpoint its location. An example is shown in Fig. 4.7 which shows a small part of the image. The wall is the white band near the left side of the image.

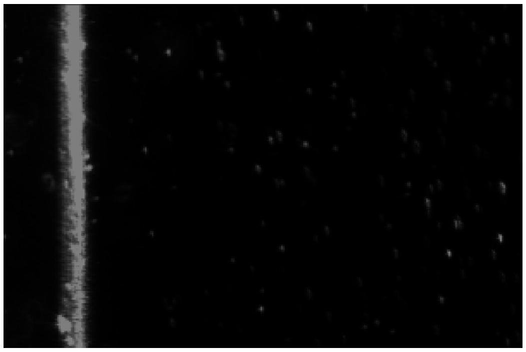

Fig. 4.7: An image of the wall, with the image width being 2.25 mm.

This estimate can be improved upon using information from the turbulent flow along a wall. The error in the wall location was found first by fitting theoretical (Spalding) velocity profiles to the hundreds of streamwise time-averaged velocity data points (some of which are located in the viscous sublayer, and most of which are in the log layer), and using the wall location as a parameter of the fit. In addition, the wall location is found by fitting a line through the three velocity values closest to the wall. These should behave linearly and go to zero at the wall. It was found that replications of this process, with the measurement system set up from scratch each time, resulted in large variations in the wall location error.

Seven replications are shown in Fig. 4.8. The error δy of each method relative to the wall location based on inspection are shown. For both methods, the variations in the wall position error were on the order of 16 pixels. The average of these samples could be viewed as the bias of each method relative to the wall location by inspection. Unfortunately, we have no evidence that any one of these methods is clearly superior to any other, but these data are sufficient to provide a reasonable uncertainty estimate of the wall location.

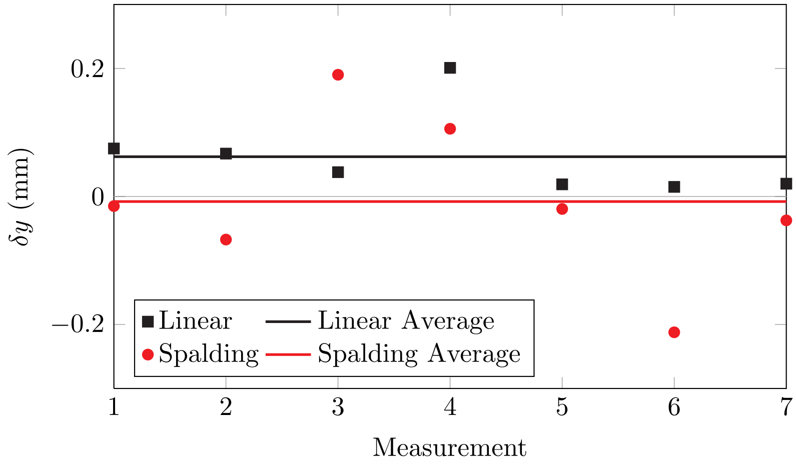

Fig. 4.8: The error of the wall location computed using three methods with the image estimate being the basis for the error and a scale factor of around 84 pixels/mm.

4.4 CFD Simulation Procedure

The CFD simulations are conducted using STAR-CCM+ from CD-adapco [50]. A best estimate for the appropriate turbulence models is used, since the validation of the models is not in the scope of this work. Use of these models is based on preliminary simulation work done by Iverson [48].

4.4.1 Geometry and Mesh

The geometry was modeled using the as-built measurements of the test section. The 7 planes of measured dimensions were used to define the air volume of the wind tunnel. This volume was exported as a parasolid. The parasolid file was imported to STAR-CCM+ and the regions defined as necessary (inlet, outlet, heated wall and three walls). The as-built dimensions are shown in Table 4.2. The assumptions that are used in building this geometry include: the heated plate is flat, the seven reference cross-sections are lined up on that flat plate, the corners nearest the heat plate are right angles.

The mesh was generated using the directed mesher function in StarCCM+. The square test section allowed for a simple mesh to be created using the directed mesher. The patch mesh (the source of the mesh that is extruded through the volume) uses a two sided hyperbolic distribution with end spacing define as in Table 4.4.

Three meshes were constructed on the geometry, and the parameters are shown in Table 4.4, where the Average Volume is the average cell volume of the cells nearest the heated plate. These meshes were constructed based on the y^+ computed using the mixed buoyancy opposed boundary conditions. The M2 mesh was defined to keep the wall y^+ below 1, then the other two meshes were defined such that the cell height ratio between the near wall cells was 2. The means that $dy_{\mathrm{M1}} = 2dy_{\mathrm{M2}} = 4dy_{\mathrm{M3}}$, where dy is the cell height of the near wall cell.

Table 4.4: The mesh properties for the three meshes used in the GCI analysis. The mesh cell count, average volume of cells, near wall cell height, and several GCI parameters and heat flux results are tabulated.

Mesh	Cells	Avg. Vol.	dy	r	y^+	q''_1	q''_2	q''_3
M1	12600000	5.61E-10	0.0358 mm	r_{21}=2.00	0.44	1609.6	1099.6	1070.4
M2	1575000	4.52E-09	0.0716 mm	r_{32}=2.02	0.87	1641.1	1142.7	1103.6
M3	191660	3.73E-08	0.1432 mm		1.75	1110.2	1175.9	1128.1

These meshes are all used to compute the grid convergence index (GCI) based on the heat flux at the three heat flux sensor positions (although the measured heat flux has nothing to do with this GCI analysis). Following the procedure outlined by the Journal of Fluids Engineering [51], the GCI was computed. First, the length scale dy was defined as the height of the near wall cells which was computed from the cube root of the average near wall cell volume. The ratio between dy for the several meshes was 2. Second, the resultant heat flux at a certain position (such as the first heat flux sensor) was recorded from the simulations at each mesh refinement (M1, M2, and M3). Third, Eqns. 4.38, 4.39, 4.40, and 4.41 are used to compute the GCI in Eqn. 4.42. In Eqns. 4.38 and 4.40, ϵ_{21} and ϵ_{32} are simply the difference between the resultant heat fluxes from the respective simulations ($\epsilon_{21} = q''_{M2} - q''_{M1}$).

$$p = \frac{1}{\ln r_{21}} \left| \ln \left| \epsilon_{32}/\epsilon_{21} \right| + q(p) \right| \tag{4.38}$$

$$q(p) = \ln \left(\frac{r_{21}^p - s}{r_{32}^p - s} \right) \tag{4.39}$$

$$s = 1 \cdot sgn(\epsilon_{32}/\epsilon_{21}) \tag{4.40}$$

$$e_a^{21} = \left| \frac{q_1'' - q_2''}{q_1''} \right| \tag{4.41}$$

$$GCI_{fine}^{21} = \frac{1.25 e_a^{21}}{r_{21}^p - 1} \tag{4.42}$$

Equation 4.42 represents the discretization error on the fine mesh based on the heat flux computed. It is noted that iterative convergence is achieved in these simulations as each equation's residuals decrease more than four orders of magnitude [51]. Table 4.5 shows the GCI results for this study.

Table 4.5: The GCI results using the methods described above for heat flux at the first sensor position.

Position	p	q	e_a^{21}	e_a^{32}	GCI^{21}	GCI^{32}
P1	4.01	-0.03	31.6	-530.9	0.002	0.026
P2	0.39	-0.01	43.0	33.2	0.158	0.116
P3	0.46	-0.01	33.2	24.5	0.103	0.073

4.4.2 Boundary Conditions and Physics

The boundary conditions for the walls are defined from the measured boundary conditions. Each of the four walls was set to the temperatures measured in the experiment, as described in Chapter 3.2. The temperature from the experiment was recorded in a .csv file that is imported into StarCCM+. The columns of the file are x, y, z, and the temperature.

The inlet temperature was defined in a similar fashion, along with the relevant turbulence model inputs (such as k, ϵ, or ω).

All of these boundary conditions are necessarily interpolated spatially (the measurements are much too coarse to be used directly in the simulation, and STAR-CCM+ does not interpolate the boundary condition tables). The interpolation codes are included in Appendix H. One code interpolates the inlet velocity components, turbulence kinetic energy, and turbulence dissipation rate ϵ. The second code interpolates the plate temperature and the inlet temperature. The variation in the other three wall temperatures is small, so interpolation is unnecessary.

Since a few turbulence models are considered, there are several physical parameters in the simulations that are all consistent. The consistent physics settings for the simulations include:

1. Steady State - the simualations included herein do not change in time
2. Coupled energy/momentum - the heat transfer contributes to changes in momentum
3. Ideal Gas - we assume air is an ideal gas
4. Turbulent - we assume that all flow scenarios presented are turbulent
5. Gravity - the models include body forces due to gravity

4.4.3 Models

The selected models are based on the work done in [48]. For the mixed convection buoyancy aided flow, the Standard k-ϵ Low Reynolds number is used, with an all $y+$ wall treatment [52]. This model is better than the standard k-ϵ model because it utilizes damping functions which allow the solver to compute in the viscous-affected region near the heated wall [50].

The forced convection buoyancy aided flow simulations use a Standard (Wilcox) k-ω model [53]. These simulations also use an all $y+$ wall treatment. In these buoyancy aided solutions, the Courant Number was increased to decrease solution computation time.

Mostly, the default settings were used in these models. In all cases, the residuals started at unity and decreased more than 6 orders of magnitude.

4.5 Quality Assurance

To ensure the experiment design, data acquisition, and analysis are sufficient to meet project funding agency requirements, the NEUP QA Requirements are used [54]. A summary of the requirements is included below:

- Equipment Calibration and Documentation
    - Specified requirements of accuracy, precision of equipment
    - Measurement uncertainty is documented
    - All equipment is controlled
    - Equipment calibration is recorded
- Analysis/Modeling V&V
    - Documented software used in analysis
    - Modeling uses software packages that have received V&V, with referenced software version
- Records
    - Regularly used laboratory notebook to record project work activity
    - Electronic records kept and backed up
- Data Acquisition and Analysis
    - Testing of data acquisition equipment before data collection
    - Investigation of data anomalies
    - Define the assumptions stated in data analysis, methods used to identify and minimize uncertainty, and the analytical models used

4.6 Data Recording, Storage, and Backup

All data are written to removable hard drives in the PIV computer. When the drive is full, it is moved to another location for future use. As all of the data are recorded digitally, it is necessary to back up the data to another site. A system is built in a different building that houses several hard drives. The PIV data and other relevant recordings are uploaded to those hard drives as a second copy. All data are stored in a hard drive in the Experimental Fluid Dynamics Laboratory and backed up to a remote location in the main Engineering building at USU.

Chapter 5

Results

The results from the experiment are presented and discussed in this chapter. The boundary conditions acquired for the cases are presented here, and the data are available on the project website. The SRQ results are presented along with the SRQ results from the simulations. Some discussion and comparison is provided. Finally, the uncertainty of the measurements are presented. In the discussion, several cases are referred to using the heating condition “constant heat flux.” This nomenclature is used because the three heat flux sensors are used to fix the heat flux at a specified value. However, the second sensor is known to have a higher uncertainty than the other two sensors, invalidating it’s nomenclature as constant heat flux. The case is valid as a different heating condition than the isothermal cases, but it should be understood that constant heat flux is not exactly the heating condition on the plate.

5.1 Boundary Conditions

The boundary conditions are measured every time PIV data are acquired. For each case, there are 9 PIV inlet planes and 3 PIV SRQ measurements, making 12 boundary condition data sets for each flow scenario. For instance, the isothermal forced convection buoyancy aided case has 12 measurements of the boundary conditions. The 12 sets of boundary conditions are averaged together and used for the buoyancy aided isothermal forced convection boundary conditions. The sample size requires a Student-t distribution to quantify the precision uncertainty of the boundary conditions [18].

The spanwise centerline $z = 0$ temperature profiles are shown in Fig. 5.1 for the cases under consideration. The isothermal cases (forced and mixed) are quite similar, as the control software compensates for the change in flow rate to hold the near-uniform temperature. The discrepancy of 1.7° at the first thermocouple is due to the nature of the power supplied to the heaters, as discussed in the following paragraph. The constant flux cases have an average temperature difference of 1.2%. This figure should be referred to when the difference in plate temperature is referenced in later discussions.

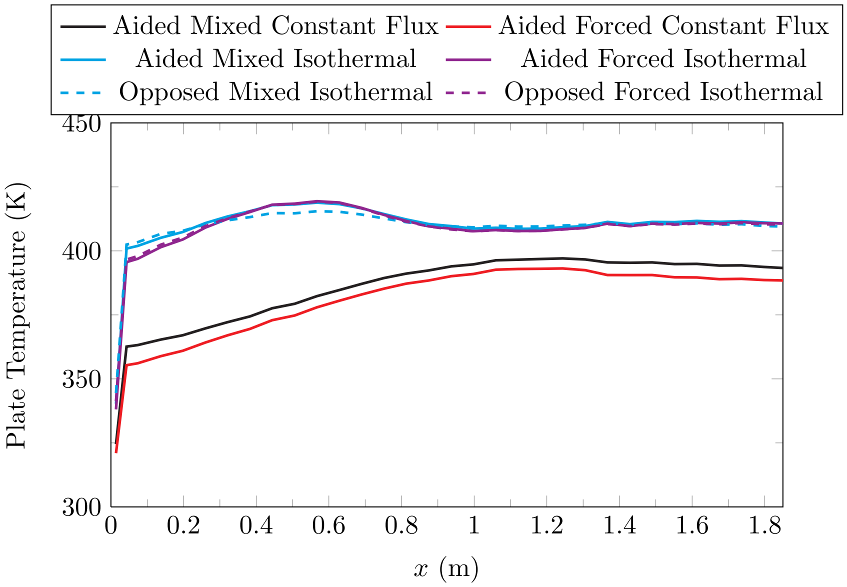

Fig. 5.1: The centerline ($z = 0$) temperature profiles for the buoyancy aided cases.

The forced convection isothermal case cools the first heated section more than the mixed convection case, therefore decreasing the temperature. This is observed in the heat flux trends discussed later. The power supplied to heaters 1 and 2 are governed by the temperature at the center of heater 1, $x = 5.87$ in. (see Fig. 3.6). The limited power allowed to the heaters kept the forced convection case cooler than the mixed convection case at the first heater. The power supplied to the first two heaters was at maximum for the forced convection case but not for the mixed convection case. The plate temperatures would be identical if the heaters could safely provide more power. This is also apparent in Fig. 5.2 where the constant power to heaters 1 and 2 create a cooler leading edge and a too warm region over heater 2.

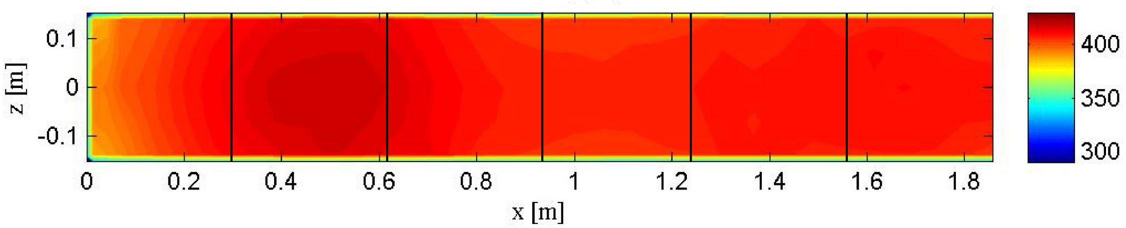

Fig. 5.2: The temperature contour for the aided isothermal forced convection case, showing the hot spot at the second heater. The segments show the heaters.

The centerline plate temperature for the buoyancy aided and buoyancy opposed isothermal cases are nearly identical when comparing the mixed aided to the mixed opposed, and similarly for the forced aided to forced opposed ceterline temperatures. The buoyancy aided and opposed cases were acquired several months apart, with a rotation of the wind tunnel 180° in between. The plate temperature showing this repeatable boundary condition for forced isothermal convection is shown in Fig. 5.1.

It is noted that the cases labeled "constant heat flux" are not actually constant heat flux. The second heat flux sensor is suspected to have elevated uncertainty compared with the other two sensors. Since this is one of the control parameters for driving the heated wall boundary conditions, it cannot be considered as "constant heat flux." However, the case is still valid as a comparison with a different temperature profile on the heated wall.

5.2 System Response Quantities

A summary of the cases is included in Table 5.1. The hydraulic diameter is 12 inches. The CFD results presented are calculated from the models outlined in Chapter 4.4.3. The system response quantities in this study include the boundary layer velocity profiles near the heated wall and the heat flux from the wall. At the same location as the heat flux sensors, the boundary layer profiles are measured with the PIV system, and the uncertainty is quantified using the uncertainty surface method described in Section 1.2. A third SRQ to consider is the friction velocity, u_τ.

Table 5.1: The several cases considered in the study.

Case	Re_{D_h}
Aided Forced Isothermal	75,900
Aided Mixed Isothermal	44,100
Aided Forced Constant Flux	75,800
Aided Mixed Constant Flux	44,400
Opposed Forced Isothermal	77,900
Opposed Mixed Isothermal	44,600

5.2.1 Isothermal Buoyancy Aided Forced Convection

The first system response quantity for the buoyancy aided isothermal forced convection case is the boundary layer velocity. The measured velocity profiles with uncertainty bands are shown in Fig. 5.3. The $\overline{u}$ component of velocity and the Reynolds normal stress $\overline{u'u'}$ with 95% confidence are shown in Fig. 5.3(a). The y direction velocity $\overline{v}$ is shown in Fig. 5.3(b) with the other two measured components of the Reynolds stress $\overline{v'v'}$ and $\overline{u'v'}$.

In Fig. 5.3(a), the velocity profile at the first position appears to be higher in magnitude than the other two positions. This is because the flow is developing, and the profile at the first position is not fully developed. The second and third positions show a more developed velocity profile. The Reynolds normal stress has the standard trend expected for boundary layer flow. It is noted that at the first position, the Reynolds stress decreases as the flow approaches the free stream. The free stream is not measured in the other two positions, so the Reynolds stress at P1 and P2 show a different slope. The Reynolds stresses at P2 and P3 are nearly the same. The first position again shows a different trend than the more developed second and third position's Reynolds stress.

Figure 5.3(b) shows the cross-stream velocity component and two other measurable quantities of the Reynolds stress. The velocity in the boundary layer has a slight trend toward the wall at all three positions. However, the values are very small compared to the streamwise velocity component (around 1% of the streamwise velocity). The uncertainty of $\overline{v}$ is about the same order as the $\overline{v}$. This does give further justification for our treatment at the inlet of the test section for this buoyancy aided isothermal forced convection case.

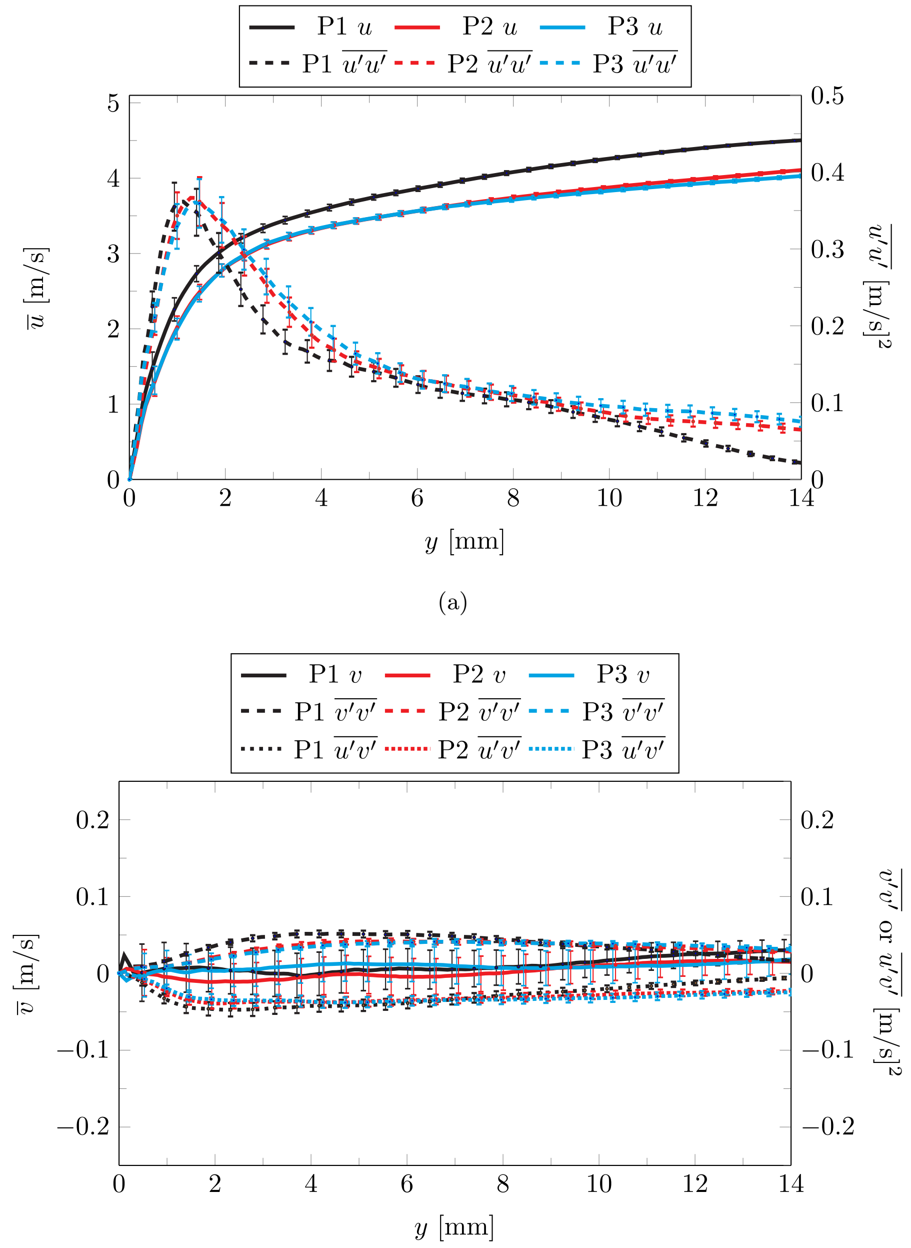

(a)

(b)

Fig. 5.3: The boundary layer velocity profiles for buoyancy aided forced convection with isothermal heating. (a) shows the streamwise component of velocity and Reynolds Stress. (b) shows the cross-stream component of velocity and the two other measured components of the Reynolds Stress. Recall that P1 is $x = 5.87$ in., P2 is $x = 30.12$ in., and P3 is $x = 54.87$ in.

The SRQ's presented in Fig. 5.3 are compared in Fig. 5.4 with the corresponding SRQ's from the CFD simulation that use the measured boundary conditions for this case. Figure 5.4(a) shows the boundary layer streamwise velocity component for both the experimental and CFD. The turbulence kinetic energy $\overline{k}$ (TKE) is shown in Fig. 5.4(b). The turbulence kinetic energy is used for comparison (instead of $\overline{u'u'}$ etc.) as the CFD models employed do not compute the Reynolds stresses directly (some discussion relating to the Reynolds shear stress is included in Section 5.3.4). The $\overline{k}$ for the experimental measurements are calculated using the definition of the turbulence kinetic energy and assuming that $\overline{v'v'} = \overline{w'w'}$. Note that these plots do not represent a validation study. They simply demonstrate that the measured boundary conditions are sufficient for the CFD simulations.

In Fig. 5.4(a), the first position CFD simulation is furthest from the measured velocity profile. The other two positions are more consistent, but still show noticeable error from the measured velocity profile. It appears that the CFD simulation free stream velocity might be more accurately predicted than the boundary layer velocity, based the converging trend of each profile with it's CFD computed profile. Figure 5.4(b) shows that the CFD simulation predicts the TKE to within the measured uncertainty near the wall for the second and third positions. The first position is poorly predicted by the CFD. However, the CFD TKE is within the experimental uncertainty for most of the boundary layer velocity profile for the third position. The first and second position CFD TKE profiles are not within the measurement uncertainty.

Non-dimensional plots of the boundary layer velocity are presented in Fig. 5.5 using the standard wall coordinates y^+ and u^+. The quantities required to compute the wall coordinate profiles, namely u_τ, κ, y_0, and B can be found using the method described by Kendall and Koochesfahani [49]. A curve fit to the Spalding profile yields shear velocities shown in Table 5.2, where the Spalding profile is given in Eqn 4.35. Two results are shown for each profile: one using the standard values $\kappa = 0.41$ and $B = 5.0$ and a second where κ and B are found in the fitting process along with the wall position y_0 and friction velocity. Care was taken to exclude wake region data for the curve fit. The simulation u_τ is found

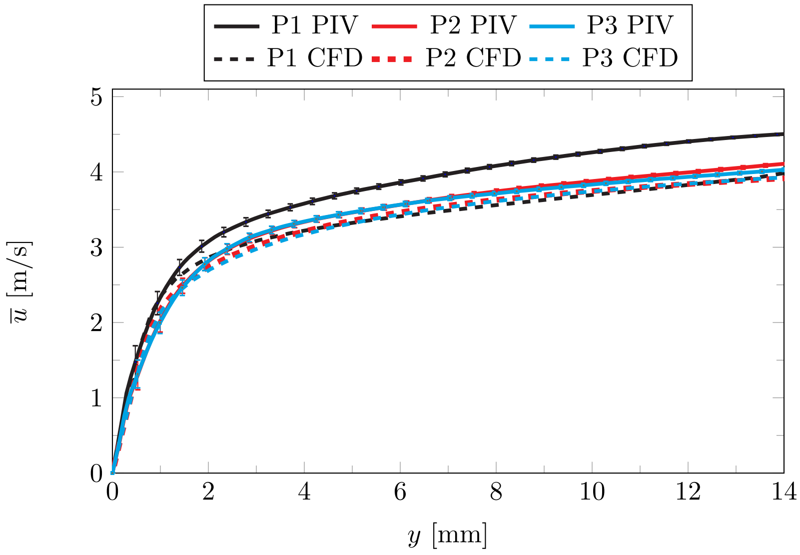

(a)

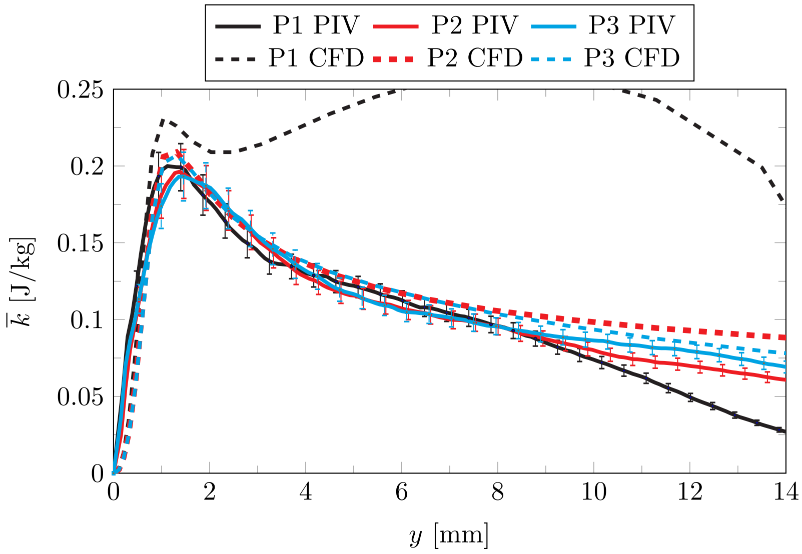

(b)

Fig. 5.4: The boundary layer velocity profiles for buoyancy aided forced convection with isothermal heating compared with CFD results using the same boundary conditions. (a) shows the streamwise component of velocity. (b) shows the turbulence kinetic energy profiles.

by plotting the density and shear stress as a function of x on the heated wall with $z = 0$. Then the friction velocity is computed using it's definition, $u_\tau = \sqrt{\tau_s/\rho}$. A linear fit to the first three valid vectors is also used to compute the shear velocity.

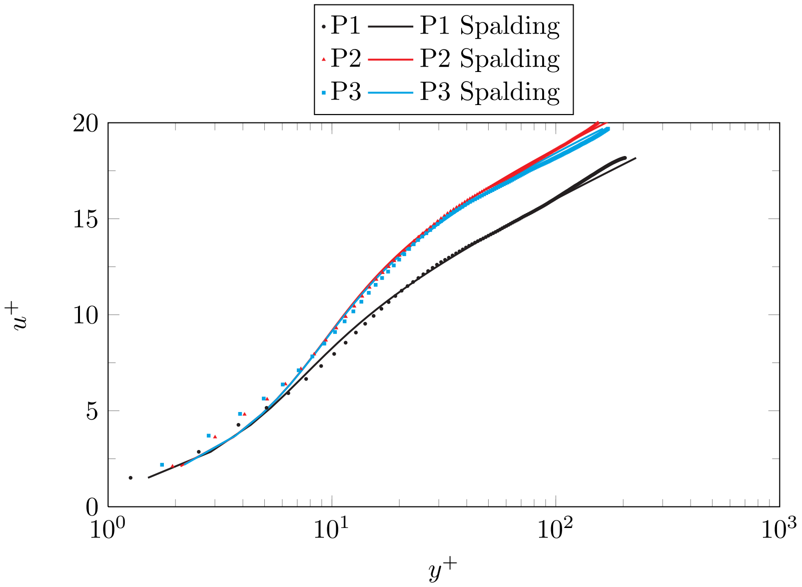

Fig. 5.5: The wall coordinate boundary layers for the three heat flux sensor positions for buoyancy aided isothermal forced convection flow and the Spalding fit profiles for comparison.

The profiles shown in Fig. 5.5 show that the curve fit does not match the data in every region of the boundary layer. The most reliable velocity data to use for the Spalding fit is inside of the wake region and outside of the viscous sublayer. Since the fit excludes the data in the linear and wake regions, the fit and the data are unmatched in the those regions. This slight discrepancy between the data and the fit has little impact on the resulting shear velocity, but does change the trend of the wall coordinate profiles.

Table 5.2 shows that there is a range of friction velocities that can be computed using the methods outlined. For this case, the CFD and the Spalding fit are in closer agreement than the linear fit friction velocity, particularly at the second and third positions. Using the shear velocities shown in Table 5.2, the wall coordinate profiles for velocity at the heat flux sensor positions are shown in Fig. 5.5. Each profile is compared with its respective Spalding profile using the 4 parameter fit. The code to fit the data to the Spalding profile is included in Appendix J.

The values of the shear velocity in Table 5.2 show a range of magnitudes. For forced

Table 5.2: The von Kármán constant, intercept, shear velocity from the Spalding fit, and the shear velocity from a linear fit near the wall at the heat flux sensor positions for the buoyancy aided isothermal forced convection case. The computed friction velocity from the CFD simulation is also tabulated.

Position	κ	B	u_τ Spalding	u_τ Linear	u_τ CFD
P1	0.41	5.00	0.248	0.258±0.004	0.215
P1	0.43	6.60	0.235		
P2	0.41	5.00	0.234	0.230±0.004	0.231
P2	0.42	8.17	0.204		
P3	0.41	5.00	0.235	0.230±0.004	0.233
P3	0.43	8.04	0.210		

convection, the Spalding fit is assumed to be more correct than a linear fit. The velocity data points nearest the wall are the most uncertain, so it seems reasonable that using more data points with the Spalding fit is more accurate. The CFD shear velocity presents the wrong trend entirely, increasing along the streamwise direction. A high value of the shear velocity at the first position is expected to correspond to the highest value of heat flux from the plate. The shear velocity is based on the velocity gradient, and a high gradient near the wall often means a thinner boundary layer. The temperature gradient in the thin boundary layer corresponds to a higher heat flux. The drop in shear velocity from P1 to P2 is expected to decrease the heat flux. The shear velocity trend from P2 to P3 does not decrease significantly for either of the Spalding or linear fits. This suggests that the heat flux should not decrease from P2 to P3. This is shown in Fig. 5.6, where the heat flux at P3 is actually greater than that at P2.

The measured heat flux at the three heat flux sensors is shown in Fig. 5.6. The measured heat flux is the reading from the sensors described in Chapter 3.2.4 and is an ensemble average of the 12 acquisition cases for the forced isothermal condition. The trend labeled Kays is the heat flux predicted by Eqn. 5.1 [18, pg. 249]. The Incropera trend is based on the correlation for convection over an isothermal flat plate, shown in Eqn. 5.2 [45, pg. 411]. The Stanton number is the Nusselt number divided by the product of the Reynolds and Prandtl numbers. Once the Nusselt number is computed, the heat flux can be found as $q'' = \mathrm{Nu_x} k(T_x - T_\infty)/x$. It is noted that these correlations may have an error as high as 25% [45].

$$\mathrm{St} = \frac{\mathrm{Nu}_x}{\mathrm{Re_x Pr}} = \frac{0.0287\mathrm{Re_x^{-0.2}}}{0.169\mathrm{Re_x^{-0.1}}(13.2\mathrm{Pr} - 9.25) + 0.85} \tag{5.1}$$

$$\mathrm{Nu_x} = 0.0296\mathrm{Re}_x^{4/5}\mathrm{Pr}^{1/3} \tag{5.2}$$

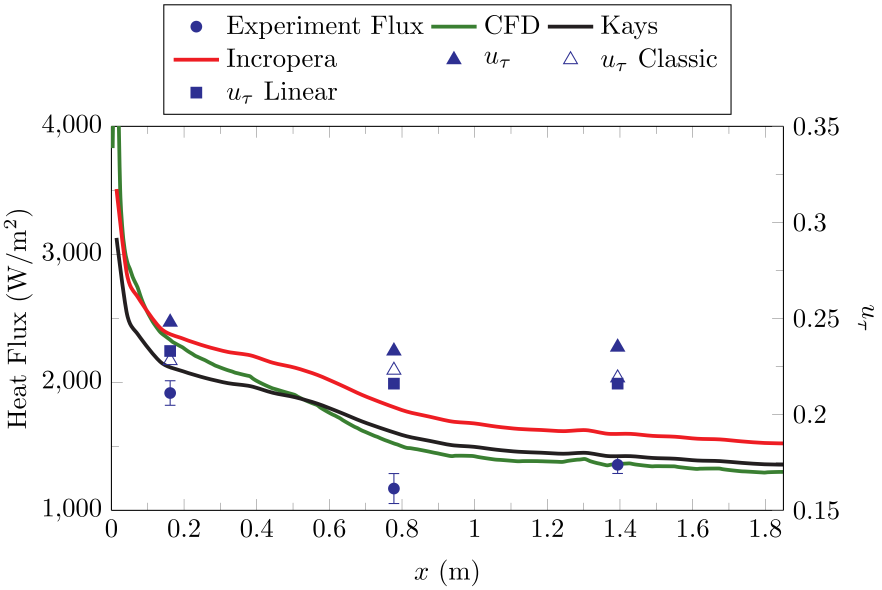

Fig. 5.6: The heat flux compared with a CFD simulation and two correlations for the buoyancy aided isothermal forced convection case. The shear velocity from the several methods is also plotted.

Figure 5.6 also shows the computed streamwise variation in heat flux from the CFD simulation along the center ($z = 0$) of the heated plate. The experimental measurements and the CFD computation have very similar heat flux responses at the first and third positions. The second position is quite different with the heat flux, being outside of the measurement uncertainty. The correlations show a similar trend to the results and simulation, but have noticeably different magnitude.

In this case (and all of the isothermal cases) the plate is heated to a nominally isothermal condition of 150°C. The controller seeks isothermal heating, but the boundary condition thermocouples are much more resolved spatially than the PID controller (which uses only three temperature readings), limiting the ability to actually achieve isothermal heating. The corner of the leading edge is 30°C cooler than the hottest spot in the entire plate. The plate temperature contour for this case is shown in Fig. 5.2.

The heat flux, Reynolds number, surface temperature, and Grashof to Reynolds squared ratio are shown in Table 5.3, along with several of the boundary layer thicknesses and the momentum thickness Reynolds number. The flow at the location of the third heat flux sensor is nearing the boundary of forced convection based on [18]. Kays and Crawford show that the critical momentum thickness Reynolds number is 162 [18], which is exceeded at all three positions.

Table 5.3: The buoyancy aided isothermal forced convection heat flux results along with the Grashof to Reynolds number ratio (showing the cases are forced convection) and the momentum thickness Reynolds number.

x Position (in)	Flux (W/m^2)	Re$_x$	Temp. (K)	Gr$_x$/Re$_x^2$	δ (mm)	δ_1 (mm)	δ_2 (mm)	Re$_{\delta_2}$
P1 = 5.87	1917	40,300	403	0.026	7.18	2.2	1.4	357
P2 = 30.12	1170	194,000	413	0.131	25.2	3.3	2.2	554
P3 = 54.87	1356	347,000	410	0.232	40.2	3.4	2.3	564

The development of the boundary layer from position 1 to 2 to 3 is shown in Fig. 5.3, where it appears that positions 2 and 3 have nearly the same boundary layer. This is confirmed by the momentum thickness Reynolds number Re$_{\delta_2}$ in Table 5.3, where the second and third positions are higher in magnitude than the first position momentum thickness Reynolds number.

5.2.2 Isothermal Buoyancy Aided Mixed Convection

The measured boundary layer velocity profiles for the buoyancy aided isothermal mixed convection case are shown in Fig. 5.7. The streamwise velocity and Reynolds normal stress profiles are shown in Fig. 5.7(a) and the cross-stream velocity and Reynolds stress profiles are shown in Fig. 5.20(b). The effects of buoyancy on the flow is observable when comparing the trends in Fig. 5.7(a) with the forced case shown in Fig. 5.3. The trends shown in Fig. 5.7 suggest a laminarization of the flow at this flow speed and plate temperature. Figure 5.7(a) shows that the first and third positions have nearly the same boundary layer velocity profile. The trend from the first to the second suggests a thickening of the boundary layer, as was the case in Fig. 5.3. However, the trend from P2 to P3 shows that the flow has reverted to a similar boundary layer velocity profile as the one at P1. The cross-stream profile of velocity and Reynolds cross-stream normal and shear stress are shown in Fig. 5.7(b). The $\overline{v}$ component of velocity is negative, suggesting an average flow toward the plate. However, the values are very small with particle displacements in the y direction of less than 0.3 pixels. The streamwise particle displacements are around 16 pixels. The two measured quantities of Reynolds stress are practically zero for this case suggesting a lack of turbulent mixing.

The boundary layer velocity profiles in Fig. 5.7 are compared in Fig. 5.8 with CFD simulation results for this case. The boundary conditions measured during the SRQ data acquisition were used in the CFD simulation. The CFD simulation fails to compute the boundary layer velocity profiles within the measurement uncertainty. The laminarization trend does not exist in the CFD simulation and the boundary layer velocity profiles from the CFD show a more turbulent boundary layer velocity profile than the measurements show. The CFD model fails to accurately predict the TKE at the first heat flux sensor position. The TKE at the other two positions are closer to the measured trends than the first position, but still not within the measurement uncertainty.

Flow laminarization is discussed by Kays and Crawford [18], McEligot and Jackson [21], and Perkins *et al.* [34]. In the literature, an acceleration parameter is defined as

$$K = \frac{\nu}{u_\infty^2}\frac{du_\infty}{dx}. \tag{5.3}$$

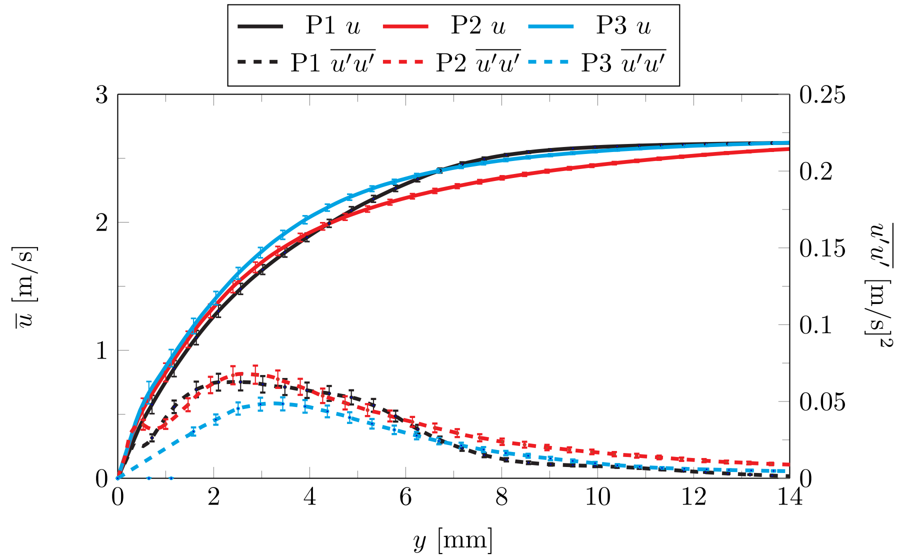

(a)

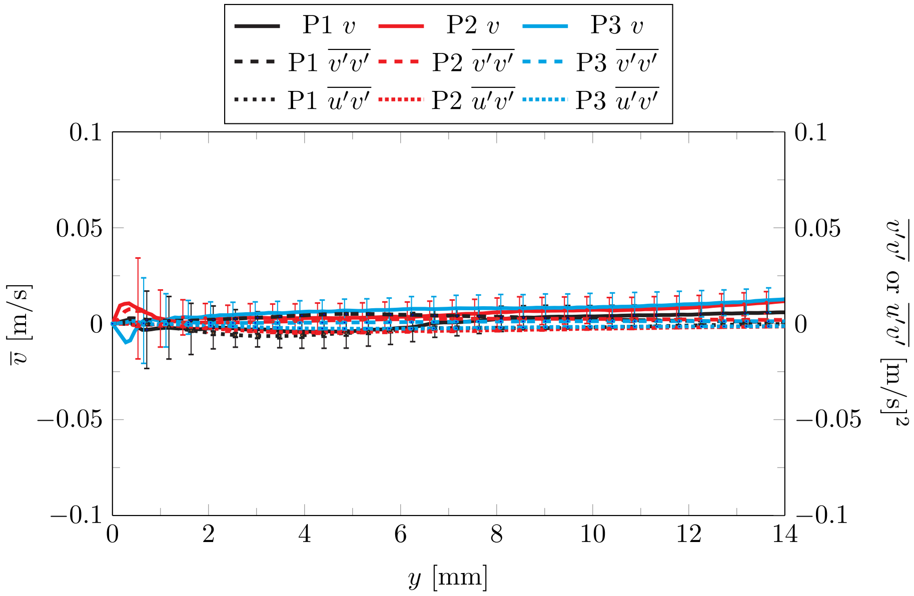

(b)

Fig. 5.7: The boundary layer velocity profiles for buoyancy aided mixed convection with isothermal heating. (a) shows the streamwise component of velocity and Reynolds Stress. (b) shows the cross-stream component of velocity and the two other components of the Reynolds Stress.

This parameter is found using the relation

$$p^+ = \frac{K}{(c_f/2)^{3/2}} = \frac{\mu \, d\overline{P}/dx}{\rho^{1/2}\tau_s^{3/2}} \tag{5.4}$$

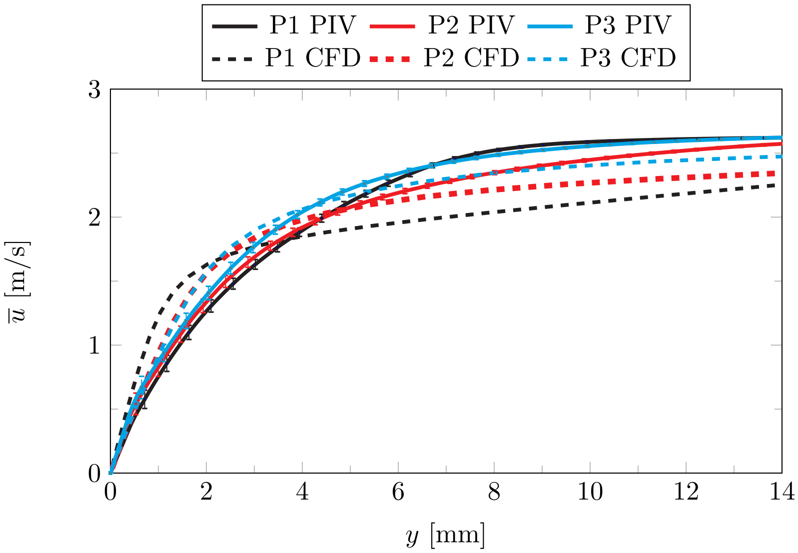

(a)

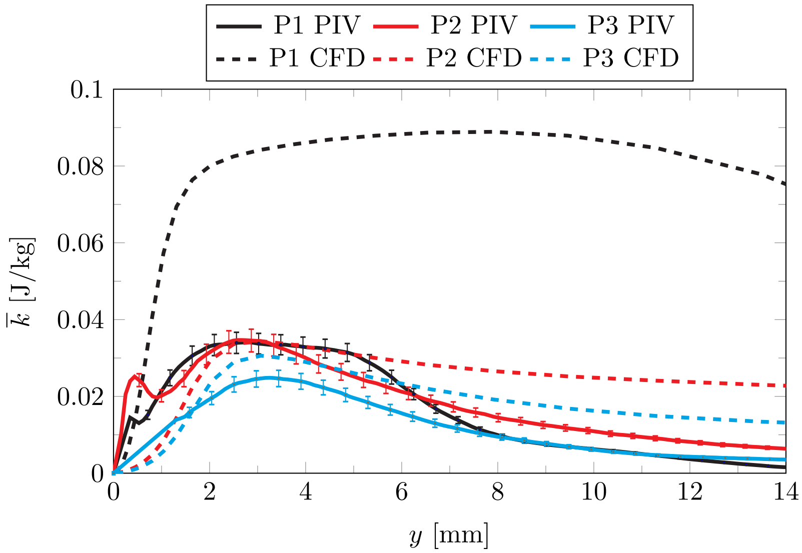

(b)

Fig. 5.8: The boundary layer velocity profiles for buoyancy aided mixed convection with isothermal heating compared with CFD results using the same boundary conditions. (a) shows the streamwise component of velocity. (b) shows the turbulence kinetic energy.

and the definition of the pressure gradient parameter p^+.

The pressure drop through the test section ($d\overline{P}/dx$) is measured when the SRQ data are acquired using the installed pressure taps. The shear stress is found using the gradient of the velocity data near the wall and the air properties are found using the measured atmospheric conditions. For the mixed isothermal buoyancy aided case, the acceleration factor K is computed to be 2×10^{-6}. This is near the suggested laminarization point of $K = 3 \times 10^{-6}$, so we would expect some laminar-like behavior of the flow [18, pg. 211].

The friction velocity analysis for the mixed convection cases was inconclusive. Several methods were attempted to compute the shear velocity, but none were physically sound. The velocity profiles near the wall are not linear, negating the validity of the linear approximation for computing the velocity gradient. Thus, the measured shear velocity as a SRQ is not available.

The measured heat flux for the buoyancy aided isothermal mixed convection case is shown in Fig. 5.9, compared with the CFD heat flux and two correlations. The correlations are based on the theory presented in the literature where the mixed convection Nusselt number is the sum or difference of the forced convection and natural convection Nusselt numbers [18,45]. The natural convection Nusselt correlation was shown in Eqn. 4.3.

The mixed convection Nusselt number is shown in Eqn. 5.5, where the sum is used for buoyancy aided flow and the difference is for buoyancy opposed. The forced convection Nusselt number Nu_F is provided in Eqns. 5.1 and 5.2. In Fig. 5.9, the Kays correlation is the combination of Eqn. 5.1 and Eqn. 4.3. The Incropera correlation in Fig. 5.9 is the combination of Eqns. 5.2 and 4.3.

$$\mathrm{Nu}_{\mathrm{mix}}^3 = \mathrm{Nu}_{\mathrm{F}}^3 \pm \mathrm{Nu}_{\mathrm{n}}^3 \tag{5.5}$$

A laminar correlation is plotted in Fig. 5.9 as well showing the heat flux is in between the laminar regime and the fully turbulent. The laminar correlation is [18]

$$\mathrm{Nu}_x = 0.332\mathrm{Pr}^{1/3}\mathrm{Re}_x^{1/2}. \tag{5.6}$$

As is shown in Fig. 5.9, the correlations are a poor representation of the heat flux as they predict nearly double the measured heat flux at the third position. The CFD simulation is

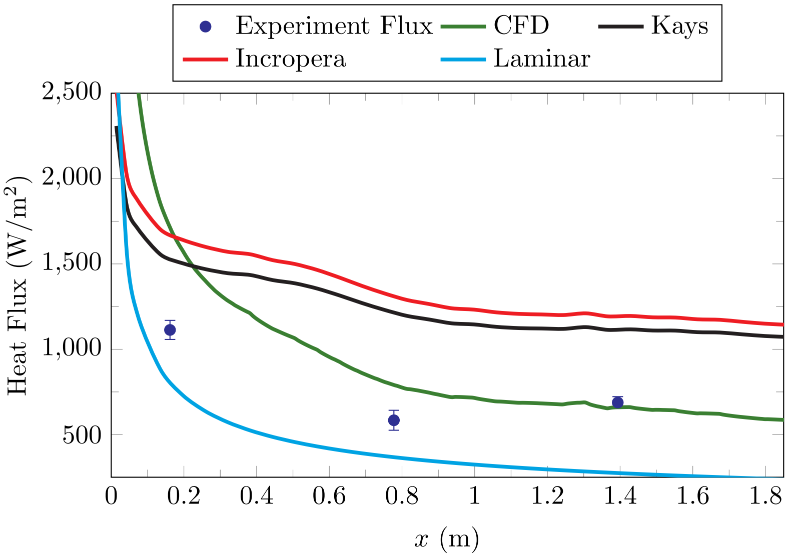

Fig. 5.9: The heat flux for the buoyancy aided isothermal mixed convection case.

closer to the measured values, but there are still large discrepancies between the experiment and the simulation. However, we reiterate that validation of the CFD model is not the scope of this dissertation. The data provide for a more robust validation study in the future. The correlations are not expected to be accurate for this flow because of the laminarization. The correlations were developed for either laminar or turublent flow. The CFD also has difficulty predicting the heat flux for this laminarizing flow, but is more accurate than the correlations.

The heat flux results and several other relevant parameters are tabulated in Table 5.4. The local Reynolds number and the ratio of buoyant forces to viscous forces is also presented. The results in Table 5.4 show that this case is in the mixed convection regime for most of the length of the plate. The fact that the first section (at least up to the first heat flux sensor) is forced convection is shown by the low ratio at the first position. This could be a contributing factor to the error in the flux computation from the CFD simulation.

Another observation from Table 5.4 is that the momentum thickness Reynolds number at the first and third positions is very near the critical momentum thickness Reynolds number specified in [18]. That means that the flow at P1 and P3 is near the transition to

Table 5.4: The buoyancy aided isothermal mixed convection heat flux results along with the Grashof to Reynolds number ratio, several boundary layer thicknesses, and the momentum thickness Reynolds number.

x Position (in)	Flux (W/m^2)	Re$_x$	Temp. (K)	Gr$_x$/Re$_x^2$	δ (mm)	δ_1 (mm)	δ_2 (mm)	Re$_{\delta_2}$
P1 = 5.87	1113	23,400	406	0.08	8.0	2.6	1.3	183
P2 = 30.12	584	113,000	414	0.39	28.1	3.2	1.7	247
P3 = 54.87	688	202,000	411	0.69	44.8	2.5	1.2	174

turbulence, with a more fully turbulent flow at P2. This further suggests that the flow is undergoing a relaminarization (although not fully laminarizing).

5.2.3 Isothermal Buoyancy Opposed Forced Convection

The boundary layer velocity SRQ's for the buoyancy opposed isothermal forced convection case are shown in Fig. 5.10. To compare the gravitational (and therefore buoyancy) effect on the boundary layer, one compares Fig. 5.10 to Fig. 5.3. As can be observed, the development of the boundary layers are different between the cases, suggesting that buoyancy forces affect the boundary layer flow for the forced convection isothermal cases. Revisiting Table 5.3, the ratio of Gr$_x$/Re$_x^2$ is near the onset of mixed convection at the third position. This means that the third position is somewhat influenced by the buoyancy forces, being nearly in the mixed convection regime. So, it is expected that the profile at the third heat flux sensor will be different depending on the orientation of gravity. Figure 5.23 shows the buoyancy aided and opposed isothermal forced convection cases plotted for comparison, and will be discussed in more detail later.

The boundary layer velocity profiles in Fig. 5.10(a) show a developing boundary layer that is not fully developed even at P3. A fully developed boundary layer profile would have a slightly lower magnitude than the P3 trend in Fig. 5.10(a), causing the boundary layer to increase in thickness. The profiles of the Reynolds normal stress in Fig. 5.10(a) also show that the boundary layer is developing. Again, the trend is due to the change in gravity direction and is discussed in Section 5.3.1. The $\overline{v}$ component of velocity is shown in

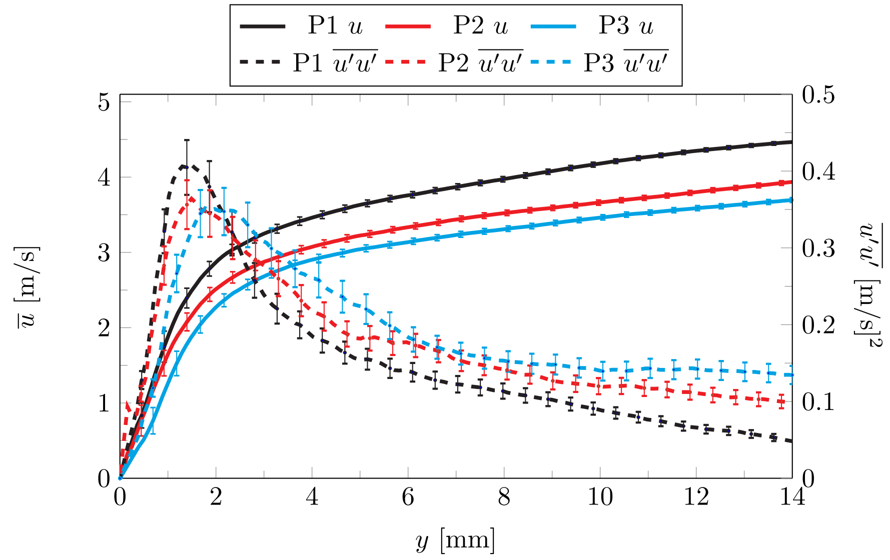

(a)

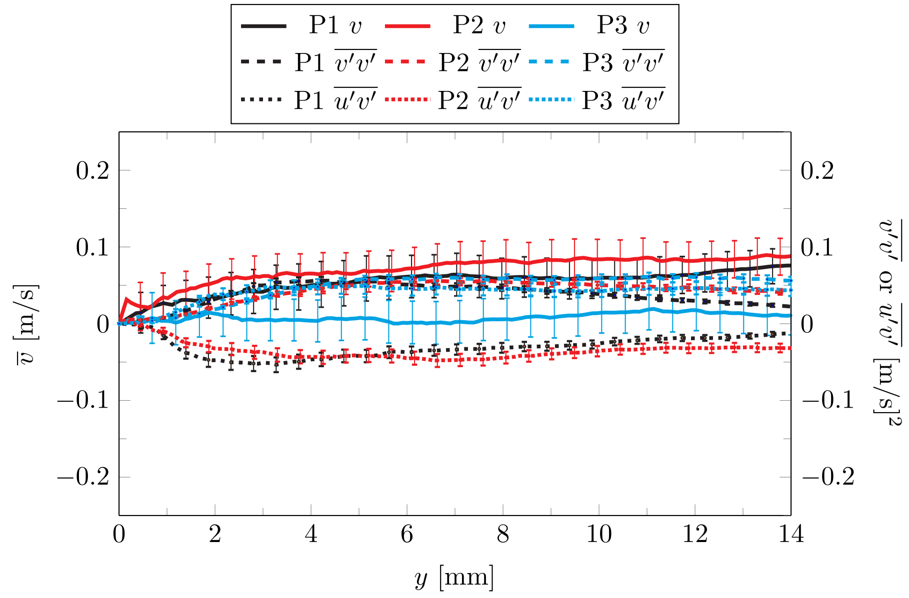

(b)

Fig. 5.10: The boundary layer velocity profiles for buoyancy opposed forced convection with isothermal heating. (a) shows the streamwise component of velocity and Reynolds normal stress. (b) shows the cross-stream component of velocity and two other measured components of the Reynolds Stress. Recall that P1 is $x = 5.87$ in., P2 is $x = 30.12$ in., and P3 is $x = 54.87$ in.

Fig. 5.10(b) and has a positive magnitude. This shows that the flow is away from the heated plate, opposite from the $\overline{v}$ component in the buoyancy aided isothermal forced convection case. Again, the values are much smaller than the streamwise component of velocity, and the uncertainty is about the same magnitude as the measurement.

The boundary layer velocity flow field for this case is compared with CFD in Fig. 5.11. The TKE is also plotted for comparison between the simulation and the experiment. The streamwise mean velocity trends of the simulation and the experiment are similar, with the simulation at the second position being nearly within the experimental uncertainty. The TKE trends show a different behavior, with the experiment and simulations being very different at the first position. The second and third positions' simulation TKE is nearly within the experimental uncertainty for the entire profile.

The friction velocity at each heat flux sensor position for this case are tabulated in Table 5.5. A linear fit of the first three vectors is used to compute the velocity gradient term in the SRQ u_τ. This linear fit also has a corresponding uncertainty shown in the table. The method to compute the friction velocity uncertainty was described in Chapter 4.3.4. The Spalding fit is also used to find the friction velocity, as shown in the table. The von Kármán constant and intercept are shown for the two different Spalding fits, where one fit uses the classical values and the other fit includes the constants in the optimization. The CFD computation of the u_τ SRQ is also tabulated in Table 5.5.

Table 5.5: The von Kármán constant, intercept, shear velocity from the Spalding fit, and the shear velocity from a linear fit near the wall at the heat flux sensor positions for the buoyancy opposed isothermal forced convection case. The resultant u_τ from the CFD simulation is also tabulated. Note that $\kappa = 0.41$ and $B = 5.0$ are classical values not included in the fit.

Position	κ	B	u_τ Spalding	u_τ Linear	u_τ CFD
P1	0.41	5.00	0.244	0.184±0.016	0.269
P1	0.39	5.17	0.237		
P2	0.41	5.00	0.220	0.176±0.015	0.236
P2	0.448	4.40	0.240		
P3	0.41	5.00	0.210	0.137±0.017	0.233
P3	0.499	6.16	0.221		

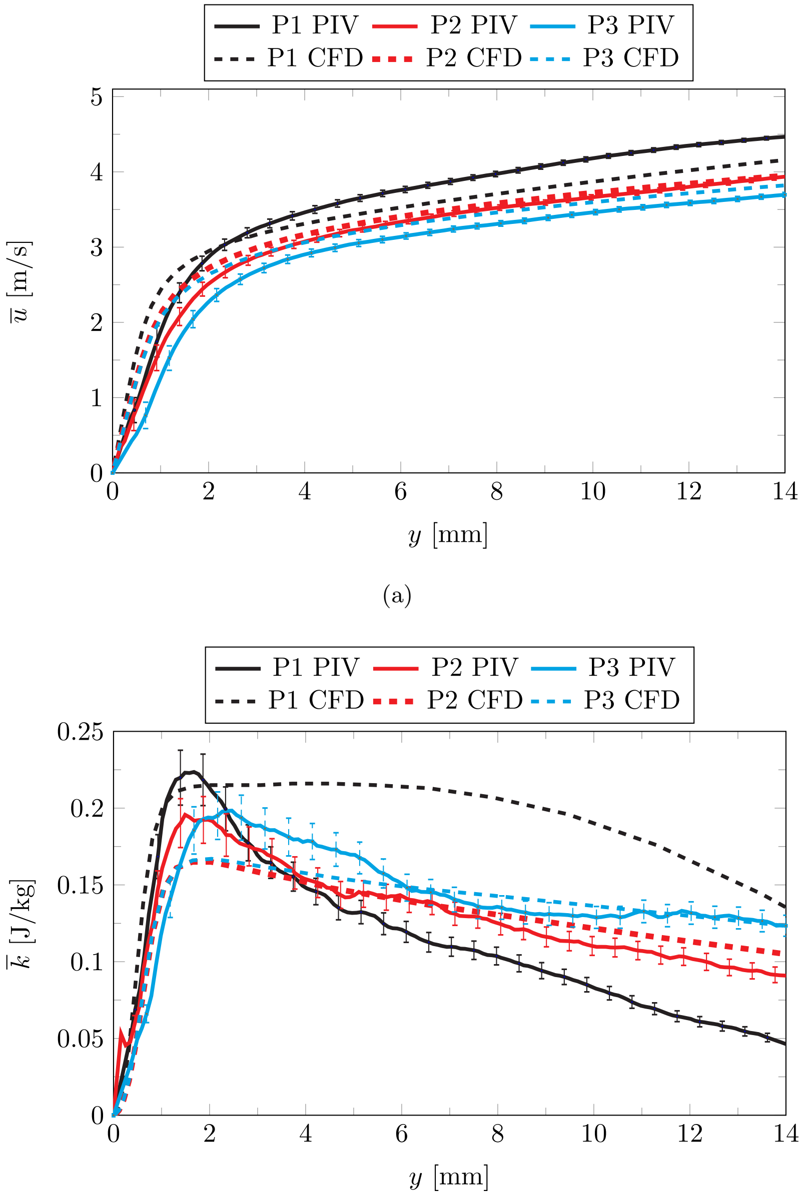

(a)

(b)

Fig. 5.11: The boundary layer velocity profiles for buoyancy opposed forced convection with isothermal heating compared with CFD results using the same boundary conditions. (a) shows the streamwise component of velocity. (b) shows the turbulence kinetic energy.

Table 5.5 shows that the friction velocity magnitude is smaller than the friction velocity for the buoyancy aided isothermal convection case, shown in Table 5.2. This is due to the smaller near wall velocity gradient in the buoyancy opposed case. This suggests that buoyancy has a slight contribution to the boundary layer flow, even in forced convection. The difference in boundary layer development is also observed in Figs. 5.3 and 5.10. The linear method underpredicts the other methods for the computation of the shear velocity. This is likely because the data do not resolve the viscous sublayer as much as the buoyancy aided case. Only three to four velocity vectors could be considered within the viscous sublayer. As the data are so close to the transition layer, the linearity of the data must be questioned.

The heat flux SRQ is shown in Fig. 5.12. The measurements are compared with the Kays correlation from Eqn. 5.1 and the Incropera correlations from Eqn. 5.2. The similarity between this case and buoyancy aided isothermal case is obvious when comparing with Fig. 5.6. However, the simulation predicts a higher heat flux trend during the first 0.25 m. of the test section comparing Figs. 5.6 and 5.12.

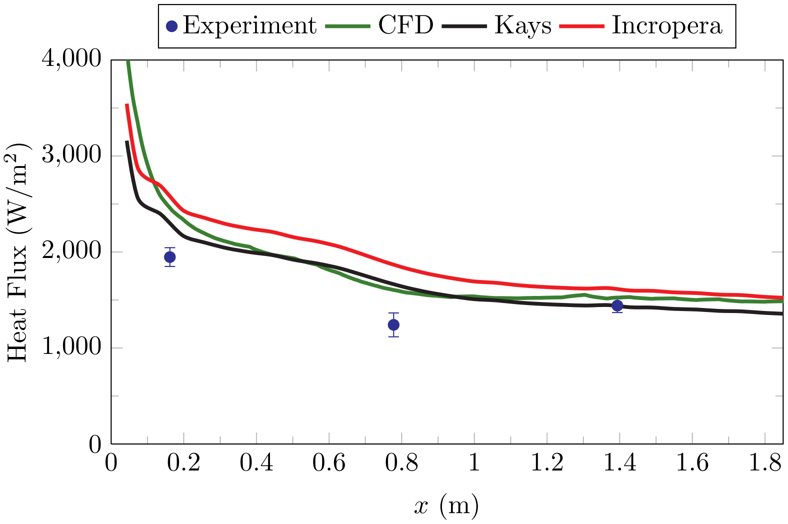

Fig. 5.12: The measured heat flux for the buoyancy opposed isothermal forced convection case is compared with the two correlations previously presented and the corresponding CFD simulation for this case.

The correlations and the CFD simulation are also closer together in the resultant heat flux SRQ than the buoyancy aided case. The difference between the correlations and the simulation is not as consistent through x as the buoyancy aided case. The simulation is further from the experimental measurements for this buoyancy opposed case.

The heat flux and several relevant boundary layer and dimensionless parameters are tabulated in Table 5.6. The convection ratio $\mathrm{Gr}_x/\mathrm{Re}_x^2$ shows that this case is in the forced convection regime at the three positions. The momentum thickness Reynolds number at all three positions is higher than the critical momentum thickness Reynolds number. This means that this case can be considered turbulent flow throughout, but it is noted that the flow is developing along the length of the plate. This is shown by (among other quantities) the momentum thickness Reynolds number increasing at each x position.

Table 5.6: The buoyancy opposed isothermal forced convection heat flux results along with the Grashof to Reynolds number ratio and the momentum thickness Reynolds number.

x Position (in)	Flux (W/m^2)	Re_x	Temp. (K)	$\mathrm{Gr}_x/\mathrm{Re}_x^2$	δ (mm)	δ_1 (mm)	δ_2 (mm)	Re_{δ_2}
P1 = 5.87	1947	41,400	360	0.02	7.1	3	1.8	466
P2 = 30.12	1241	199,000	386	0.12	25.1	5.9	2.8	713
P3 = 54.87	1442	357,000	391	0.22	40.0	7.3	3.2	813

5.2.4 Isothermal Buoyancy Opposed Mixed Convection

The velocity SRQ's for the buoyancy opposed isothermal mixed convection case are shown in Fig. 5.13. A comparison of these data with those shown in Fig. 5.7 reveals the significant difference in the boundary layers when the direction of gravity is the only change. This discussion is deferred to Section 5.3.1.

The velocity profiles presented in Fig. 5.13(a) show the streamwise component of the velocity at the three heat flux sensor positions. The flow is affected by gravity (as expected) and shows drastically different boundary layers at the first position when compared with the second and third positions. The free stream velocity can be seen at the first position, but not at P2 nor P3. The $\overline{v}$ component of the velocity in Fig. 5.13(b) shows a positive (away from the plate) velocity, just as the buoyancy opposed forced convection case but unlike the buoyancy aided isothermal mixed convection case. The other two measured quantities of the Reynolds stress are small.

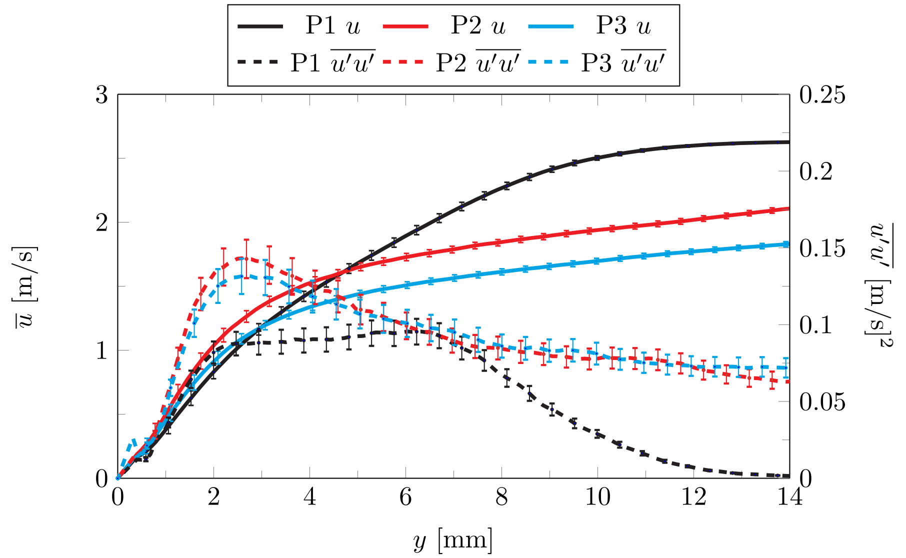

(a)

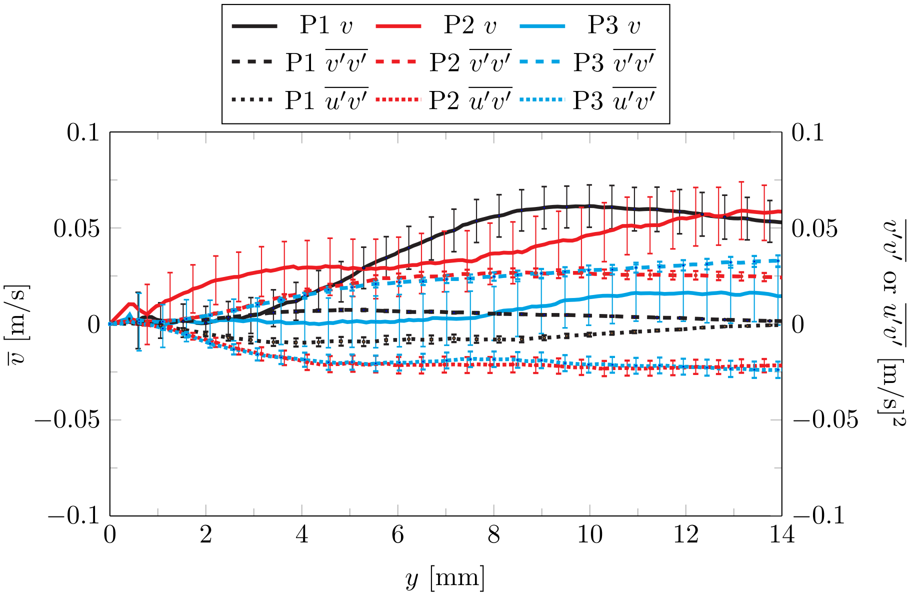

(b)

Fig. 5.13: The boundary layer velocity profiles for buoyancy opposed mixed convection with isothermal heating. (a) shows the streamwise component of velocity and Reynolds normal stress. (b) shows the cross-stream component of velocity and two other measured components of the Reynolds Stress.

Figure 5.14 shows the boundary layer velocity profiles and TKE compared with the corresponding CFD simulation for this case. The CFD simulation predicts the streamwise component of velocity reasonably well near the free-stream. Near the wall and at the other two streamwise positions, the streamwise velocity is not as well predicted. The CFD simulation boundary layer velocity profiles are not contained within the measurement uncertainty. It is interesting that the CFD simulation for this case predicts the same viscous sublayer velocity profile for all three positions. The TKE presented in Fig. 5.14(b) shows that for the first position and near the wall, the CFD simulation under-predicts $\overline{k}$ by nearly 50%. The simulation matches the experiment further away from the wall near the free-stream. The CFD simulation TKE is nearly within the experimental uncertainty for the other two positions.

The heat flux from the plate at the three heat flux sensor positions is plotted in Fig. 5.15. The CFD resultant heat flux and two correlations are also presented in Fig. 5.15. Comparing the heat flux presented in Fig. 5.9 and that in Fig. 5.15, we see that buoyancy effects on the heat flux, correlations, and CFD simulation are not negligible. It is interesting that the correlations are not consistently higher than the experiment for this case (as it was in the isothermal aided mixed convection case).

The heat flux, dimensionless numbers, and relevant boundary layer parameters are tabulated in Table 5.7. The convection ratio shows that most of the plate can be considered as mixed convection. The momentum thickness Reynolds numbers show that the flow is in the turbulent regime, and still developing.

Table 5.7: The buoyancy opposed isothermal mixed convection heat flux results along with the Grashof to Reynolds number ratio and the momentum thickness Reynolds number.

x Position (in)	Flux (W/m^2)	Re$_x$	Temp. (K)	Gr$_x$/Re$_x^2$	δ (mm)	δ_1 (mm)	δ_2 (mm)	Re$_{\delta_2}$
P1 = 5.87	1180	23,700	366	0.08	7.14	4.2	1.7	248
P2 = 30.12	932	114,000	390	0.38	25.1	5.9	3.1	459
P3 = 54.87	1055	204,000	395	0.67	44.7	7.3	3.7	535

5.2.5 Constant Heat Flux Buoyancy Aided Forced Convection

The measured boundary layer velocities at the three heat flux sensor positions for the

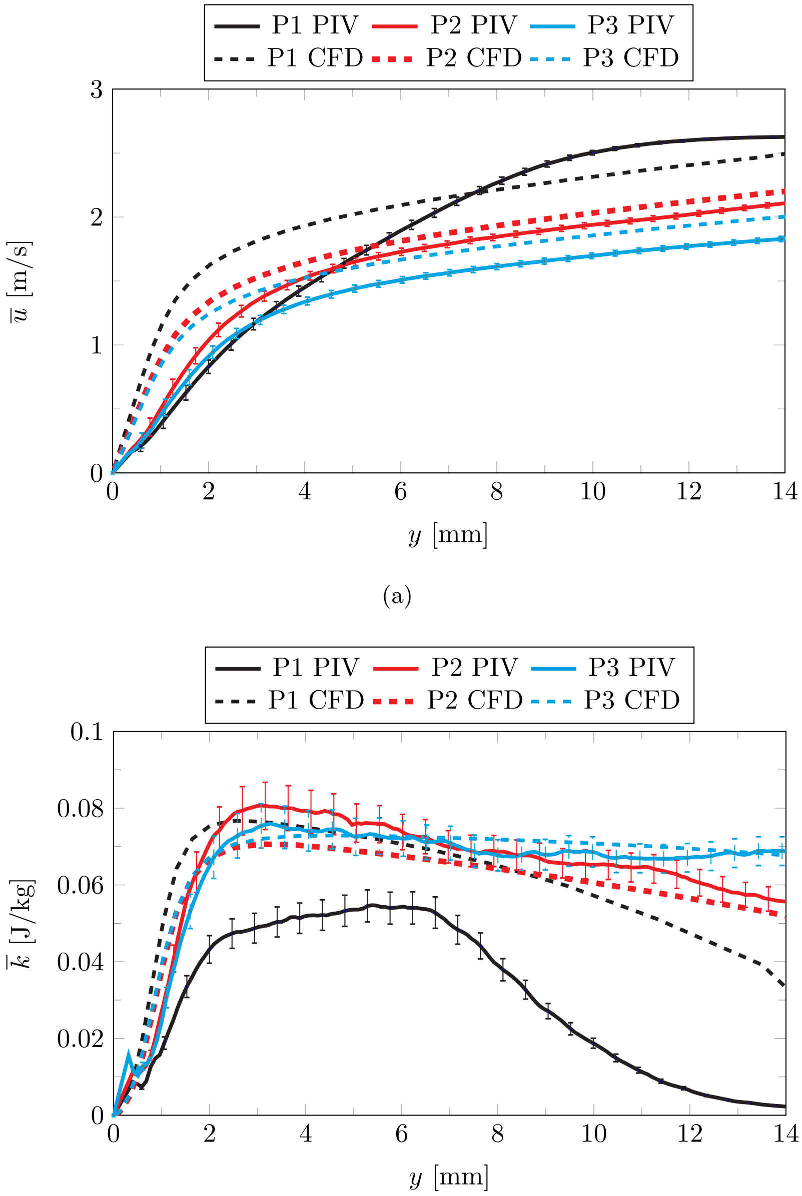

(a)

(b)

Fig. 5.14: The boundary layer velocity profiles for buoyancy opposed mixed convection with isothermal heating compared with CFD results using the same boundary conditions. (a) shows the streamwise component of velocity. (b) shows the turbulence kinetic energy profiles.

buoyancy aided constant heat flux forced convection case are shown in Fig. 5.16. These profiles are compared to those in the buoyancy aided isothermal forced convection case

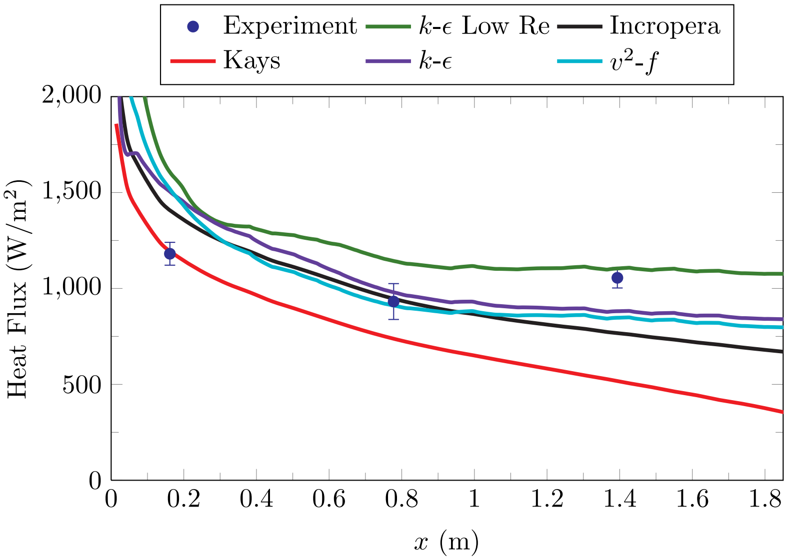

Fig. 5.15: The heat flux for the buoyancy opposed isothermal mixed convection case compared with several CFD models with the k-ϵ Low Re being the standard model for the mixed cases in this study.

shown in Fig. 5.3 and it is observed that the trends are practically the same. The change in plate temperature appears to have no influence on the profiles. A more thorough comparison is included in Fig. 5.28 and is discussed in detail in Section 5.3.1.

The streamwise boundary layer velocity profiles presented in Fig. 5.16 are plotted with the CFD results for the same boundary conditions in Fig. 5.17(a) and the TKE comparison is plotted in Fig. 5.17(b). The first position velocity and TKE are poorly predicted using this CFD model. The CFD simulation streamwise velocity boundary layer at the second and third positions are somewhat similar. The TKE near the wall is poorly predicted by the CFD at all positions. This is an example of using several SRQ's in the difficulty spectrum of Fig. 1.3. A model may predict a quantity (such as the streamwise velocity) reasonably well, but fails to predict another quantity (such as the turbulence kinetic energy and heat flux). Also, the TKE may be computed in the simulation accurately for the free-stream, but not near the wall.

The friction velocity SRQ for the buoyancy aided constant heat flux forced convection case is shown in Table 5.8. The shear velocity u_τ is comparable to the isothermal heating

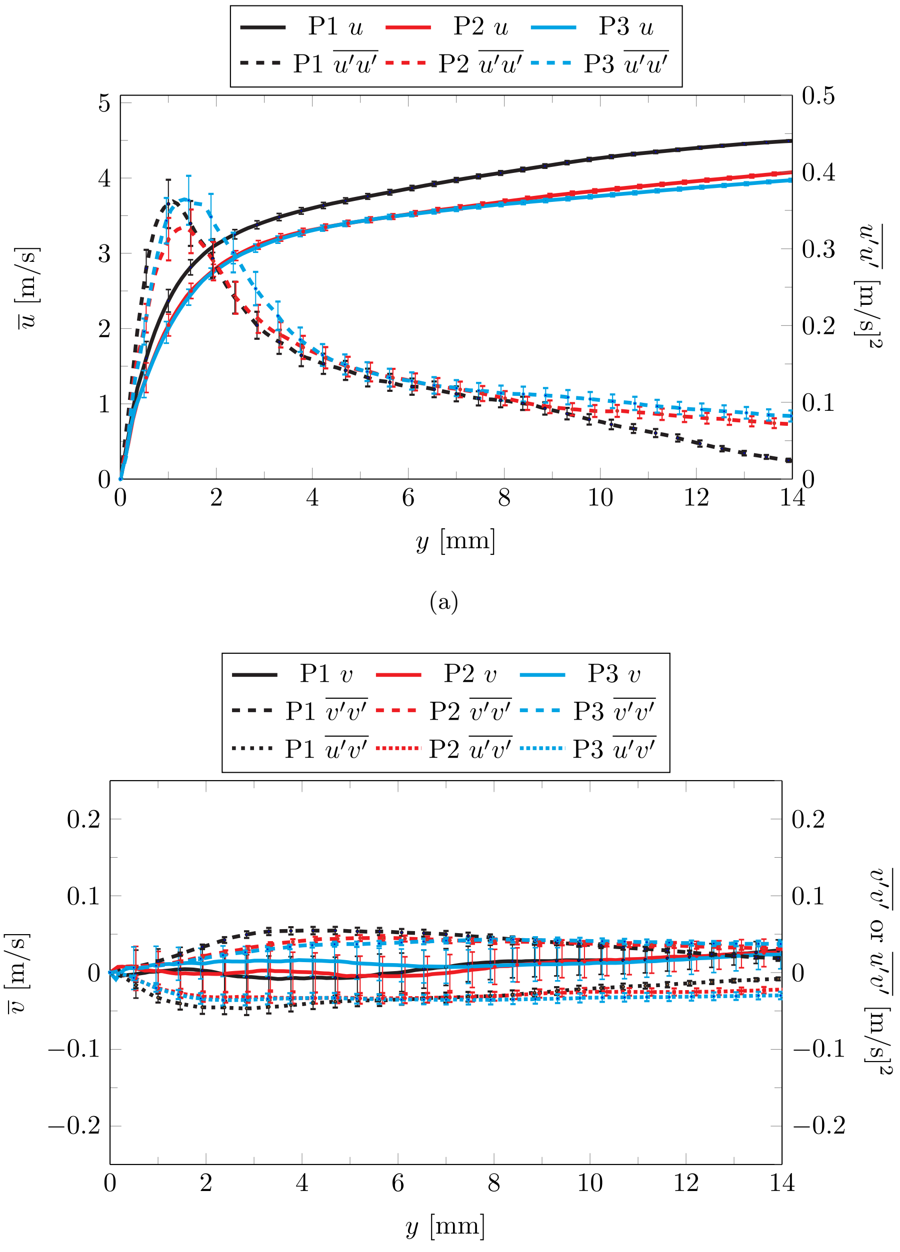

(a)

(b)

Fig. 5.16: The boundary layer velocity profiles for buoyancy aided forced convection with constant heat flux from the plate. (a) shows the streamwise component of velocity and Reynolds normal stress. (b) shows the cross-stream component of velocity and two other measured components of the Reynolds stress.

case for buoyancy aided forced convection, shown in Table 5.2. It is worth noting that the shear velocity resulting from the Spalding fit is much more consistent between these

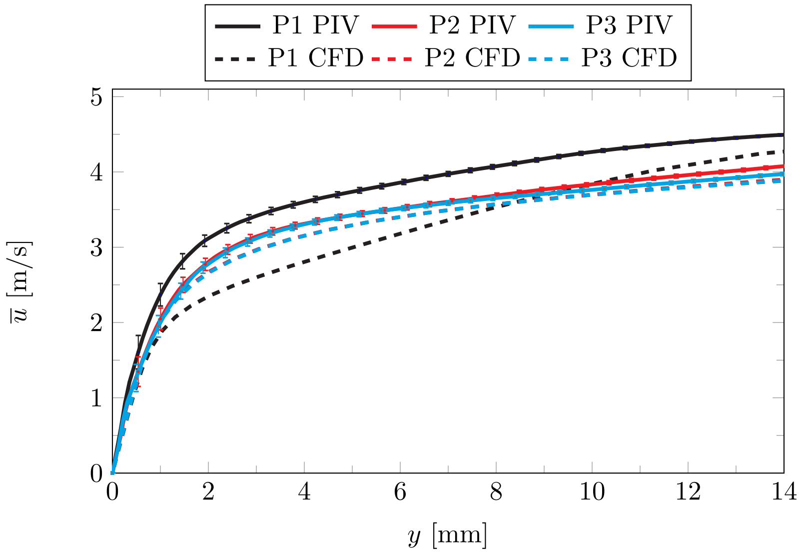

(a)

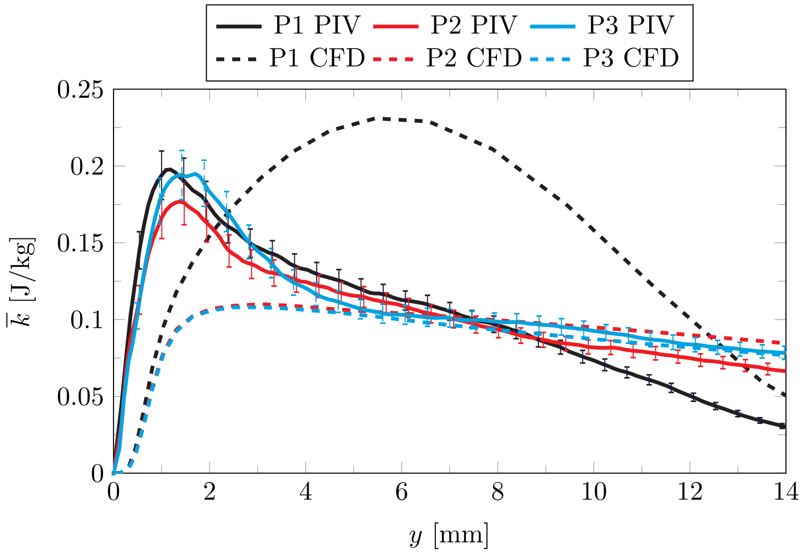

(b)

Fig. 5.17: The boundary layer velocity profiles for buoyancy aided forced convection with constant heat flux compared with CFD results using the same boundary conditions. (a) shows the streamwise component of velocity. (b) shows the turbulence kinetic energy profiles.

cases than u_τ resulting from the linear fit near the wall. Since the buoyancy aided forced convection cases have practically the same flow field (the plate temperature has little effect on the flow), the shear velocities should be nearly identical when comparing the isothermal and constant flux cases.

Table 5.8: The von Kármán constant, intercept, shear velocity from the Spalding fit, and the shear velocity from a linear fit near the wall at the heat flux sensor positions for the buoyancy aided constant heat flux forced convection case.

Position	κ	B	u_τ Spalding	u_τ Linear	u_τ CFD
P1	0.41	5.00	0.248	0.248±0.011	0.200
P1	0.45	4.92	0.262		
P2	0.41	5.00	0.233	0.230±0.012	0.203
P2	0.46	8.16	0.210		
P3	0.41	5.00	0.232	0.240±0.015	0.206
P3	0.41	7.37	0.206		

The wall coordinate velocity profiles using the optimized von Kármán constant and intercept are shown in Fig. 5.18. This case shows a slight acceleration at the third position. This suggests that buoyancy effects are not completely insignificant even at this Reynolds number. However, the fit at the second position and discussion in Section 5.3.1 suggests that the fit method is not reliable enough to presume that the trend shows an acceleration or deceleration of the flow.

The measured heat flux for the buoyancy aided constant heat flux forced convection case is shown in Fig. 5.19. This can be compared with Fig. 5.6 as the only difference between the two data sets is the plate temperature. The CFD resultant SRQ heat flux is also plotted with the experimental measurements, showing a drastic difference between the two. Again, the importance of using several SRQ's in the difficulty spectrum is emphasized. The computed boundary layer velocity might be within the validation error limits, but derivative or integral quantities could be far from within the allowable limits. The correlation for the Incropera trend is given in Eqn. 5.7, showing only a slight difference from the isothermal correlation given in Eqn. 5.2.

$$\mathrm{Nu_x} = 0.0308\mathrm{Re}_x^{4/5}\mathrm{Pr}^{1/3} \tag{5.7}$$

The measured heat flux is tabulated in Table 5.9, along with the local Reynolds number,

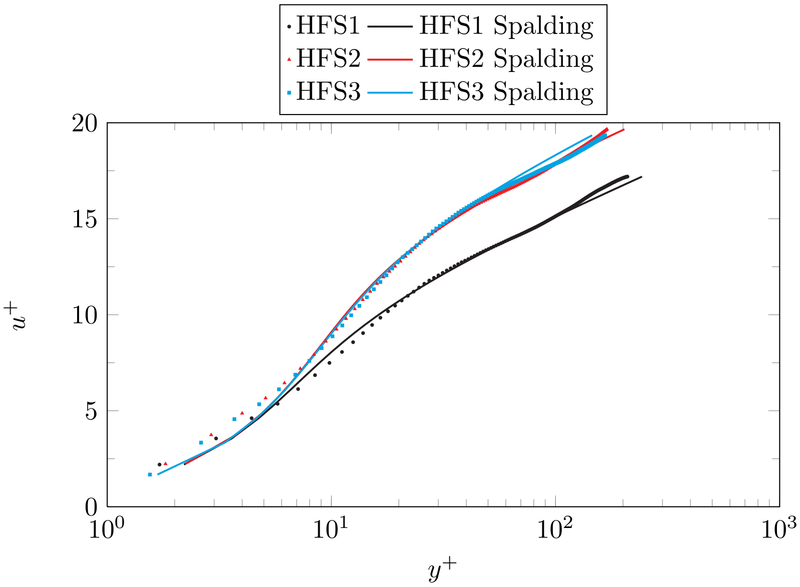

Fig. 5.18: The wall coordinate boundary layers for the three heat flux sensor positions for buoyancy aided constant flux forced convection flow and the Spalding fit profiles for comparison.

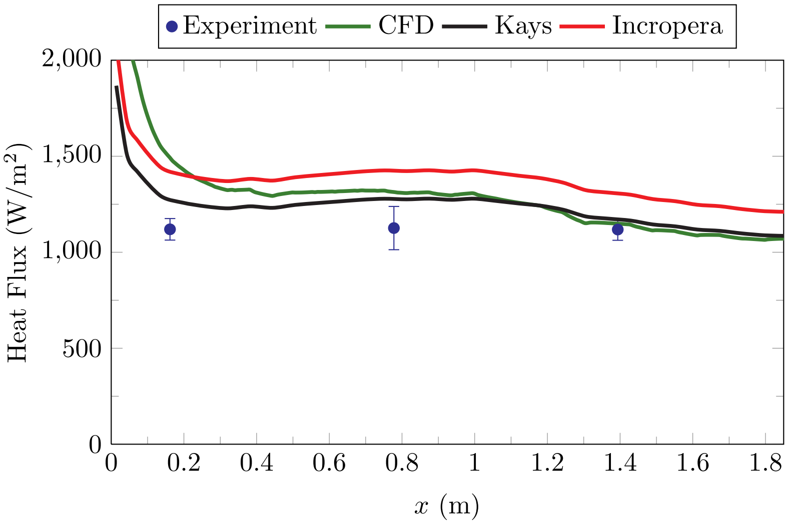

Fig. 5.19: The heat flux for the buoyancy aided constant heat flux forced convection case compared with the CFD results for the same boundary conditions.

surface temperature, the ratio of the Grashof number to the Reynolds number squared, and the momentum thickness Reynolds number. The ratio $\mathrm{Gr}_x/\mathrm{Re}_x^2$ in Table 5.9 shows that this case is also in the forced convection regime, but that the buoyancy forces become somewhat significant at the third heat flux sensor position. Table 5.9 also shows that the flow is turbulent and developing along x.

Table 5.9: The buoyancy aided constant heat flux forced convection heat flux results along with the Grashof to Reynolds number ratio and the momentum thickness Reynolds number.

x Position (in)	Flux (W/m^2)	Re$_x$	Temp. (K)	Gr$_x$/Re$_x^2$	δ (mm)	δ_1 (mm)	δ_2 (mm)	Re$_{\delta_2}$
P1 = 5.87	1119	40,200	404	0.015	7.18	2.3	1.4	357
P2 = 30.12	1126	193,000	413	0.104	25.2	3.6	2.3	574
P3 = 54.87	1118	346,000	410	0.193	40.2	3.6	2.3	582

5.2.6 Constant Heat Flux Buoyancy Aided Mixed Convection

The measured boundary layers at the three heat flux positions for the buoyancy aided constant flux mixed convection case are shown in Fig. 5.20. These profiles are compared to those in Fig. 5.7 in Section 5.3.1. The streamwise velocity profile at the first position clearly captures the free-stream velocity and near zero Reynolds normal stress. The second and third positions are nearly the same, but shows a slight relaminarization trend at the third position. The $\overline{v}$ component of velocity is negative for this case (flow toward the plate), and the two other measured components of the Reynolds stress are nearly zero.

It is observed that the velocity profiles develop differently than the isothermal case. This is due to the different heating conditions. The isothermal case has a higher plate temperature than the constant flux case (see Fig. 5.1). This higher temperature in the isothermal case drives an elevated heat flux when compared to the constant flux case. The increased flux to the flow increases the buoyancy effects and changes the velocity profile and development. This fact also suggests that the constant flux case does not laminarize as much as the isothermal case.

The comparison with the simulations for the constant heat flux buoyancy aided mixed convection case is shown in Fig. 5.21, with the streamwise velocity profiles shown in Fig. 5.21(a) and the TKE shown in Fig. 5.21(b). The models employed fail to predict most aspects of

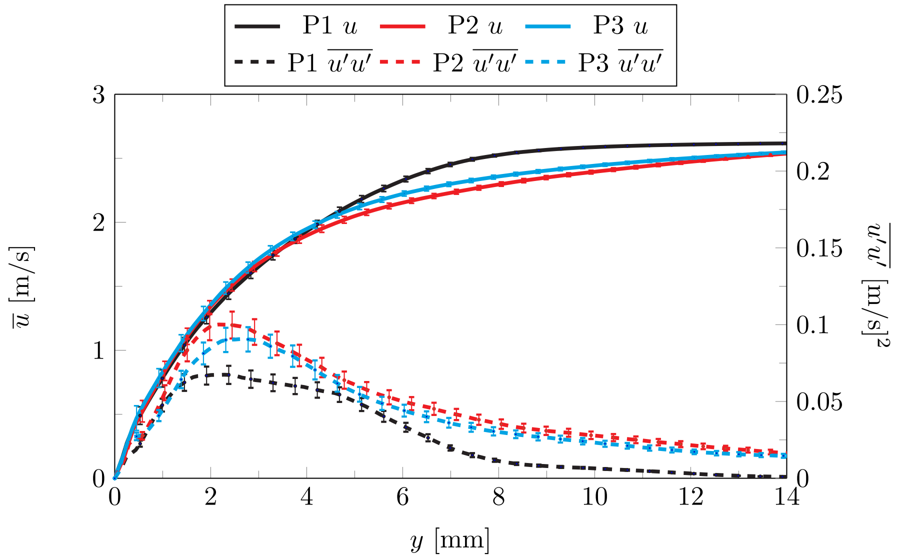

(a)

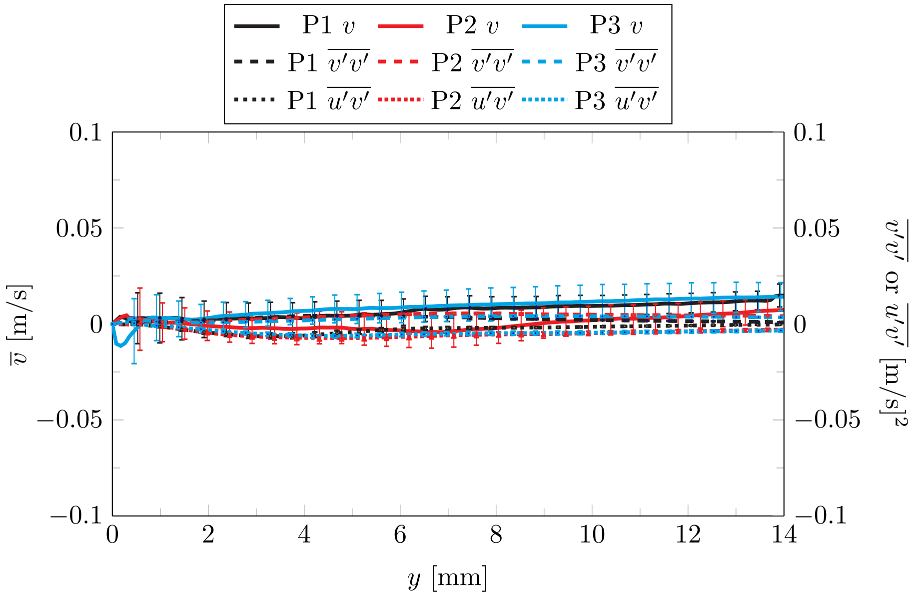

(b)

Fig. 5.20: The boundary layer velocity profiles for buoyancy aided mixed convection with constant flux heating. (a) shows the streamwise component of velocity and Reynolds Stress. (b) shows the cross-stream component of velocity and two other measured components of the Reynolds Stress.

this flow. The velocity profiles have significant differences and the TKE also has large error. The models are similar to those shown in Fig. 5.8 and have similar issues in predicting the experimentally measured SRQ's. The first position CFD simulation is particularly different from the measured quantities.

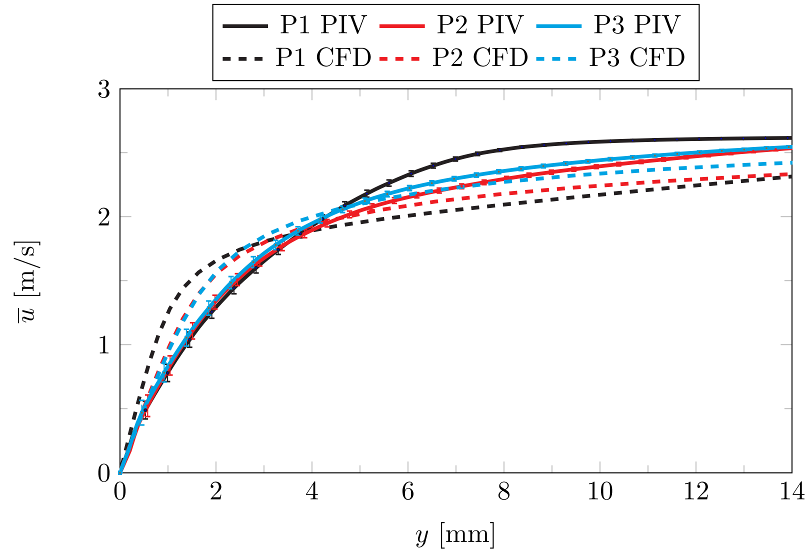

(a)

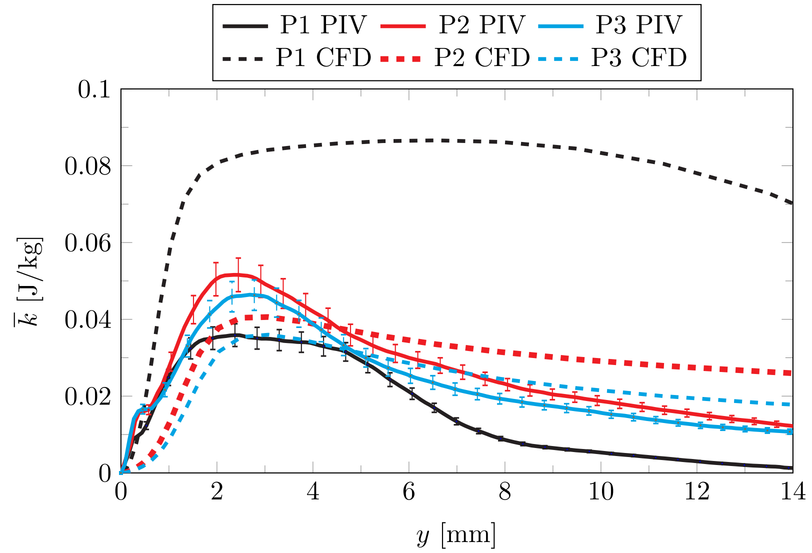

(b)

Fig. 5.21: The boundary layer velocity profiles for buoyancy aided mixed convection with constant heat flux heating compared with CFD results using the same boundary conditions. (a) shows the streamwise component of velocity. (b) shows the turbulence kinetic energy.

The measured heat flux for the buoyancy aided constant heat flux mixed convection case is shown in Fig. 5.22. This can be compared with the measured flux in of the isothermal buoyancy aided mixed case from Fig. 5.9, as the only difference between the measurements in the plate temperature. This temperature difference is shown in Fig. 5.1. The measured heat flux is also compared with the CFD computed SRQ of heat flux along the $z = 0$ centerline. The simulation trend is similar to the isothermal case, but the constant flux case has a steeper gradient. The experiment and the simulation are in near agreement at the third position.

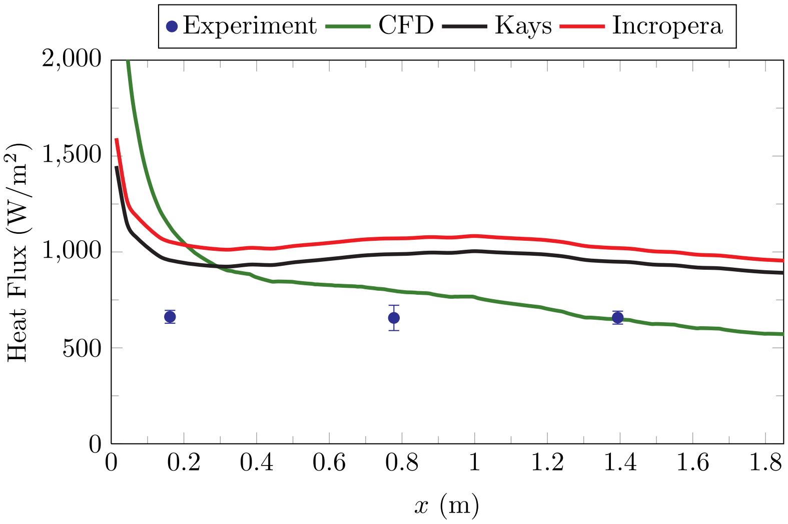

Fig. 5.22: The heat flux for the buoyancy aided constant heat flux mixed convection case.

The measured heat flux is tabulated in Table 5.10 along with the local Reynolds number, the convection ratio, the momentum thickness, and the momentum thickness Reynolds number. The ratio $\mathrm{Gr}_x/\mathrm{Re}_x^2$ shows that after the second heat flux sensor position, the flow is in the mixed convection regime. The leading section of the plate including the first heat flux sensor is considered to be in the forced convection regime. Table 5.10 also shows that the first position is near the critical momentum thickness Reynolds number, suggesting a transition near that point to turbulent flow. The third position momentum thickness Reynolds number is lower than the second position, suggesting a relmainarization of the flow.

Table 5.10: The buoyancy aided constant heat flux mixed convection heat flux results along with the Grashof to Reynolds number ratio and the momentum thickness Reynolds number.

x Position (in)	Flux (W/m^2)	Re$_x$	Temp. (K)	Gr$_x$/Re$_x^2$	δ (mm)	δ_1 (mm)	δ_2 (mm)	Re$_{\delta_2}$
P1 = 5.87	662	23,600	407	0.049	8.0	2.4	1.2	181
P2 = 30.12	656	113,000	413	0.315	28.1	3.2	1.8	268
P3 = 54.87	658	203,000	410	0.560	44.8	3.1	1.6	233

5.3 Discussion of SRQ's

The system response quantities presented above are compared and discussed in more detail in this section. Several comparisons are made between the buoyancy aided and buoyancy opposed cases, and the isothermal and constant heat flux cases. Classical boundary layer theory is also presented and compared with some of the boundary layer velocity profiles previously presented.

5.3.1 Gravity and Temperature Effects

Figure 5.23 shows the boundary layer velocity profiles for the buoyancy aided and opposed isothermal forced convection. Figure 5.23 shows that not only is the flow at position 3 affected by gravity (as previously stated), but also at position 2. The difference between the aided and opposed cases at the second position is smaller than the difference between the cases at the third position, suggesting that the effects of gravity affect the development of the boundary layer in forced convection. The difference at the first position is the smallest, as shown in Fig. 5.23.

The relative difference for the isothermal forced convection is also shown in Fig. 5.23, with the difference being attributed to the effects of the change in the direction of gravity. The relative difference in this forced convection case due to a gravity change is denoted $\Delta\overline{u}_{F,G}$. The relative difference was computed by taking the difference between the buoyancy aided and opposed and dividing by the buoyancy opposed velocities.

The effects of gravity direction on measured heat flux for isothermal forced and mixed convection is presented with Fig. 5.24. The measured heat flux for the forced convection

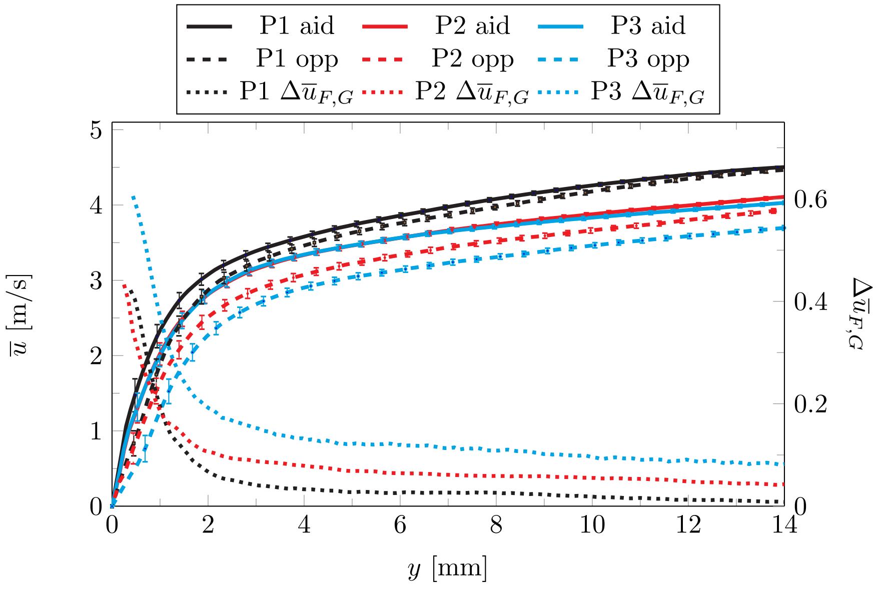

Fig. 5.23: The boundary layer velocity comparison for the isothermal forced convection buoyancy aided and opposed cases. The relative difference between the cases is also plotted as $\Delta\overline{u}_{F,G}$.

cases are similar. The buoyancy opposed forced convection case shows a slightly elevated heat flux compared to the buoyancy aided forced convection at the second and third positions. The heat flux at the first position for the forced convection is practically the same. The heat flux measured at the first position for the mixed cases is also nearly the same. The mixed convection buoyancy opposed case has much higher heat flux then the buoyancy aided case at the second two positions.

The convection ratio $\mathrm{Gr}_x/\mathrm{Re}_x^2$ for the isothermal cases is shown in Fig. 5.25. Both cases show that the convection ratio is not influenced by the change in gravity. This is not surprising because the free-stream air temperature and the wall temperature between all of the cases are the same. This makes the properties and other terms in the computation the same.

The effects of the direction of gravity on the momentum thickness is shown in Fig. 5.26. For both forced and mixed convection, the momentum thickness at the first position is not significantly affected by the direction of gravity. The buoyancy opposed cases show an

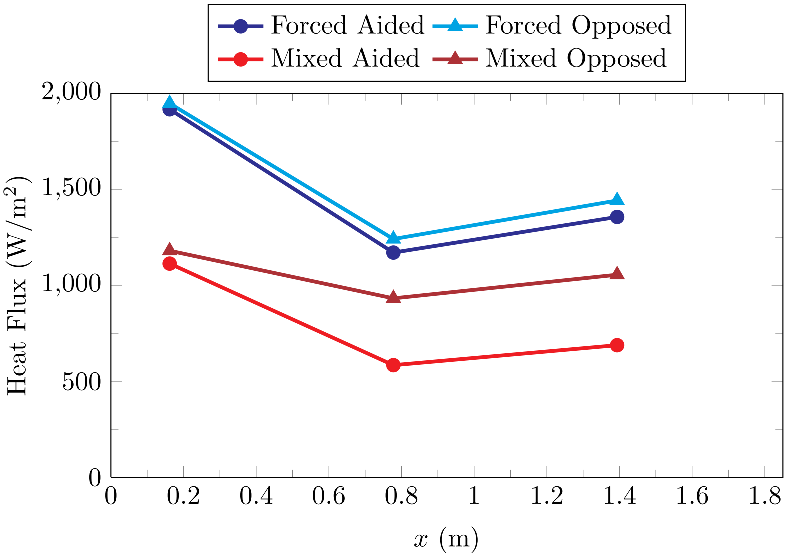

Fig. 5.24: The heat flux comparison for isothermal forced and mixed convection comparing the buoyancy aided and buoyancy opposed conditions.

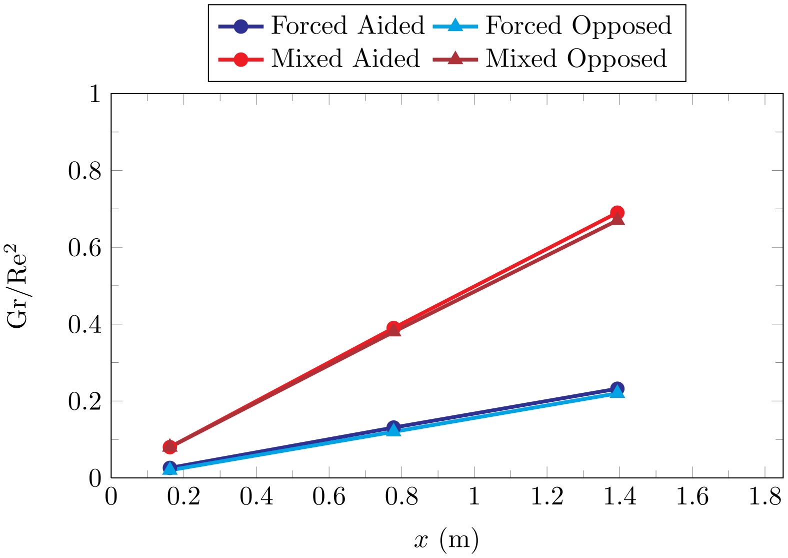

Fig. 5.25: The convection ratio comparison for isothermal forced and mixed convection comparing the buoyancy aided and buoyancy opposed conditions.

increase in the momentum thickness as a function of x. The buoyancy aided cases show a constant momentum thickness (forced) or a decrease in the momentum thickness (mixed) from the second to third positions.

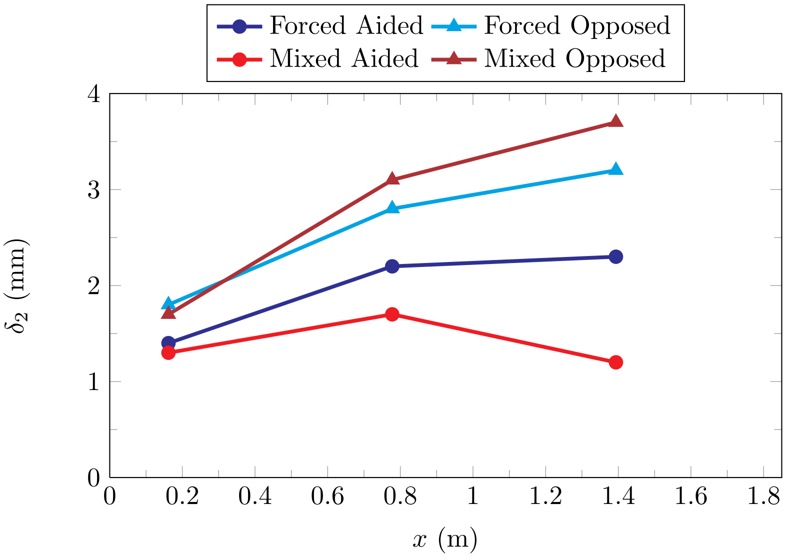

Fig. 5.26: The momentum thickness comparison for isothermal forced and mixed convection comparing the buoyancy aided and buoyancy opposed conditions.

Figure 5.27 shows the comparison of the boundary layer velocity profiles between the buoyancy aided and opposed isothermal mixed convection cases. As expected, the trends are significantly different. The aided case shows the laminarization (as discussed previously). The opposed case shows a developing boundary layer that appears to never fully develop. Even the first position boundary layers are different between the two cases. The mixed convection flow is influenced strongly by gravity. It is also interesting that the measured free stream at the first position for both cases is the same. This is shown by the near zero relative difference in Fig. 5.27.

The boundary layer velocities plotted in Figs. 5.3 and 5.16 are plotted for comparison in Fig. 5.28 to compare the effects of isothermal and constant flux heating for buoyancy aided forced convection. The slight change in heating conditions has little effect on the boundary layer velocity flow for buoyancy aided forced convection. The trends in Fig. 5.28 are nearly indistinguishable. This is shown by computing the relative difference between the data, plotted as $\Delta\overline{u}_{F,T}$. The magnitude of the difference is much smaller than that presented in Fig. 5.23. As previously stated, the forced convection flow is influenced by

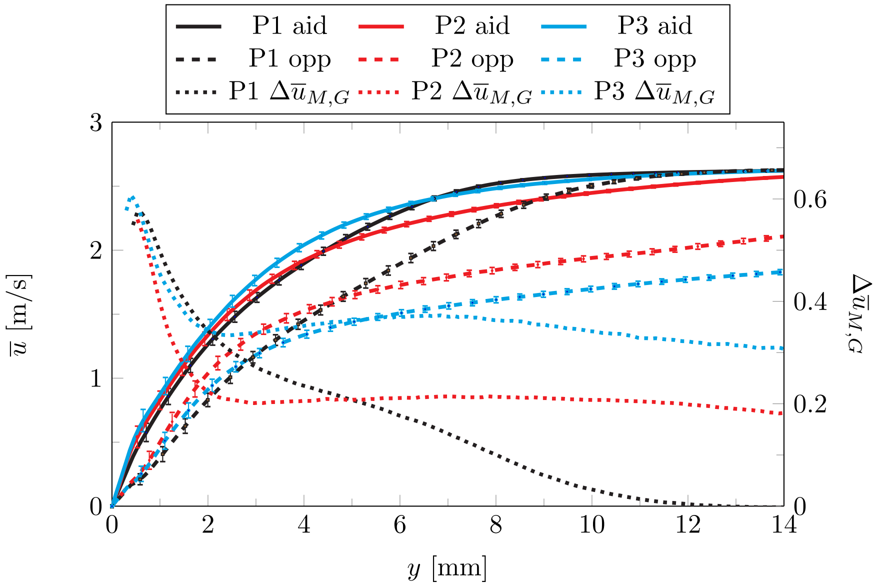

Fig. 5.27: The boundary layer velocity profile comparison for the isothermal mixed convection buoyancy aided and opposed cases. The relative difference due to gravity effects for isothermal mixed convection is denoted $\Delta\overline{u}_{M,G}$.

buoyancy, shown in Fig. 5.23. However, the change in buoyant forces due to the change in heating conditions does not significantly influence the boundary layer velocity profiles. The effects due to gravity changes are much more significant.

Figure 5.29 shows the boundary layer velocity for the buoyancy aided mixed convection cases comparing the constant heat flux and isothermal heating effects on the boundary layer velocity. The third position is influenced most heavily by the change in heating conditions. The first position is not influenced significantly. The second position shows some difference due to the different heating. As with the forced convection case mentioned above, the effects due to gravity changes are more significant than the changes resulting from the plate temperature. Although this is only for the plate temperatures outlined in Fig. 5.1.

The data presented in Figs. 5.23, 5.27, 5.28, and 5.29 show that the boundary layer velocities are more significantly effected by gravity than by the wall temperature, all other boundary conditions being practically the same. The mixed convection cases are more significantly effected by the change in buoyant forces than the forced convection cases (as

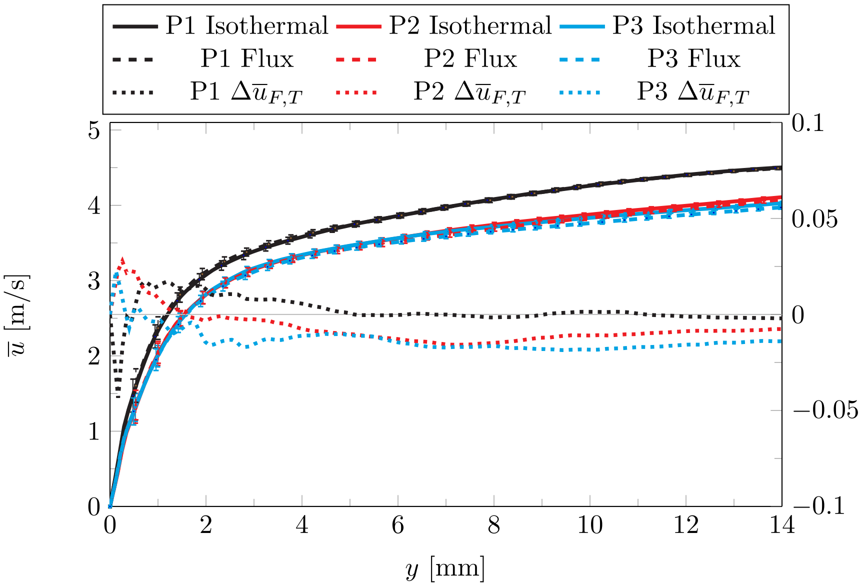

Fig. 5.28: The boundary layer velocity comparison for the forced convection buoyancy aided cases, comparing the isothermal and constant flux heating conditions. The relative difference between the cases is denoted $\Delta\overline{u}_{F,T}$.

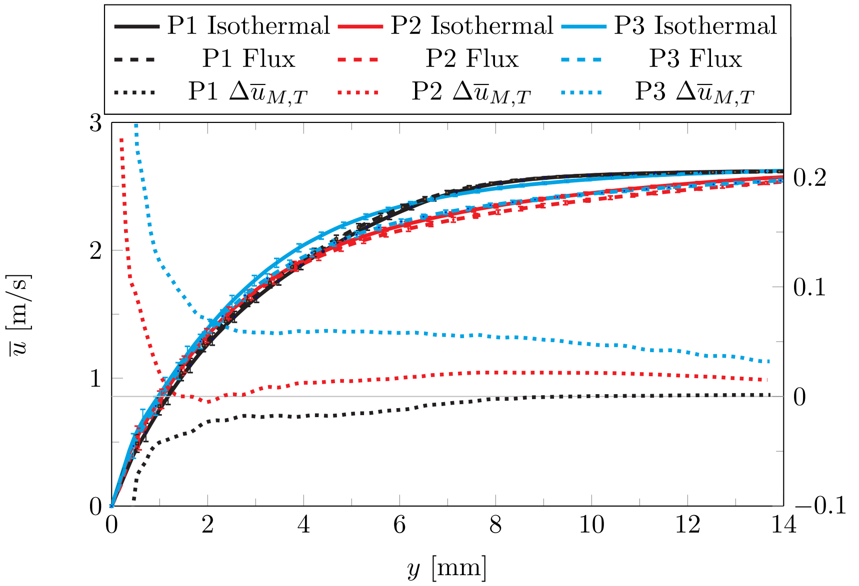

Fig. 5.29: The boundary layer velocity comparison for the mixed convection buoyancy aided cases comparing the isothermal and constant heat flux conditions. The relative difference between the cases is denoted $\Delta\overline{u}_{M,T}$.

expected). The forced convection cases do show some influence from buoyancy on the boundary layer velocity profiles.

5.3.2 Comparison of Classical Boundary Layer Shape Factors

The classic literature provides some insight into what one can expect in the measured boundary layer velocity. The shape factor H, which is the ratio of the displacement thickness and the momentum thickness, is plotted in Fig. 5.30. The displacement thickness δ_1 and the momentum thickness δ_2 where presented earlier. The shape factor is plotted as a function of a second shape factor, η, which is defined as [55]

$$\eta = 1 - \left(\frac{u(H)}{\overline{u}_{\infty}} \right)^2 . \tag{5.8}$$

The $u(H)$ term in Eqn. 5.8 is the measured velocity at a distance H from the wall. The expected trend is for η as a function of H is [55]

$$\eta = 1 - \left[\frac{H-1}{H(H+1)} \right]^{H-1} . \tag{5.9}$$

It is noted that for $\eta > 0.46$ a pressure rise exists in the flow, which is also called an adverse pressure gradient [55]. From Fig. 5.30, we see that all of the buoyancy aided cases are in the adverse pressure range. The experimental measurements also match trends shown in the data presented by Schlichting and others (see Fig. 22.6 in [55]). The cases at the higher magnitudes of η are nearer the expected trend than those at lower values of η for the buoyancy aided cases. The text also states that separation occurs near $\eta \approx 0.8$. The data show no signs of separation, however.

To ensure that the flow in this wind tunnel can be considered valid for the shape factor analysis, an unheated case is desired. The unheated shape factor should fit the expected trend. Thus, an additional two data sets are now considered but are not part of the validation data presented. They include an unheated and heated flow at a Reynolds number (based on hydraulic diameter) of 13400. This flow is much slower than the cases

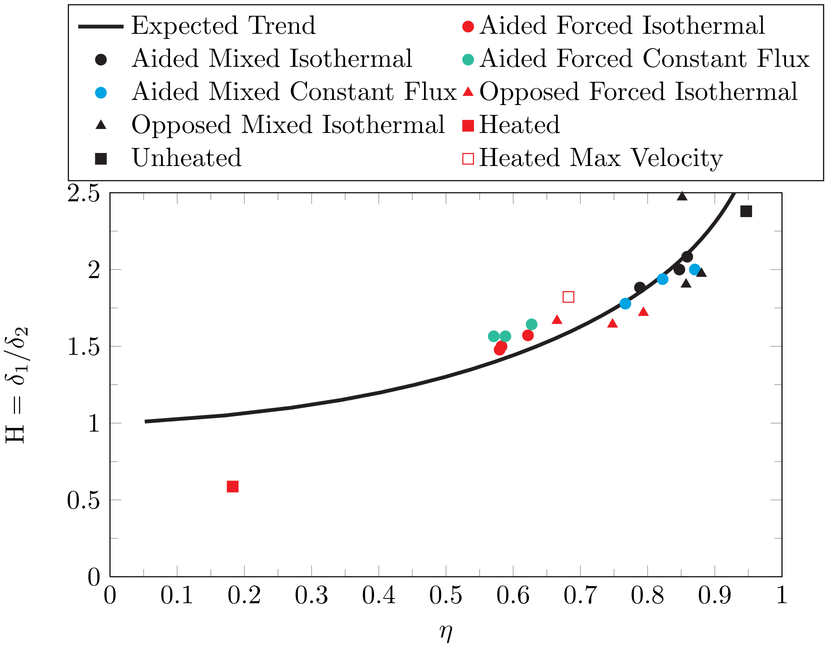

Fig. 5.30: A comparison of the classic shape factor with the expected trend as a function of the second shape factor η (see Eqn. 5.8).

considered previously, having a free stream velocity of 0.7 m/s. The buoyancy effects on the flow are significant for this flow rate. The velocity profiles for these additional cases are presented in Fig. 5.31. It is obvious that the heating accelerates the boundary layer when compared with the unheated case. In both cases, the Reynolds normal stress is small.

The corresponding shape factor correlation is included in Fig. 5.30 labed as Heated, Unheated, and Heated Max Velocity. Notice that when the free stream velocity is used to compute η in the Heated case (filled in red square), the resultant point is far different from an expected trend. The free stream velocity is used in the literature and the other cases previously presented. However, if the maximum velocity is used (Heated Max Velocity, hollow red square), the point is closer to expected values. The unheated case is near the expected trend as well (filled in black square). This suggests that the boundary layers considered in this flow behave similarly to unheated boundary layers considered in the classical literature. Also, when discussing this shape factor trend, the maximum velocity should be used, particularly when significant accelerations are in the flow. The maximum velocity is higher than the free stream velocity for the very slow flow case shown by Fig. 5.31.

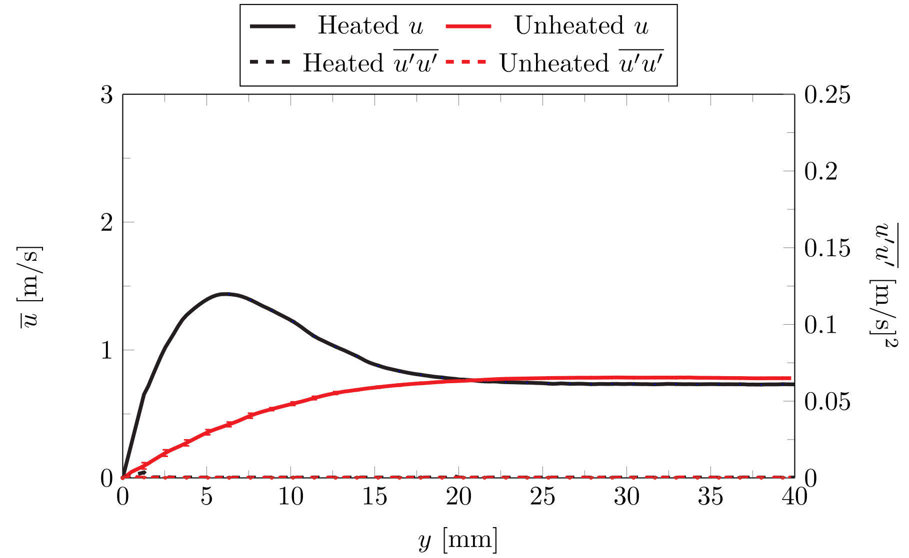

Fig. 5.31: The boundary layer velocity profiles for an unheated and heated low Reynolds number flow.

5.3.3 Buoyancy Influence on Heat Flux

Now we consider the buoyancy influence on heat flux from the plate. Wang *et al.* show data comparing the effects of buoyancy on heat transfer for buoyancy aided and opposed flow [4]. The Nusselt number is divided by a forced convection Nusselt number and plotted as a function of the special buoyancy parameter

$$Bo^* = \frac{\mathrm{Gr}^*}{\mathrm{Re}^{3.425}\mathrm{Pr}^{0.8}}. \tag{5.10}$$

This is shown in Fig. 5.32 and is compared with the data presented in [4].

In this analysis, the Nusselt number Nu characteristic length is the hydraulic diameter of the test section (12 in.). The developing, variable property forced convection Nusselt number Nu_f is

$$\mathrm{Nu}_f = C \times 0.0228\mathrm{Re}^{0.79}\mathrm{Pr}^{0.4}\left(\frac{T_s}{T_\infty}\right)^{-0.34} \tag{5.11}$$

with

$$C = 1.0 + \left(\frac{x}{D_h}\right)^{-0.29} \exp\left(-0.07\frac{x}{D_h}\right) \times \left[0.69 + \frac{5520}{Re}\left(\frac{x}{D_h}\right)^{-0.7}\right] \tag{5.12}$$

as described in [4].

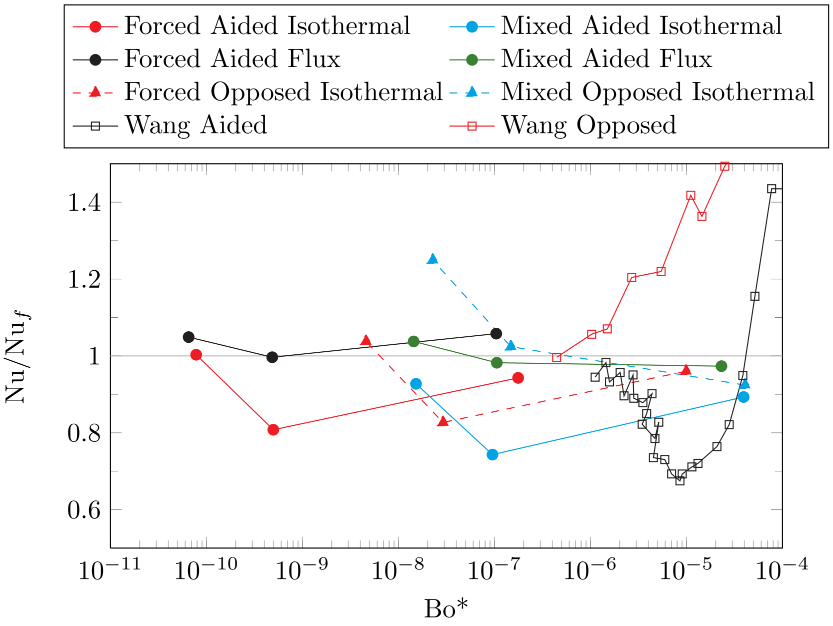

Fig. 5.32: A plot of the Nusselt number ratio versus the special buoyancy parameter for the data in this study and the data presented in [4].

It is shown in the Wang *et al.* data and study [4] that the buoyancy aided data experiences a suppression of heat transfer followed by a recovery of the heat flux for an increase in buoyancy effects. The data obtained in this study shows a similar trend. For example, the mixed buoyancy aided isothermal case shows a decrease in the Nusselt number ratio from position 1 to 2 and an increase again from 2 to 3 (right to left in Fig. 5.32). The forced aided isothermal trend shows a similar heat flux suppression, but with smaller magnitude than the mixed convection aided isothermal case. The constant heat flux cases show a flat trend, not giving any significant suppression of the heat flux due to buoyancy. The buoyancy opposed forced case shows an impairment of heat flux similar to the buoyancy aided case. However, the buoyancy opposed mixed case shows an improvement of heat flux due to the effect of buoyancy.

5.3.4 Shear Velocity and Shear Profile

There is another method that can be used to compute the shear velocity from the data. The total shear stress is the sum of the Reynolds stress ($-\rho\overline{u'v'}$) and the viscous stress, $\tau(y) = -\rho\overline{u'v'} + \mu d\overline{u}/dy$ [56]. The total shear stress is linear in fully developed pipe and channel flow due to the absence of streamwise acceleration [56]. The intercept at $y = 0$ is the total shear stress at the wall, and is used to find the friction velocity tabulated in the previous sections. Those tables are repeated for discussion in this section.

Figure 5.33 shows the total shear stress for the buoyancy aided isothermal forced convection case. This case has negligible streamwise acceleration and the second and third positions appear to be is fully developed. The trends closely match the linear fit, except nearest the wall. The shear stress is expected to be zero in the free stream. As is shown, the first position nearly reaches the free stream shear stress, but the second and third positions do not. The velocity profiles in Fig. 5.3 show that the free stream velocity is not measured except nearly at the first position. This is why the second and third positions shear stress do not go to zero within the bounds of the plot.

Figure 5.34 shows the total shear stress trends for the buoyancy aided isothermal mixed convection case. The flow is not fully developed and has significant acceleration effects from buoyant forces, causing disagreement with the theory that the shear stress profile should be linear. The first position trend is the most different from the linear fit. As the trends are all near zero at the furthest points from the wall ($y \approx 14$ mm), the free stream velocity is measured in these profiles. This is confirmed by reviewing Fig. 5.7. The non-linear nature of the shear stress profile suggests that this is a poor method for estimating the friction velocity in the mixed convection regime.

Figure 5.35 shows the total shear stress for the buoyancy aided constant flux forced convection case. This figure shows similar trends to the isothermal case in Fig. 5.33. As was previously discussed, the boundary layer velocity profiles are very similar, so the similarity in the shear stress is not unexpected. It is worth noting that the data near the wall (inwards

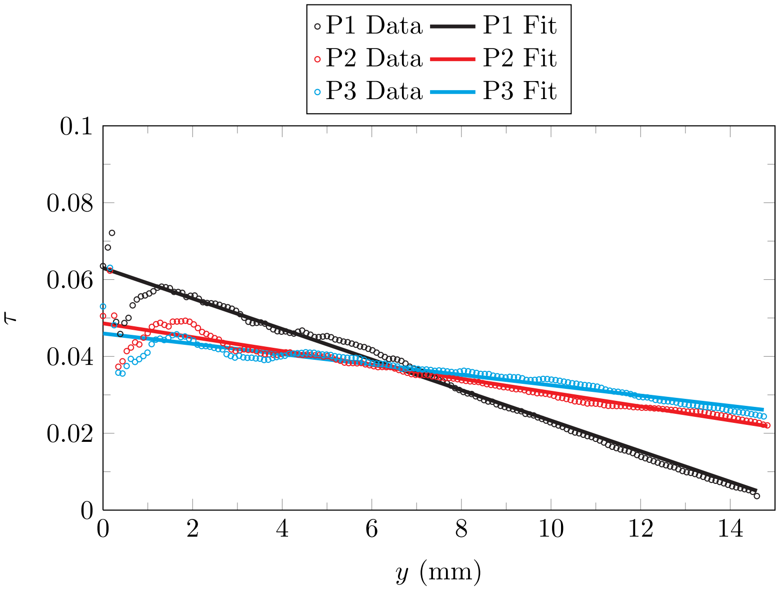

Fig. 5.33: The total shear stress profile with a linear fit for the buoyancy aided isothermal forced convection case.

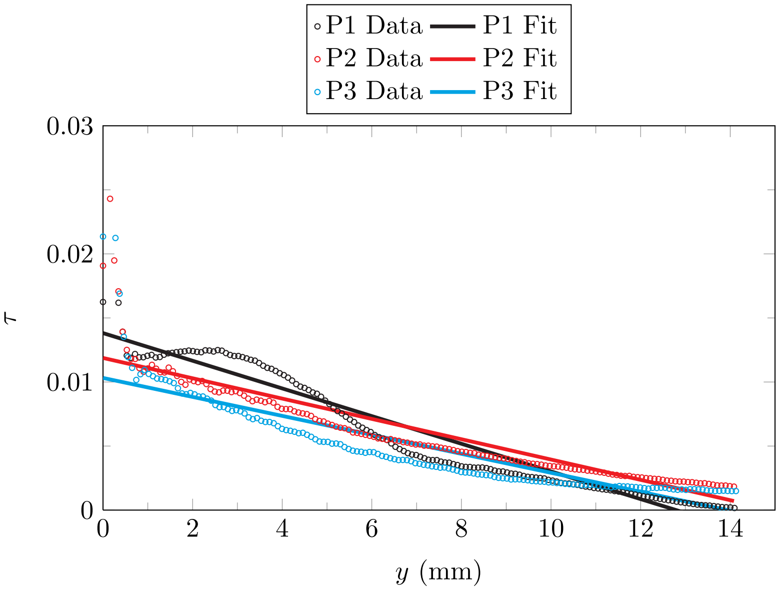

Fig. 5.34: The total shear stress profile with a linear fit for the buoyancy aided isothermal mixed convection case.

from 2 mm.) shows a slightly different trend than the isothermal forced convection case. Also, the data for position 2 and 3 do not cross in this case, as they do in the isothermal case (Fig. 5.33).

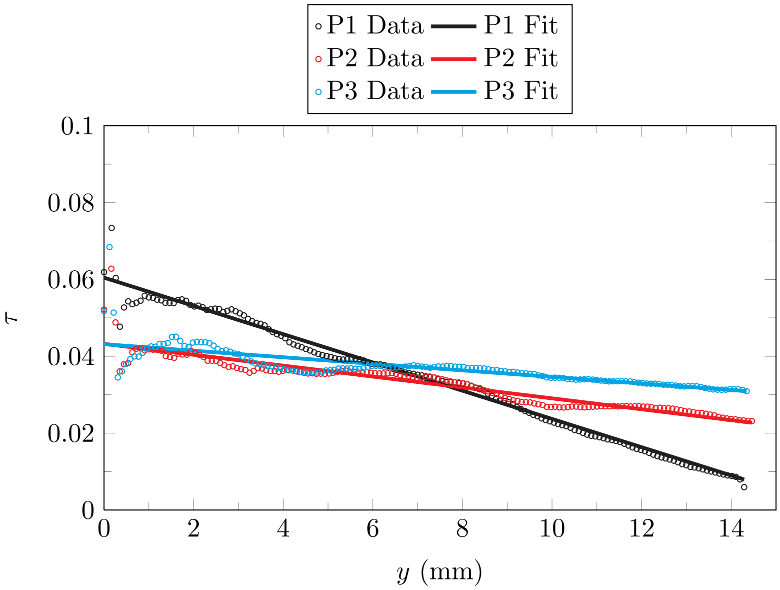

Fig. 5.35: The total shear stress profile with a linear fit for the buoyancy aided constant flux forced convection case.

The total shear stress for the buoyancy aided constant heat flux mixed convection case is shown in Fig. 5.36. The trends are not similar to the isothermal counterpart in Fig. 5.34. At each streamwise location, the constant heat flux case has similar wall shear stress, whereas the isothermal case does not. They both do exhibit a non-linear profile, particularly at the first position. Again, this is no surprise, as the linearity is only expected in fully developed turbulent flow, and the mixed cases are neither fully developed nor fully turbulent.

The shear stress at $y = 0$ is used to find the friction velocity. For the forced convection cases, the wall shear stress is used directly to compute u_τ. However, for the mixed convection cases, this value is not accurate since the trends are not linear.

Table 5.11 shows the previously presented friction velocities, with the addition of the friction velocity resulting from the total shear stress linear fit for the buoyancy aided isothermal forced convection case. With the exception of the first position, this method is near the other methods for predicting the friction velocity. The first position gives a high estimate

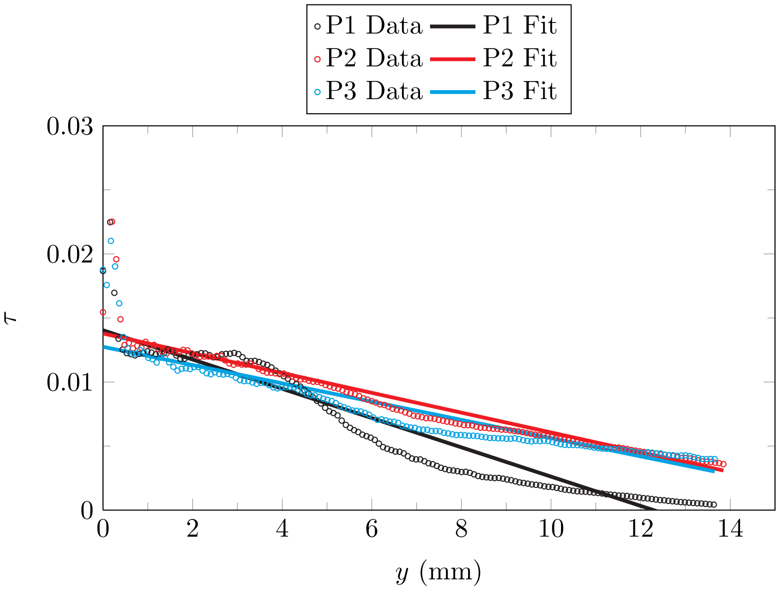

Fig. 5.36: The total shear stress profile with a linear fit for the buoyancy aided constant flux mixed convection case.

of the shear velocity using the total shear method. It is interesting that this method is most closely matched with the Spalding fit method using the classical parameters of κ and B.

Table 5.11: Shear velocity from the Spalding fit, and the shear velocity from a linear fit near the wall at the heat flux sensor positions for the buoyancy aided isothermal forced convection case. The computed friction velocity from the CFD simulation is also tabulated, along with the friction velocity from the total shear velocity. The two Spalding fit shear velocities correspond to the two cases with different fit parameters described previously (see Table 5.2).

Position	u_τ Spalding	u_τ Linear	u_τ CFD	u_τ Total Shear
P1	0.248	0.258±0.004	0.215	0.250
P1	0.235			
P2	0.234	0.230±0.004	0.231	0.248
P2	0.204			
P3	0.235	0.230±0.004	0.233	0.229
P3	0.210			

The shear velocity is again tabulated in Table 5.12 for the buoyancy aided constant heat flux forced convection case with the addition of u_τ from the total linear shear stress method. The linear shear stress method provides a similar shear velocity to the other methods for this case, but slightly under-predicts the value compared to the other methods for the second and third positions. The total shear method over-predicts the friction velocity at the first position compared to the three point linear fit and the CFD, but under-predicts when compared to the Spalding fit at the first position.

Table 5.12: Shear velocity from the Spalding fit, and the shear velocity from a linear fit near the wall at the heat flux sensor positions for the buoyancy aided constant heat flux forced convection case. The two Spalding fit shear velocities correspond to the two cases with different fit parameters described previously (see Table 5.8).

Position	u_τ Spalding	u_τ Linear	u_τ CFD	u_τ Total Shear
P1 P1	0.248 0.262	0.248±0.011	0.200	0.248
P2 P2	0.233 0.210	0.230±0.012	0.203	0.227
P3 P3	0.232 0.206	0.240±0.015	0.206	0.226

The two components that make up the total shear inspire another question; can the components of the total shear be used for validation? The two components that are summed to compute the total shear stress previously presented are $\mu du/dy$ and $\rho\overline{u'v'}$. These components are plotted for the three positions of the buoyancy aided isothermal forced convection case and compared with the CFD computation of the same. One assumption necessary for the CFD components is that $-\overline{u'v'} = \epsilon_M \delta\overline{u}/\delta y$. The eddy diffusivity is ϵ_M and $\overline{u}$ is the measured average streamwise velocity. The models used for the forced convection case compute a turbulence viscosity μ_t that is related to the eddy diffusivity by $\mu_t = \rho\epsilon_M$ [18].

Figure 5.37 shows the shear stress components for the buoyancy aided forced isothermal case at the first position comparing the CFD computation to the experiment. As is shown, the CFD under-predicts the Reynolds stress compared to the experiment. Also, the CFD trend for the Reynolds stress is non-linear. The assumptions that make for a linear total shear stress are not valid for this case, as the flow is not fully developed. However, the experimental data show that the total shear stress is linear, but the CFD prediction is not linear.

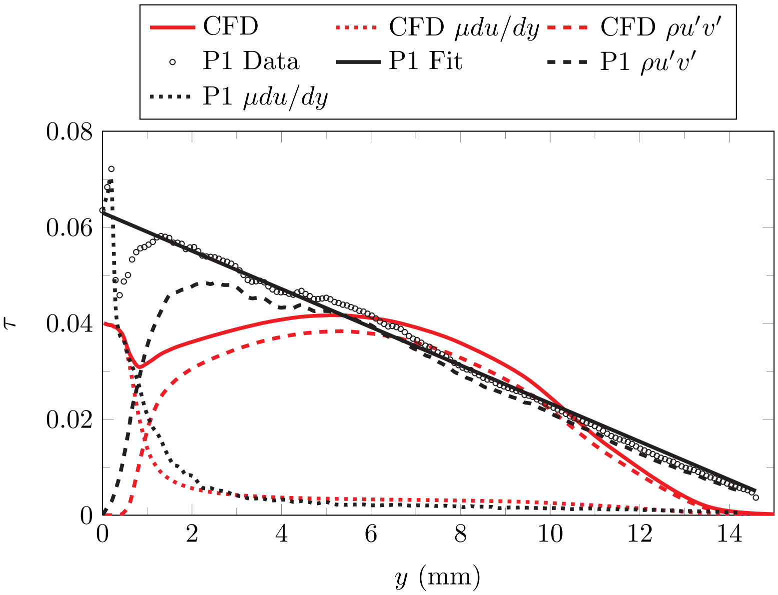

Fig. 5.37: The total shear stress profile with a linear fit for the buoyancy aided isothermal forced convection case at the first position. The $y+ = 10$ value is at $y = 0.73$ mm.

Figure 5.38 shows the shear stress components for the second position in the buoyancy aided forced isothermal case, comparing the CFD and experiment. The total shear stress at this position is linear, but the simulation still under-predicts the experiment Reynolds stress. The viscous stress is similar when comparing the CFD and the experiment, giving further credence to the limitations of the model to predict the Reynolds shear stress. The difference between the CFD simulation and the experiment in the viscous shear stress and the Reynolds shear stress within the viscous sublayer is significant.

Figure 5.39 shows the the shear stress components for the third position in the forced isothermal case, comparing the CFD and experiment. The total shear stress at this position is linear, but the simulation still under-predicts the experiment Reynolds stress. It is interesting that the near wall trends at the second and third positions are very similar (both experimentally and in the simulation). The viscous shear stress in the viscous sublayer does not follow the trend predicted in the experiment, as was the case at the second position.

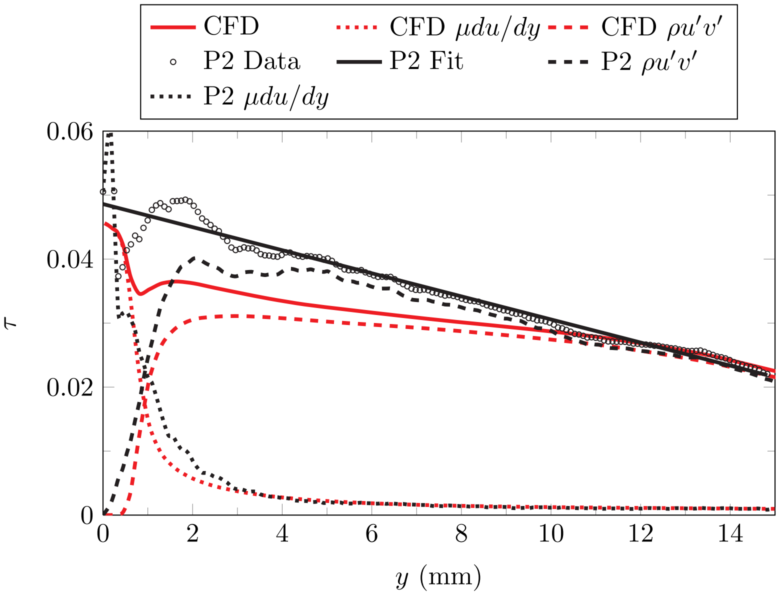

Fig. 5.38: The total shear stress profile with a linear fit for the buoyancy aided isothermal forced convection case at the second position. The $y+ = 10$ value is at $y = 0.87$ mm.

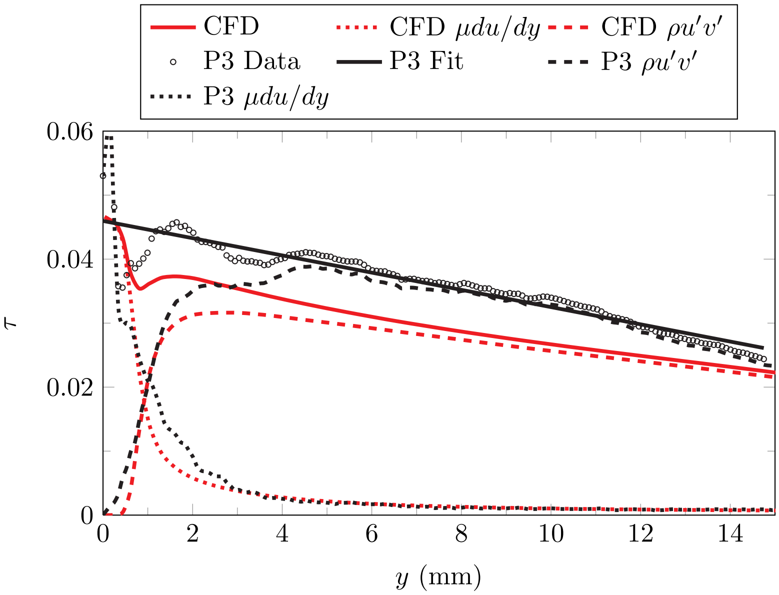

Fig. 5.39: The total shear stress profile with a linear fit for the buoyancy aided isothermal forced convection case at the third position. The $y+ = 10$ value is at $y = 1.13$ mm.

5.4 Uncertainty and Repeatability

To quantify the uncertainty of the measurements, several methods are used. The PIV position uncertainty is found using three different methods to compute the wall position. The position of the wall is the primary source of uncertainty for the position, since all spatial dimensions in the PIV data are derived from the wall location. For a discussion of this component of uncertainty, refer to Chapter 4.3.4. The PIV data uncertainty is quantified as outlined in the literature mentioned earlier.

The repeatability of the velocity measurement is considered as suggested by Oberkampf and Trucano [6]. Figure 5.40 shows the boundary layer velocity for several repeats of the buoyancy aided forced isothermal data at each position. The velocity profile for the boundary layer over the first heat flux sensor (P1 r1-r3) is repeatable. The profiles over the second and third heat flux sensors are repeatable as well. These cases were recorded several months apart, with a disassemble and remount of the PIV equipment between r2 and r3 cases. The free stream velocity $\overline{u}_\infty$ for these cases is 4.487 m/s.

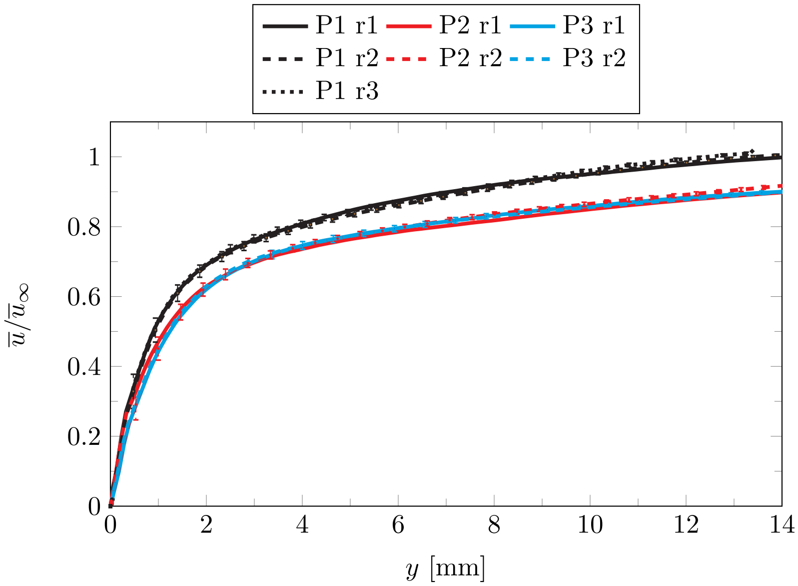

Fig. 5.40: The boundary layer streamwise velocity profiles for the flow over the three positions for three repeats of the isothermal forced aided flow measurement.

Figure 5.41 shows these profiles as a difference from the mean of the data, also called the velocity residual $\Delta\overline{u}$. The residual is normalized by the mean $((\overline{u}_{P1,r1} - \overline{u}_{P1mean})/\overline{u}_{P1mean})$. We note that between replications, the camera was removed, replaced, and recalibrated. The mean of the profiles at the first position is used to compute the residual at the first position, and similarly for the other two positions. It is shown that 3 repeats of the boundary layer velocity over the first heat flux sensor have an average residual level of less than 20% with the largest values near the wall. The PIV data near the wall has larger uncertainty. The large residual here could also result from an error in the y position in the presence of the large velocity gradient. This suggests that the repeatability of the boundary layer velocity measurement is within 20% with an average of less than 1%.

The Reynolds normal stress residual $\Delta\overline{u'u'}$ is similarly plotted in Fig. 5.42. The peak Reynolds normal stress residual is 0.6 with an average of less than 10%. The increasing residual levels toward the free stream is due to the very small values of $\overline{u'u'}$.

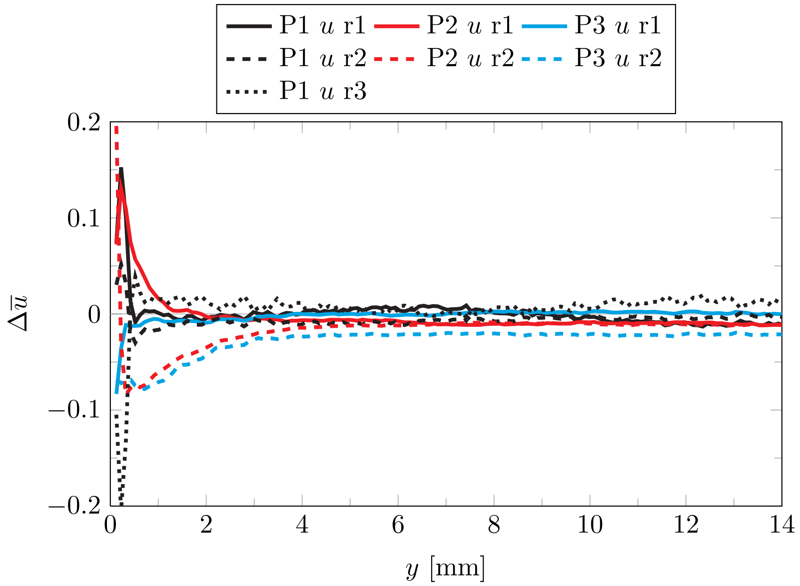

Fig. 5.41: The boundary layer streamwise velocity residuals for the flow over the three positions for three repeats of the isothermal forced aided flow measurement.

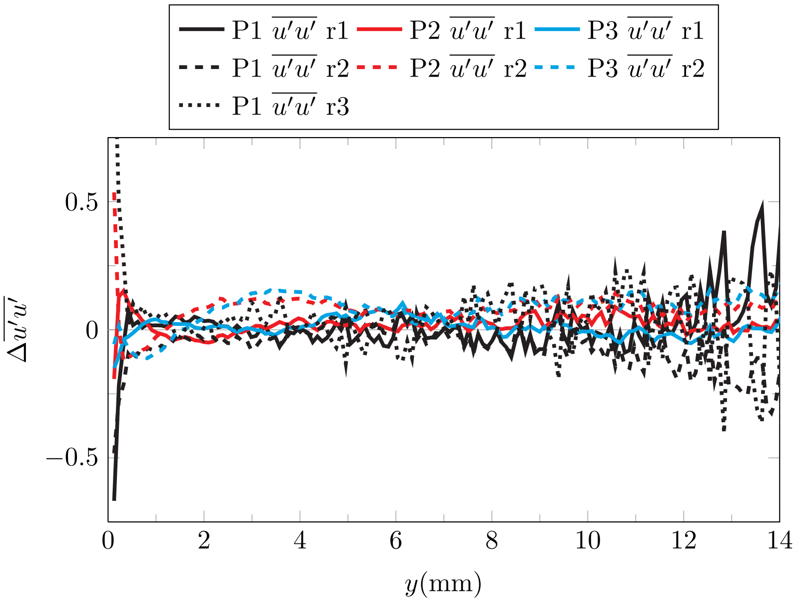

Fig. 5.42: The boundary layer streamwise velocity Reynolds normal stress residuals for the flow over the three positions for three repeats of the isothermal forced aided flow measurement.

Chapter 6

Conclusions

Validation of CFD simulations is an important aspect of pre-production analysis for many complicated systems, including nuclear reactors. The design of a validation experiment is presented. This design allows for simultaneous measurement of the boundary conditions and system response quantities. The boundary conditions measured include: the wall temperatures, flow inlet temperature, inlet velocity with statistical quantities sufficient to quantify turbulence model parameters, and atmospheric conditions. These measured boundary conditions were designed with a gaol of Level 2 Completeness in the Validation Experiment Data Completion table [11].

The boundary condition treatment is outlined, with uncertainty quantification. It is not prudent to present the boundary conditions in a report such as this, so a website was created to disseminate the boundary conditions and system response quantities. This website also contains the details necessary for an external party to conduct validation studies of their own. They simply gather the necessary details from the pages describing the experimental apparatus, material properties, boundary conditions, and system responses. They can use the boundary conditions to compute their own simulations. Then they can compare their simulation system responses to those on the website (which are the ones presented in this work). A validation study is mostly useless unless the data are made available for model developers around the world to use.

The repeatability of the measurements are discussed in Chapter 5.4, where it is shown that the boundary layer measurements are repeatable. To properly quantify that repeatability, the velocity residuals were also presented. The worst case error of repeatability is shown to be 20%, with an average repeatability error of 1%. The repeatability error could be combined with the velocity uncertainty to provide a more accurate estimate of the total velocity uncertainty.

Another aspect of the uncertainty of the velocity measurements is the position uncertainty. As there are several methods that can be employed to find the wall position, only a few of these methods were used to estimate the wall position and uncertainty, and therefore the overall velocity position uncertainty. It was found that the position uncertainty can be as high as 0.2 mm, with an average of our cases below 0.1 mm, depending on the method used to find the wall position.

The system responses presented also provide much insight into the behavior of convective boundary layer flow. Forced convection flow is usually considered to have no influence from buoyant forces. However, the unique capability of this experimental apparatus to change gravity without changing other boundary conditions shows that this is not always true. Even when the $\mathrm{Gr}_x/\mathrm{Re}_x^2$ ratio is in the forced convection regime, the effects of buoyancy are still present. This is even more prevalent in the mixed convection case, but this was expected. The isothermal heating and constant flux heating did not effect the boundary layer profiles as much as the effect of buoyancy from gravity changes. The heat flux SRQ was changed significantly with the change in heating conditions, however.

The mixed convection buoyancy aided case shows a laminarizing flow. The flow inlet starts with a laminar-like profile, and develops into a more turbulent profile before returning to the laminar-like flow. The heat flux trend also provides some insight into this phenomenon, where the flux at the second position is lower than expected. The impairment of the heat flux is further quantified by using a Nusselt number ratio and a special buoyancy parameter. It is shown that buoyancy tends to suppress the heat flux and then improve it, depending on the flow rate and orientation. It is noted that the $\mathrm{Gr}/\mathrm{Re}^2$ ration is nearly identical for the forced convection buoyancy aided and opposed cases, as well as for the mixed buoyancy aided and opposed cases. The momentum thickness is also compared as a function of the direction of gravity. The laminarizing flow shows a decrease in the momentum thickness during the onset of laminarization.

The classical boundary layer shape functions were also presented. It was found that even this convective flow behaves as an unheated boundary layer, so long as similar pressure gradients are in effect. It was also found that when the flow rate is very slow (buoyancy effects are large), the shape factors agree with expected trends so long as the maximum velocity is used instead of the free stream velocity.

Several simulations were conducted using models that were expected to be reasonably accurate for these flow conditions. The simulations are presented simply to show that the measured boundary conditions are sufficient to define the boundary conditions in the models presented. The simulation response quantities show that the models may predict the flow reasonably well, but Reynolds stress or heat flux may not be as well predicted.

References

[1] Idaho National Laboratory, "Module 05a Prismatic HTGR Core Design Description," 2010, from `https://inlportal.inl.gov/portal/server.pt/community/ngnp_public_documents` [retrieved Dec. 2013].

[2] Oberkampf, W. L., Sindir, M., and Conlisk, A., "Guide for the Verification and Validation of Computational Fluid Dynamics Simulations," *American Institute of Aeronautics and Astronautics*, 1998.

[3] Oberkampf, W. L. and Roy, C. J., *Verification and Validation in Scientific Computing*, Cambridge University Press, New York, 2010.

[4] Wang, J., Li, J., and Jackson, J., "A Study of the Influence of Buoyancy on Turbulent Flow in a Vertical Plane Passage," *International Journal of Heat and Fluid Flow*, Vol. 25, No. 3, 2004, pp. 420–430.

[5] ASME, "ANSI Standard V&V 20. ASME Guide on Verification and Validation in Computational Dynamics and Heat Transfer," Tech. rep., American Society of Mechanical Engineers, 2008.

[6] Oberkampf, W. L. and Trucano, T. G., "Verification and Validation in Computational Fluid Dynamics," *Progress in Aerospace Sciences*, Vol. 38, No. 3, 2002, pp. 209–272.

[7] Wilson, G. E. and Boyack, B. E., "The Role of the PIRT Process in Experiments, Code Development and Code Applications Associated with Reactor Safety Analysis," *Nuclear Engineering and Design*, Vol. 186, No. 1, 1998, pp. 23–37.

[8] CFD-Online, "Validation Cases Links References," 2013, from http://www.cfd-online.com/Links/refs.html [retrieved Dec 2013].

[9] NPARC Alliance, "Turbulent Flat Plate," 2013, from http://www.grc.nasa.gov/WWW/wind/valid/fpturb/fpt urb.html [retrieved Dec 2013].

[10] ERCoFTC, "Classic Collection Database," 2013, from http://cfd.mace.manchester.ac.uk/ercoftac/classif.html [retrieved Dec. 2013].

[11] Oberkampf, W. and Smith, B., "Assessment Criteria for Computational Fluid Dynamics Validation Benchmark Experiments," *AIAA SciTech Conference*, 2014.

[12] Experimental Fluid Dynamics Laboratory, "Buoyancy Aided Forced Convection Database," 2014, http://efdl.neng.usu.edu/ValidationPages/FC_Validation/Main.html [retrieved May 2014].

[13] Timmins, B. H., Wilson, B. W., Smith, B. L., and Vlachos, P. P., "A Method for Automatic Estimation of Instantaneous Local Uncertainty in Particle Image Velocimetry Measurements," *Experiments in Fluids*, Vol. 53, No. 4, 2012, pp. 1133–1147.

[14] Warner, S. O., Smith, B. L., and Vlachos, P. P., “Autocorrelation Based Estimate of Particle Image Density in PIV,” Bulletin of the American Physical Society, DFD, San Diego, CA, 2012.

[15] Wilson, B. M. and Smith, B. L., “Uncertainty on PIV Mean and Fluctuating Velocity Due to Bias and Random Errors,” *Measurement Science and Technology*, Vol. 24, No. 3, 2013, pp. 035302.

[16] Wilson, B. M. and Smith, B. L., “Taylor-Series and Monte-Carlo-Method Uncertainty Estimation of the Width of a Probability Distribution Based on Varying Bias and Random Error,” *Measurement Science and Technology*, Vol. 24, No. 3, 2013, pp. 035301.

[17] Coleman, H. W. and Steele, W. G., *Experimentation, Validation, and Uncertainty Analysis for Engineers*, Wiley, Hoboken, NJ, 3rd ed., 2009.

[18] Kays, W. M., Crawford, M. E., and Weigand, B., *Convective Heat and Mass Transfer*, McGraw-Hill, New York, 4th ed., 2004.

[19] Lloyd, J. and Sparrow, E., “Combined Forced and Free Convection Flow on Vertical Surfaces,” *International Journal of Heat and Mass Transfer*, Vol. 13, No. 2, 1970, pp. 434–438.

[20] Gryzagoridis, J., “Combined Free and Forced Convection from an Isothermal Vertical Plate,” *International Journal of Heat and Mass Transfer*, Vol. 18, No. 7, 1975, pp. 911–916.

[21] McEligot, D. M. and Jackson, J. D., “Deterioration Criteria for Convective Heat Transfer in Gas Flow Through Non-Circular Ducts,” *Nuclear Engineering and Design*, Vol. 232, No. 3, 2004, pp. 327–333.

[22] Hattori, Y., Tsuji, T., Nagano, Y., and Tanaka, N., “Effects of Freestream on Turbulent Combined-Convection Boundary Layer Along a Vertical Heated Plate,” *International Journal of Heat and Fluid Flow*, Vol. 22, No. 3, 2001, pp. 315–322.

[23] Tsuji, T. and Nagano, Y., “Characteristics of a Turbulent Natural Convection Boundary Layer Along a Vertical Flat Plate,” *International Journal of Heat and Mass Transfer*, Vol. 31, 1988, pp. 1723–1734.

[24] Jackson, J. D., “Review of Some Experimental Studies of Turbulent Mixed Convection Covering a Wide Range Prandtl Number,” NURETH-14, Sept. 25-29, 2011.

[25] Jackson, J., “Studies of Buoyancy-Influenced Turbulent Flow and Heat Transfer in Vertical Passages,” *International Heat Transfer Conference 13*, Begel House Inc., Danbury, CT, 2006.

[26] Chen, T., Armaly, B., and Ramachandran, N., “Correlations for Laminar Mixed Convection Flows on Vertical, Inclined, and Horizontal Flat Plates,” *ASME Transactions Journal of Heat Transfer*, Vol. 108, 1986, pp. 835–840.

[27] Ramachandran, N., Armaly, B., and Chen, T., "Measurements and Predictions of Laminar Mixed Convection Flow Adjacent to a Vertical Surface," *Journal of Heat Transfer*, Vol. 107, No. 3, 1985, pp. 636–641.

[28] Hattori, Y., Tsuji, T., Nagano, Y., and Tanaka, N., "Characteristics of Turbulent Combined-Convection Boundary Layer Along a Vertical Heated Plate," *International Journal of Heat and Fluid Flow*, Vol. 21, No. 5, 2000, pp. 520–525.

[29] Krishnamurthy, R. and Gebhart, B., "An Experimental Study of Transition to Turbulence in Vertical Mixed Convection Flows," *Journal of Heat Transfer (Transcations of the ASME (American Society of Mechanical Engineers), Series C);(United States)*, Vol. 111, No. 1, 1989.

[30] Gavara, M. R., Dutta, P., and Seetharamu, K., "Mixed Convection Adjacent to Non-Isothermal Vertical Surfaces," *International Journal of Heat and Mass Transfer*, Vol. 55, No. 17, 2012, pp. 4580–4587.

[31] Yadav, V. and Kant, K., "Experimental Validation of Analytical Solutions for Vertical Flat Plate of Finite Thickness Under Natural-Convection Cooling," *Journal of Heat Transfer*, Vol. 130, 2008, pp. 032503–1.

[32] Abedin, M. Z., Tsuji, T., and Lee, J., "Turbulence Characteristics and Vortical Structures in Combined-Convection Boundary Layers Along a Heated Vertical Flat Plate," *International Journal of Heat and Mass Transfer*, Vol. 55, No. 15, 2012, pp. 3995–4002.

[33] Moretti, P. and Kays, W., "Heat Transfer to a Turbulent Boundary Layer with Varying Free-Stream Velocity and Varying Surface Temperature - An Experimental Study," *International Journal of Heat and Mass Transfer*, Vol. 8, No. 9, 1965, pp. 1187–1202.

[34] Perkins, K. R., Schade, K. W., and McEligot, D. M., "Heat Laminarizing Gas Flow in a Square Duct," *International Journal of Heat and Mass Transfer*, Vol. 16, 1973, pp. 897–916.

[35] Shehata, A. M. and McEligot, D. M., "Turbulence Structure in the Viscous Layer of Strongly Heated Gas Flows," Tech. rep., Lockheed Idaho Technologies Co., Idaho Falls, ID (United States), 1995.

[36] "Engineering Laboratory Design," PO Box 278, 2021 S. HWY 61, Lake City, MN 55041.

[37] National Instruments, *LabView*, from `http://www.ni.com/labview/` [retrieved Dec. 2013.

[38] Adrian, R. J. and Westerweel, J., *Particle Image Velocimetry*, Cambridge University Press, New York, 2010.

[39] Raffel, M., Willert, C., Wereley, S., and Kompenhans, J., *Particle Image Velocimetry–A Pratical Guide*, Springer Verlag, New York, 2007.

[40] LaVision, *DaVis® version 8.1*, Goettingen, Germany, from http://www.lavision.de/en/techniques/piv.php [retrieved Dec. 2013].

[41] Kähler, C., "General Design and Operating Rules for Seeding Atomisers," *Proceedings of the 5th International Symposium on Particle*, 2003.

[42] Velmex, Inc., *Linear Motor-driven Bi- and UniSlide Assemblies*, from `http://www.velmex.com/index.asp` [retrieved Dec. 2013].

[43] Howell, J. R., Siegel, R., and Mengüç, M. P., *Thermal Radiation Heat Transfer*, CRC Press, New York, 2011.

[44] Weast, R. C., Astle, M. J., and Beyer, W. H., *CRC Handbook of Chemistry and Physics*, Vol. 69, CRC Press, Boca Raton, FL, 1988.

[45] Incropera, F. P. and DeWitt, D. P., *Introduction to Heat and Mass Transfer*, Wiley, Hoboken, NJ, 5th ed., 2002.

[46] Barlow, J. B., Rae, W. H., and Pope, A., *Low-Speed Wind Tunnel Testing*, Wiley, New York, 3rd ed., 1999.

[47] Janna, W., *Design of Fluid Thermal Systems-SI Version*, Cengage Learning, Stamford, CT, 2010.

[48] Iverson, J. M., *Computational Fluid Dynamics Validation of Buoyant Turbulent Flow Heat Transfer*, Master's thesis, Utah State University, 2013.

[49] Kendall, A. and Koochesfahani, M., "A Method for Estimating Wall Friction in Turbulent Wall-Bounded Flows," *Experiments in Fluids*, Vol. 44, No. 5, Nov. 2007, pp. 773–780.

[50] CD-adapco, *STAR-CCM+*, from `http://www.cd-adapco.com/products/star-ccm-plus` [retrieved Dec. 2013].

[51] Celik, I. B., Ghia, U., Roache, P. J., et al., "Procedure for Estimation and Reporting of Uncertainty Due to Discretization in CFD Applications," *Journal of Fluids Engineering-Transactions of the ASME*, Vol. 130, No. 7, 2008.

[52] Lien, F., Chen, W., and Leschziner, M., "Low-Reynolds-Number Eddy-Viscosity Modelling Based on Non-Linear Stress-Strain/Vorticity Relations," *Engineering Turbulence Modelling and Experiments*, Vol. 3, 1996, pp. 91–100.

[53] Wilcox, D. C., "Formulation of the kw Turbulence Model Revisited," *AIAA Journal*, Vol. 46, No. 11, 2008, pp. 2823–2838.

[54] Department of Energy, NEUP, *Quality Assurance Requirements*, from `https://inlportal.inl.gov/portal/server.pt?open=514&objID=7362&parentname=CommunityPage&parentid=1&mode=2&in_hi_userid=2&cached=true` [retrieved Dec. 2013].

[55] Schlichting, H., *Boundary-Layer Theory*, McGraw-Hill, New York, 1968.

[56] Adrian, R. J., "Hairpin Vortex Organization in Wall Turbulence," *Physics of Fluids*, Vol. 19, No. 4, 2007, pp. 041301.

Appendices

Appendix A

Small Calibration Target

The calibration plate uses laser etched circles on an anodized aluminum plate. The dots are 0.980 mm (0.039 in) in diameter and spaced 3.175 mm (0.125 in) apart.

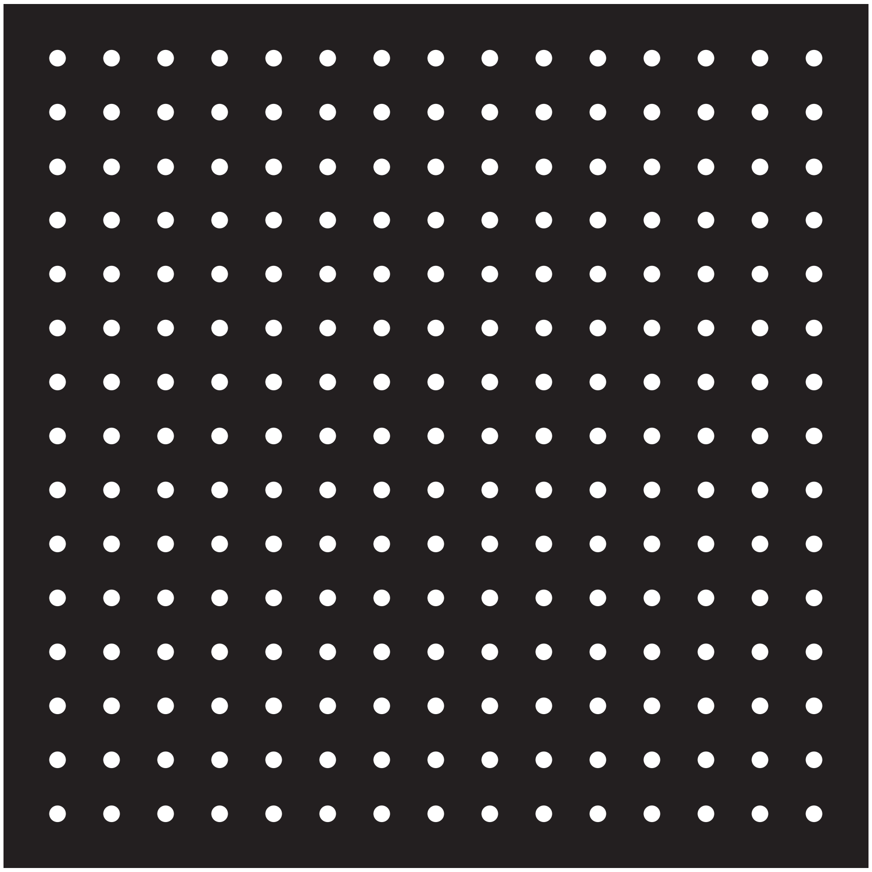

Fig. A.1: An image of the calibration target built to dewarp the SRQ data images.

Appendix B

Rotatable Buoyancy Tunnel Schematic

The schematic of the wind tunnel, provided by Engineering Laboratory Design, Inc. and used with permission.

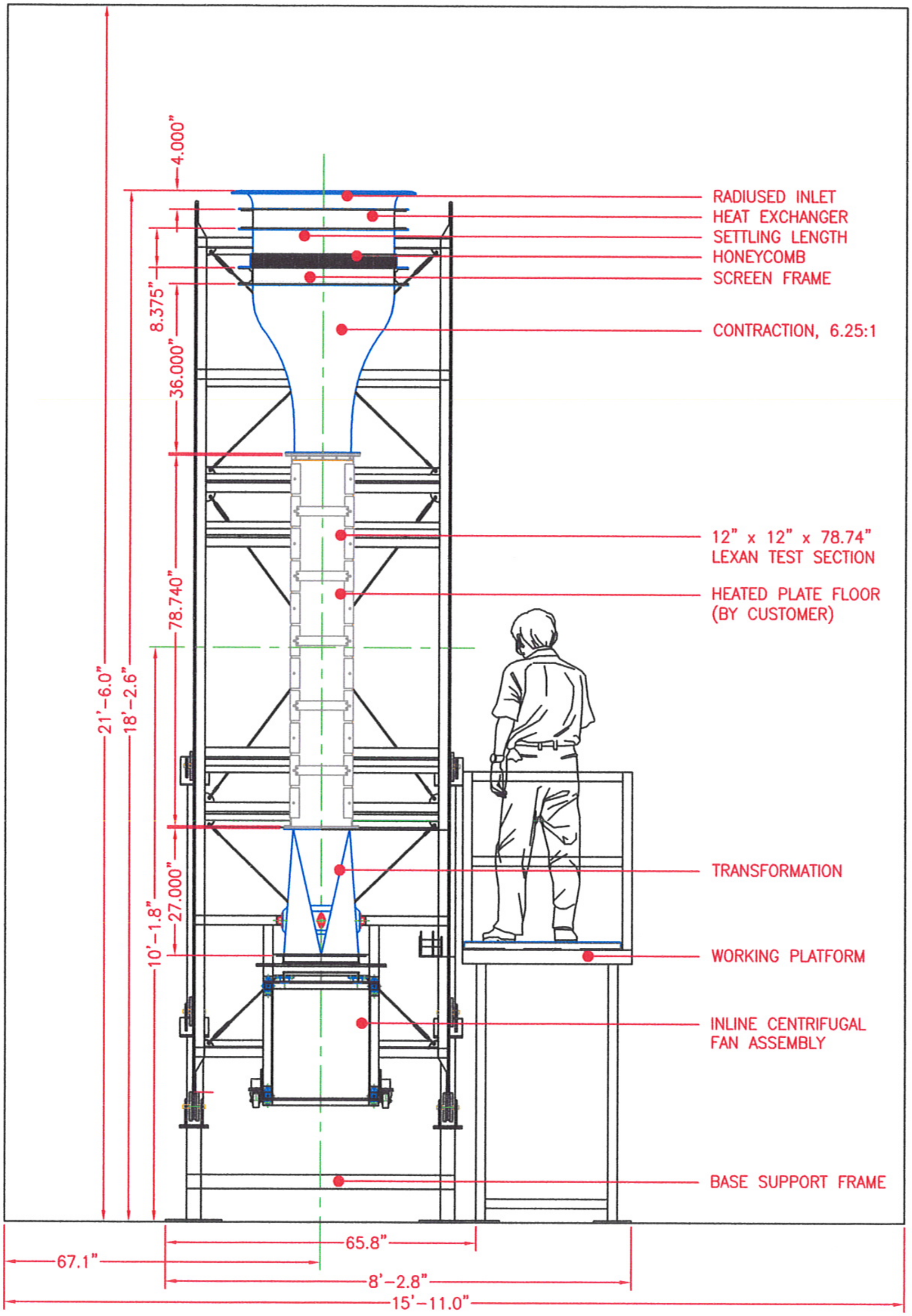

SECTION A-A

PROJECT: 12" O.C. ROTATING WIND TUNNEL
END ELEVATION - SECTION A-A

ORGANIZATION: UTAH STATE UNIVERSITY

REFERENCE: PO NO. P0103934

DATE: 9/13/10

SCALE: 3/8" - 1'-0"

ENGINEERING LABORATORY DESIGN, INC.
P.O. Box 278
Lake City, Minnesota 55041 USA
800-795-8536 FAX 651-345-5095

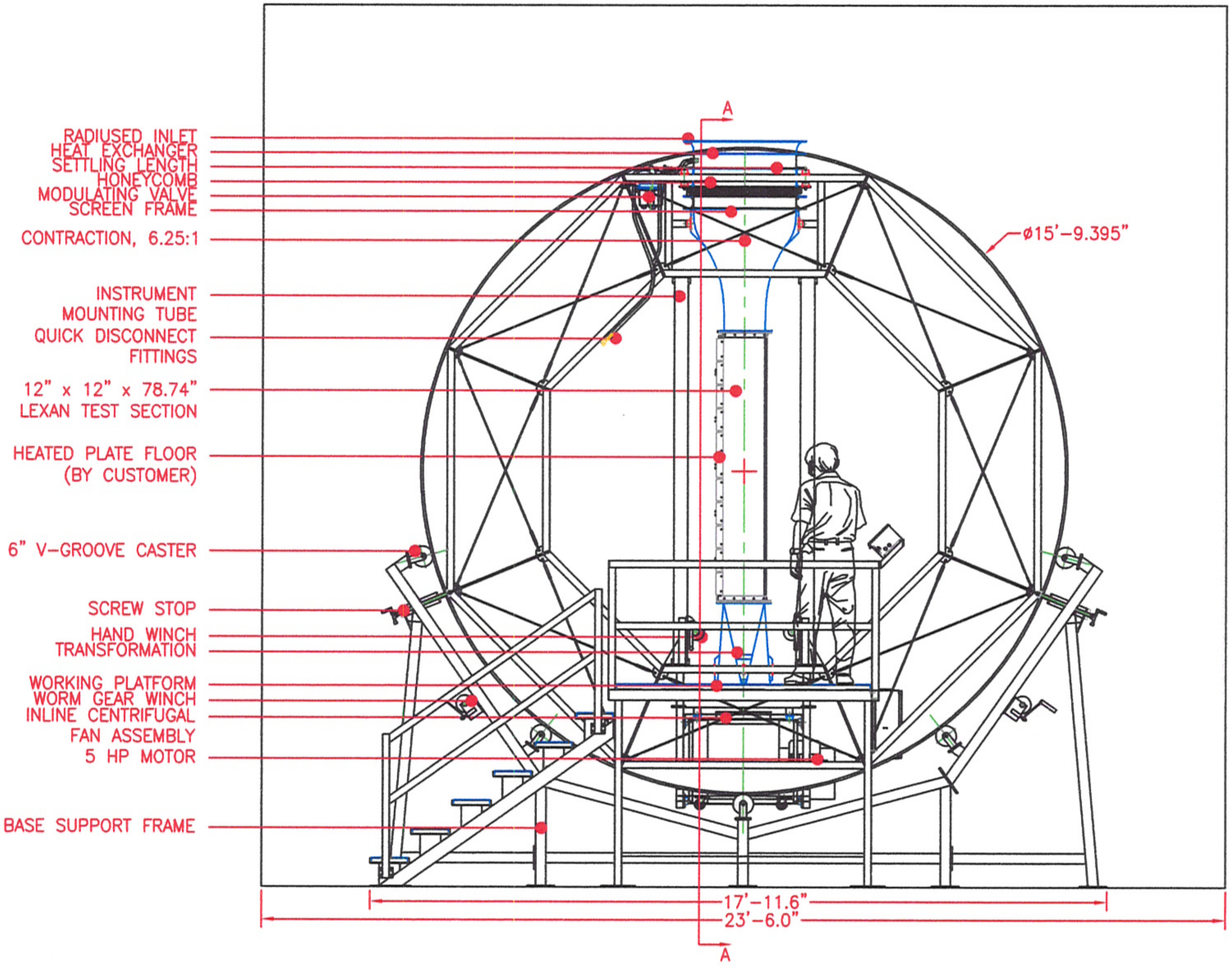

ENGINEERING LABORATORY DESIGN, INC.
P.O. Box 278
Lake City, Minnesota 55041 USA
800-795-8536 FAX 651-345-5095

THIS DRAWING AND THE INFORMATION THAT IT CONTAINS ARE THE PROPERTY OF ENGINEERING LABORATORY DESIGN, INC. REPRODUCTION AND/OR TRANSMISSION WITHOUT EXPRESS WRITTEN AUTHORIZATION IS PROHIBITED.

PROJECT: 12" O.C. ROTATING WIND TUNNEL
OVERALL ELEVATION

ORGANIZATION: UTAH STATE UNIVERSITY

REFERENCE: PO NO. P0103934
DATE: 9/13/10
SCALE: 1/4" = 1'-0"

Appendix C

Test Section Schematics

Schematics of the test section walls. The order of the drawings is

1. Left Wall

2. Right Wall

3. Top Wall 1^{st} Section

4. Top Wall 2^{nd} Section

5. Top Wall 3^{rd} Section

6. Inlet Floor

REVISION HISTORY

REV	DESCRIPTION	DATE	APPROVED

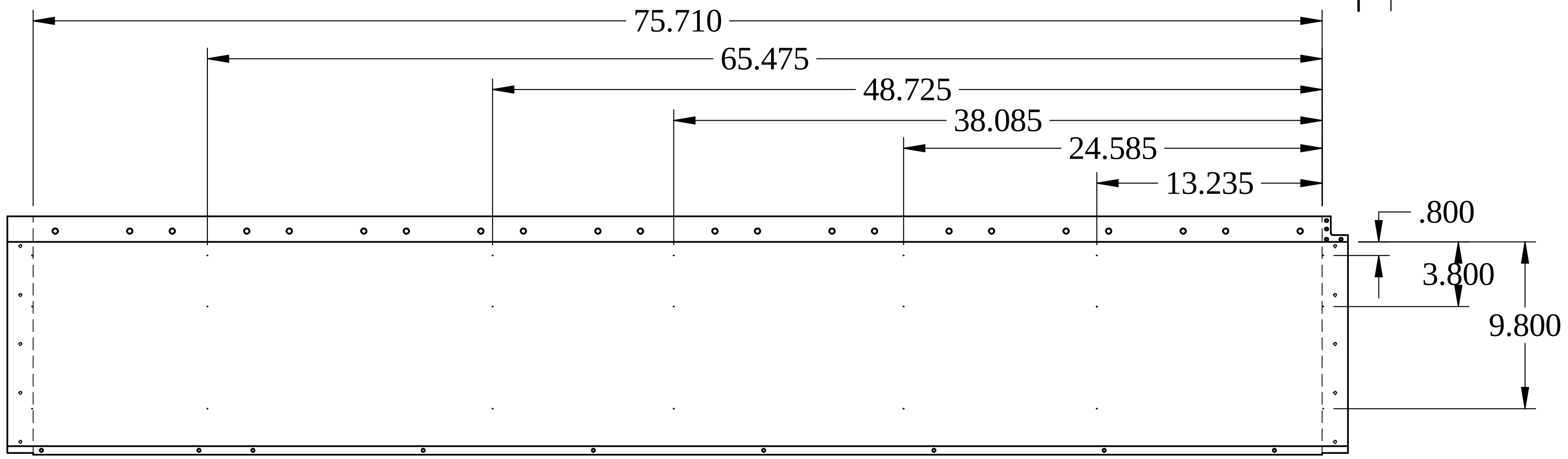

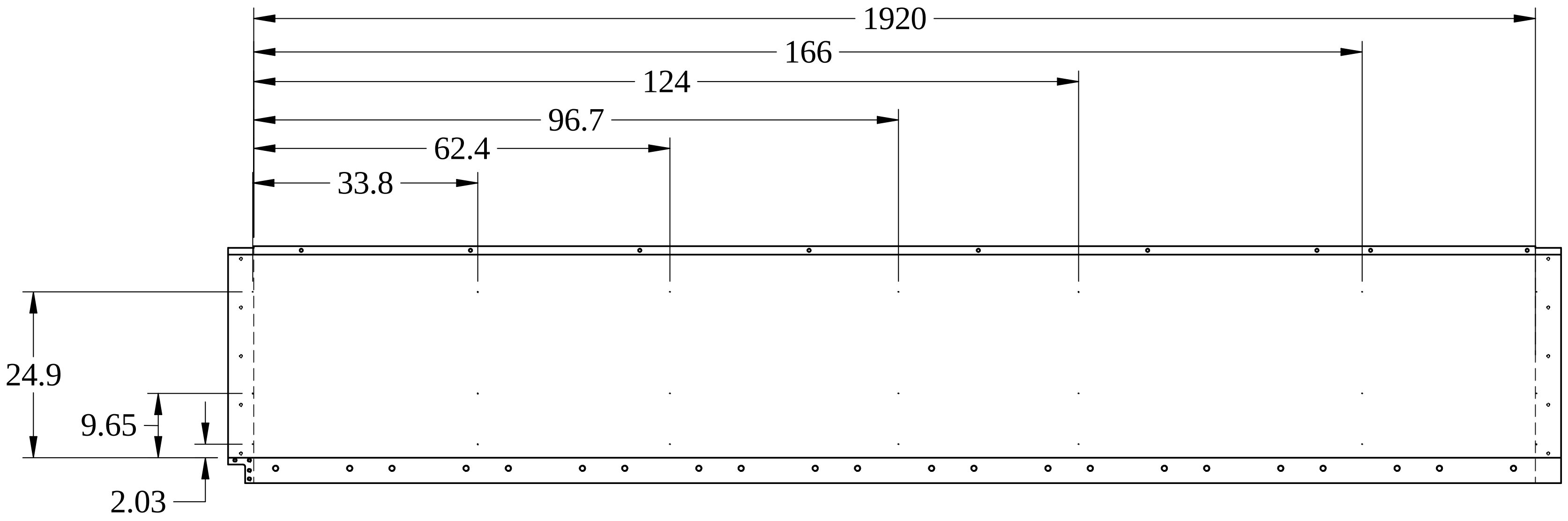

	NAME	DATE
DRAWN	EFDL	11/05/12
CHECKED		
ENG APPR		
MGR APPR		

UNLESS OTHERWISE SPECIFIED
DIMENSIONS ARE IN MILLIMETERS
ANGLES ±X.X°
2 PL ±X.XX 3 PL ±X.XXX

Solid Edge

TITLE

SIZE A2 | DWG NO | REV

FILE NAME: Left Side Mark 2_2.dft

SCALE: | WEIGHT: | SHEET 1 OF 1

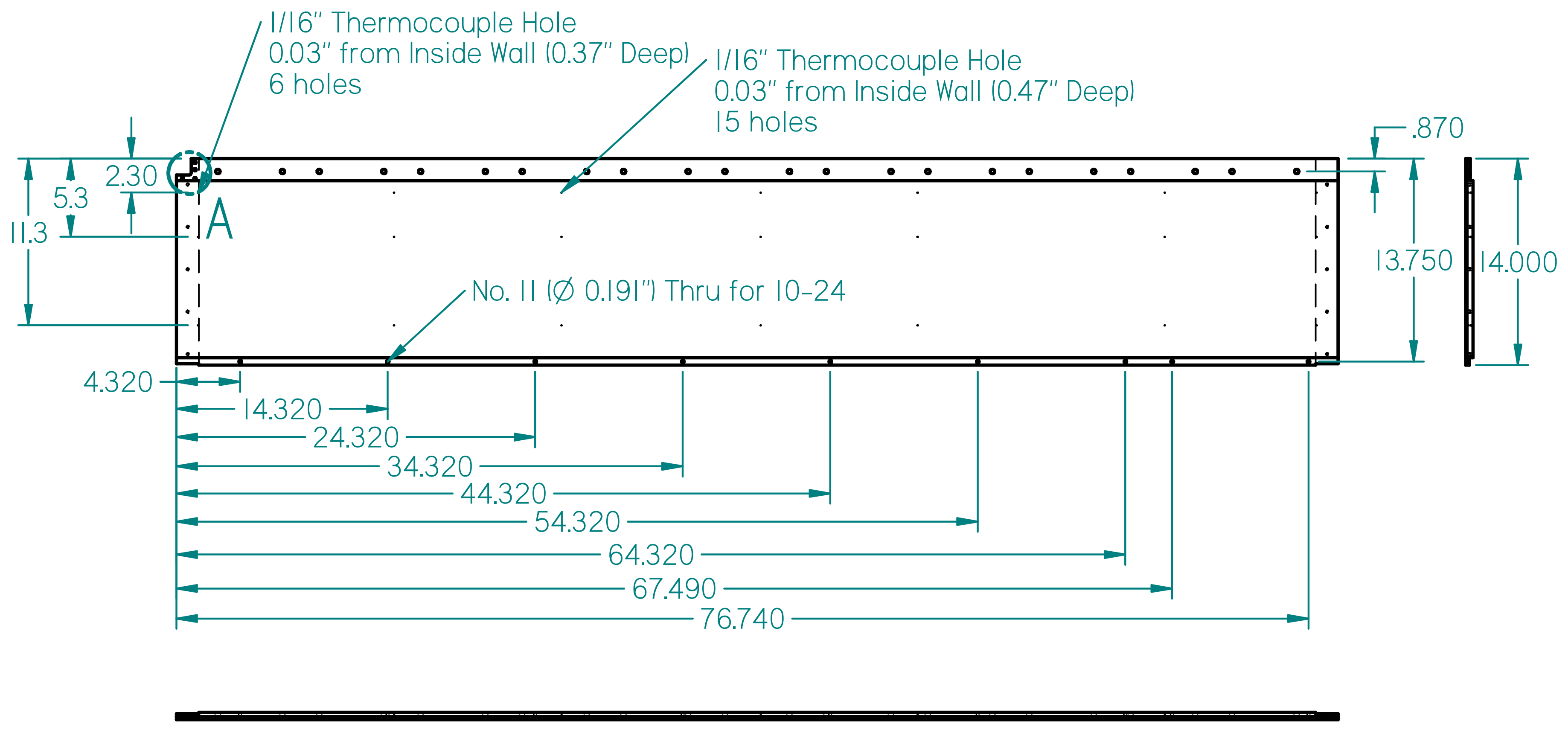

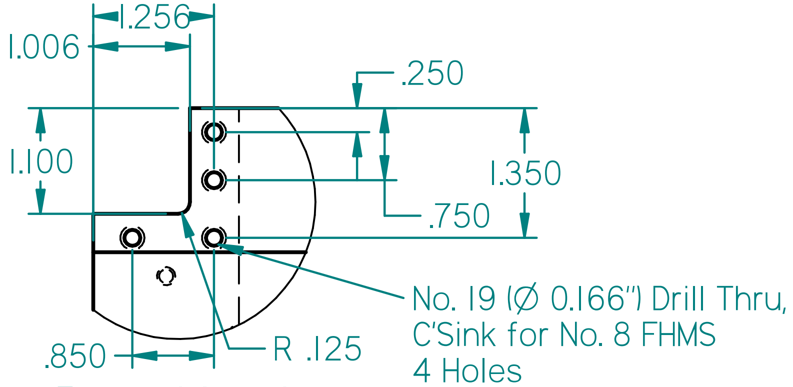

DETAIL A

	NAME	DATE
DRAWN	Jeff_N7	01/20/12
CHECKED		
ENG APPR		
MGR APPR		

UNLESS OTHERWISE SPECIFIED
DIMENSIONS ARE IN INCHES
ANGLES ±X.X°
2 PL ±X.XX 3 PL ±X.XXX

Right Side Wall

TITLE
Right Side 2

SIZE A4
DWG NO
REV

FILE NAME: Right Side Mark 2.2.dft

SCALE:
WEIGHT:
SHEET 1 OF 1

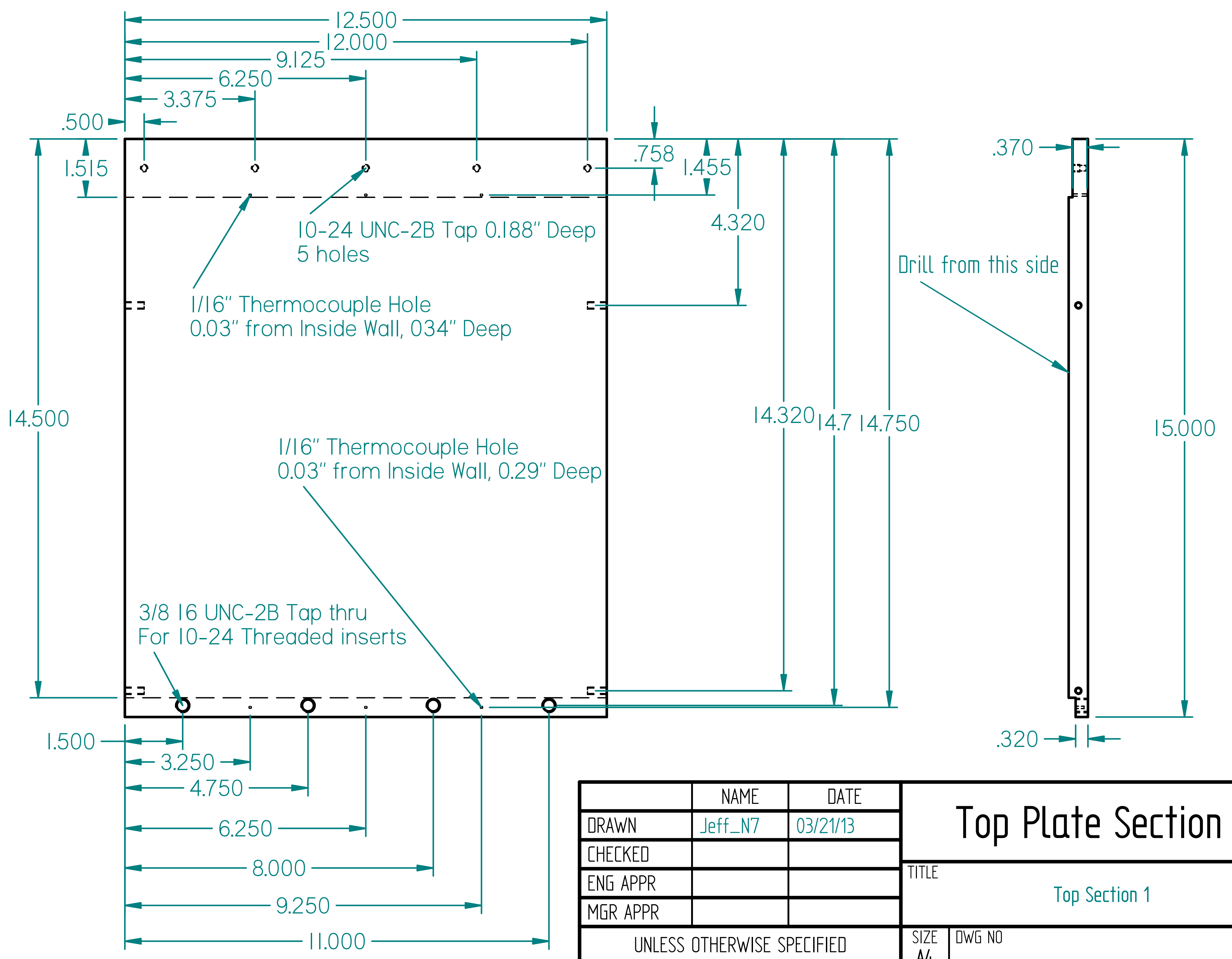

	NAME	DATE
DRAWN	Jeff_N7	03/21/13
CHECKED		
ENG APPR		
MGR APPR		

UNLESS OTHERWISE SPECIFIED
DIMENSIONS ARE IN INCHES
ANGLES ±X.X°
2 PL ±X.XX 3 PL ±X.XXX

Top Plate Section 1

TITLE
Top Section 1

SIZE A4
DWG NO
REV

FILE NAME: Top Mark 2 section 1b.dft

SCALE:
WEIGHT:
SHEET 1 OF 1

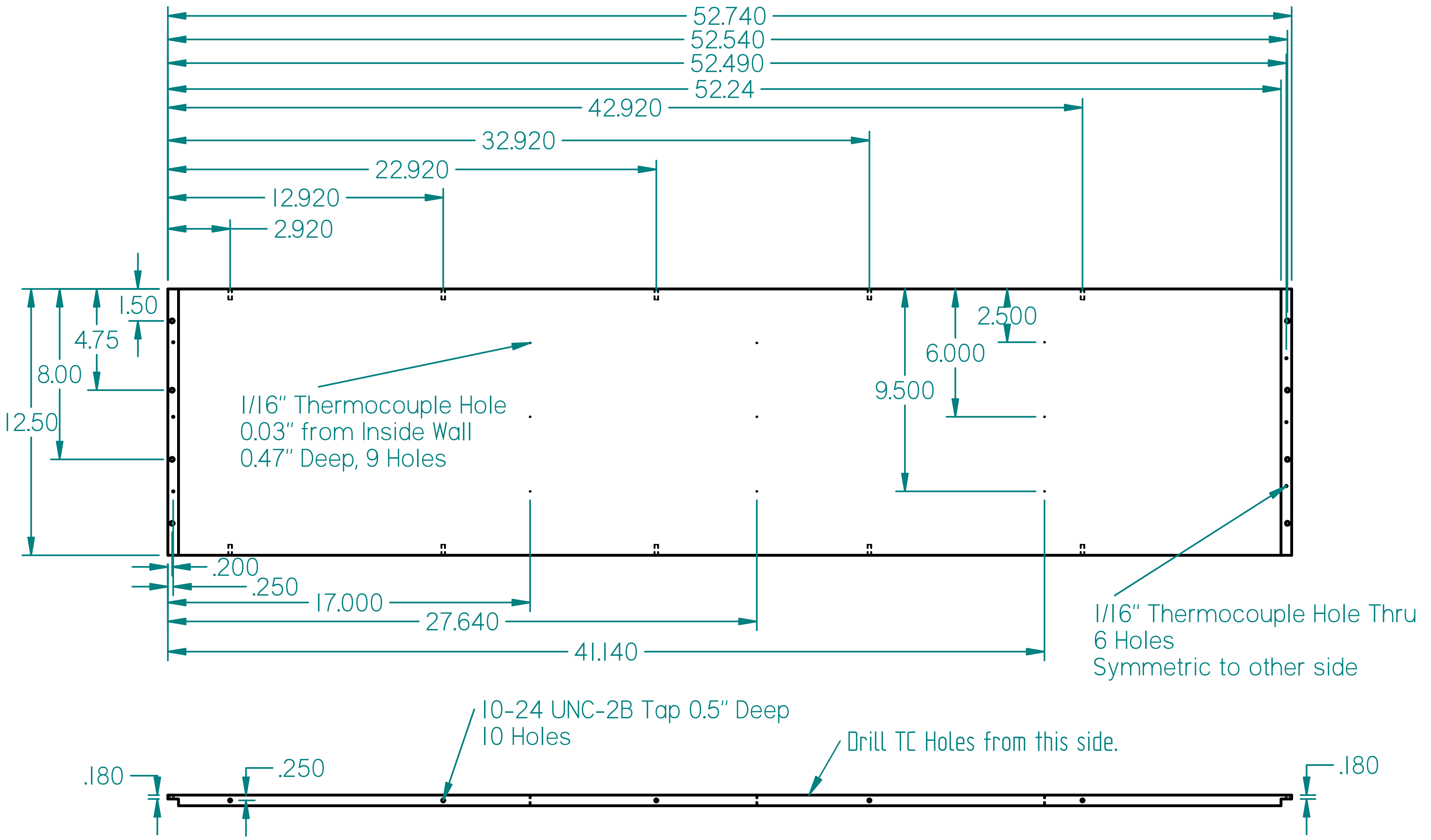

1/16" Thermocouple Hole
0.03" from Inside Wall
0.47" Deep, 9 Holes

1/16" Thermocouple Hole Thru
6 Holes
Symmetric to other side

10-24 UNC-2B Tap 0.5" Deep
10 Holes

Drill TC Holes from this side.

	NAME	DATE
DRAWN	Jeff_N7	03/21/13
CHECKED		
ENG APPR		
MGR APPR		

UNLESS OTHERWISE SPECIFIED
DIMENSIONS ARE IN INCHES
ANGLES ±X.X°
2 PL ±X.XX 3 PL ±X.XXX

Top Plate Section 2

TITLE
Top Section 2

SIZE	DWG NO	REV
A4		

FILE NAME: Top Mark 2 section 2.dft

SCALE:	WEIGHT:	SHEET 1 OF 1

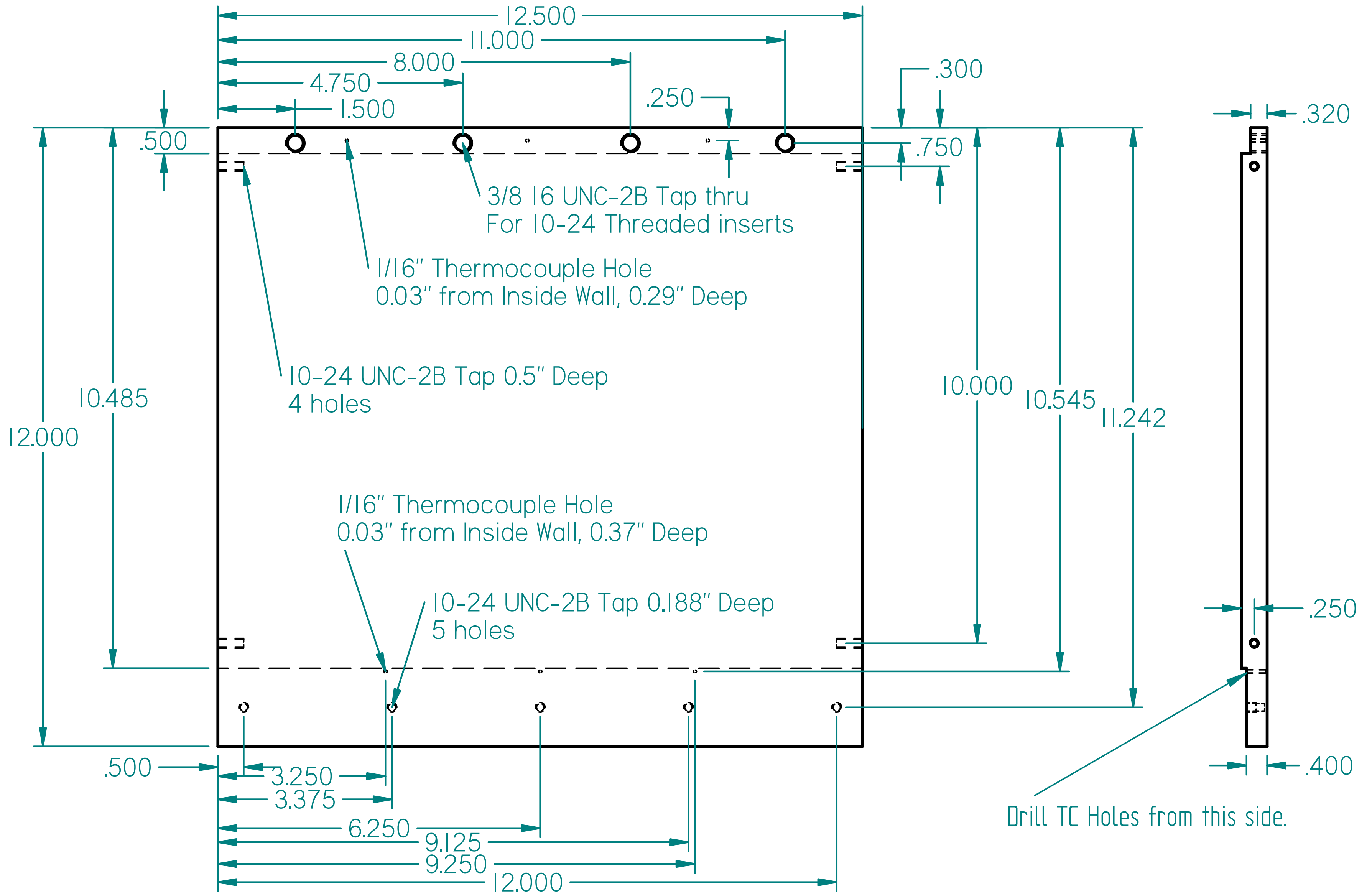

	NAME	DATE
DRAWN	Jeff_N7	03/21/13
CHECKED		
ENG APPR		
MGR APPR		

UNLESS OTHERWISE SPECIFIED
DIMENSIONS ARE IN INCHES
ANGLES ±X.X°
2 PL ±X.XX 3 PL ±X.XXX

Top Plate Section 3

TITLE
Top Section 3

SIZE A4
DWG NO
REV

FILE NAME: Top Mark 2 section 3b.dft

SCALE:
WEIGHT:
SHEET 1 OF 1

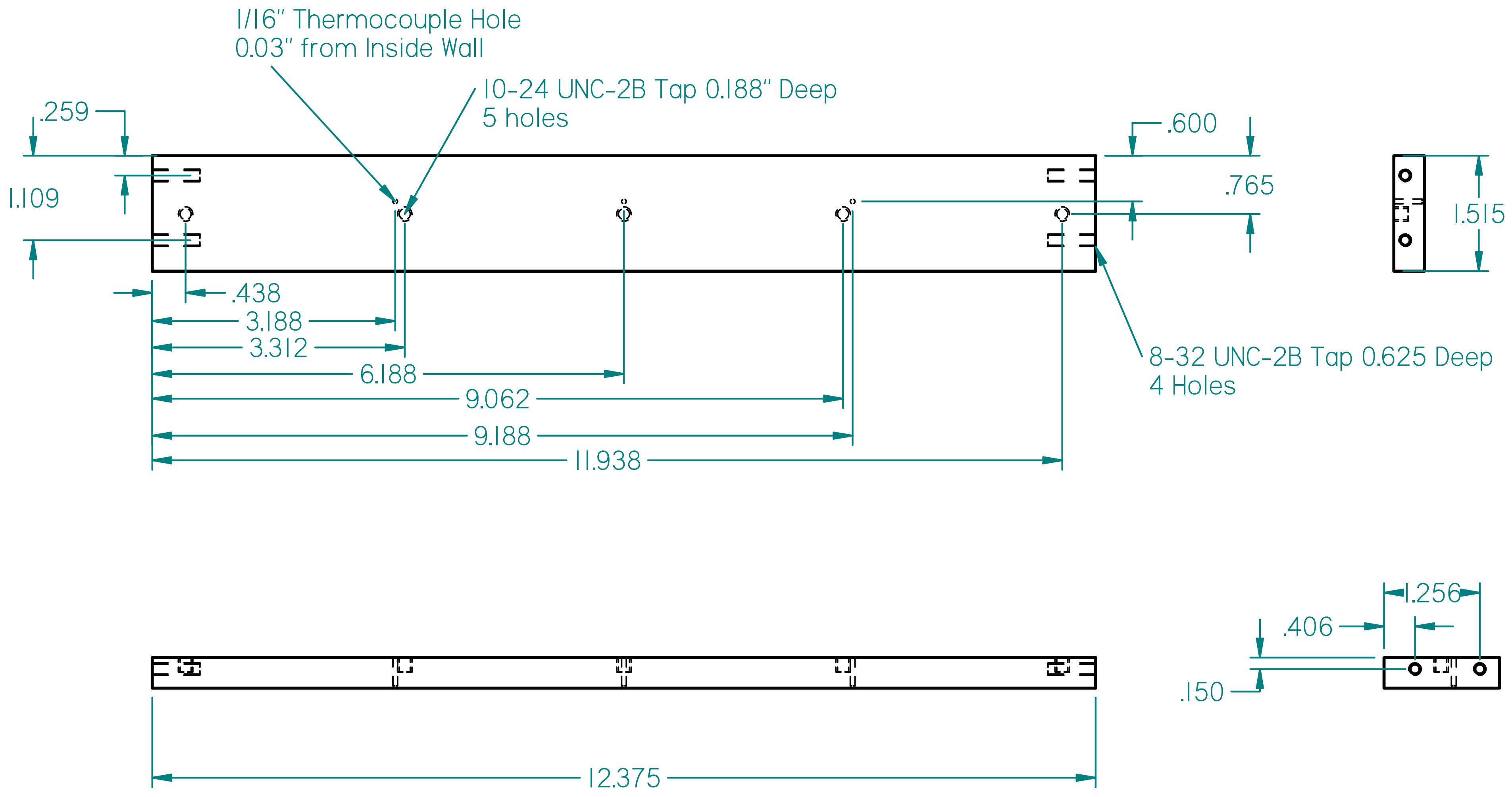

	NAME	DATE
DRAWN	Jeff_N7	03/21/13
CHECKED		
ENG APPR		
MGR APPR		

UNLESS OTHERWISE SPECIFIED
DIMENSIONS ARE IN INCHES
ANGLES ±X.X°
2 PL ±X.XX 3 PL ±X.XXX

Inlet Floor

TITLE
Inlet Floor

SIZE A4
DWG NO
REV

FILE NAME: Inlet Floor.dft

SCALE:
WEIGHT:
SHEET 1 OF 1

Appendix D

Custom Silicon Heater

The schematic of the heater from Tempco Electric Heater Corporation. Each heater cost \$158.90 and one time charge of \$60.00 to setup the manufacturing. The heaters have Teflon leads of 24 inches. The heaters have a capacity of 580 Watts and 60 Volts. Failure temperature is above 260°C, but continuous use should stay below 200°C.

NO.	REVISION	DATE	BY

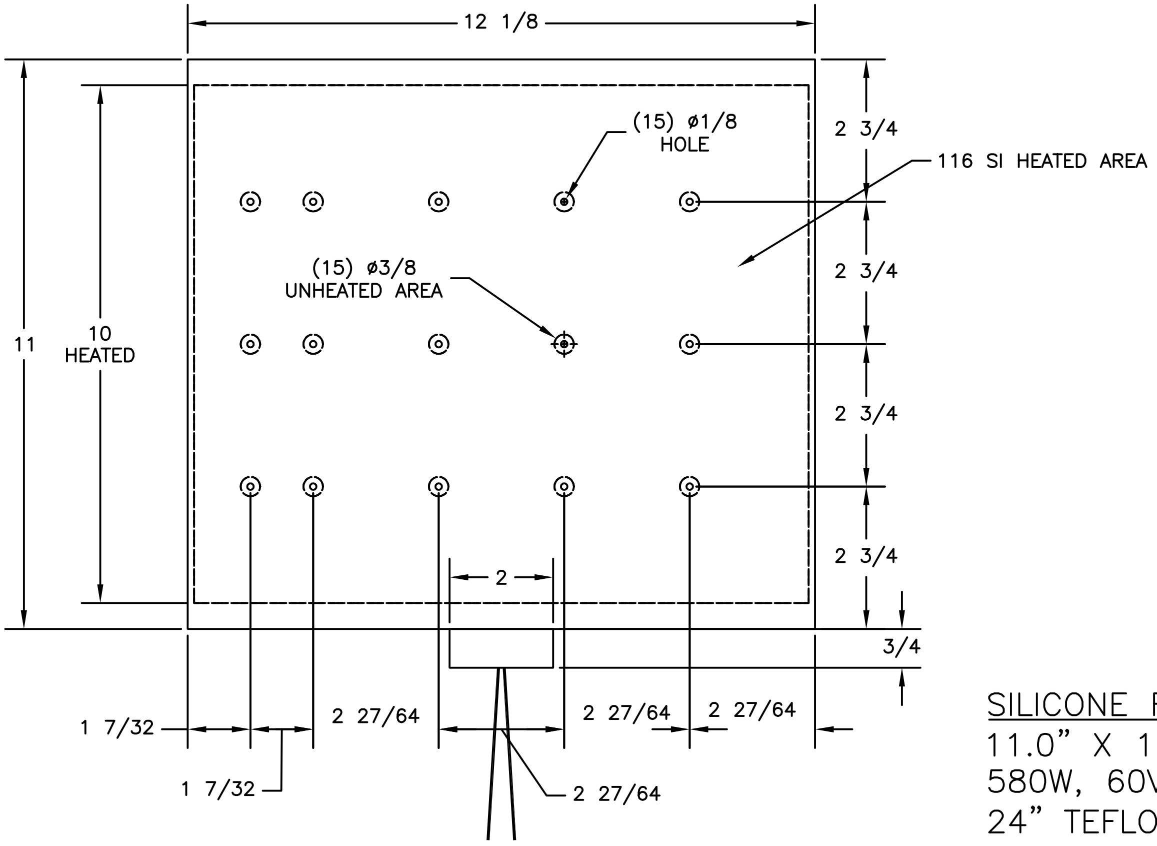

DRAWING APPROVED
BY:
DATE:

SILICONE RUBBER SURFACE HEATER
11.0" X 12.125"
580W, 60V
24" TEFLON LEADS
(15) HOLES 1/8" DIA
LEAD EXIT TAB 7/8" X 2"
1/2" UNHEATED MARGINS

ITEM	PART NO.	REQD	DESCRIPTION

TOLERANCES
UNLESS OTHERWISE
SPECIFIED
FRACTIONS ± 1/64
DECIMALS .XX ± .010
.XXX ± .005
ANGLES ± 1°
SURFACE FINISH √

Tempco Electric Heater Corporation
607 N. Central Ave.
Wood Dale, IL. 60191-1452 U.S.A.
Phone: (630) 350-2252 Fax: (630) 350-1210
Email: info@tempco.com

SCALE:	DATE:	DRAWN BY:	CHECKED:	APPROVED:
NTS	8/13/10	BPM		

CUSTOMER:

TITLE:
SILICONE RUBBER HEATER

DRAWING NUMBER:
SHS01814

Appendix E

Inlet Thermocouple Positions

The positions of the inlet thermocouples are shown in Fig. E.1. North is up in the figure and the thermocouples are numbered as in the Master .vi.

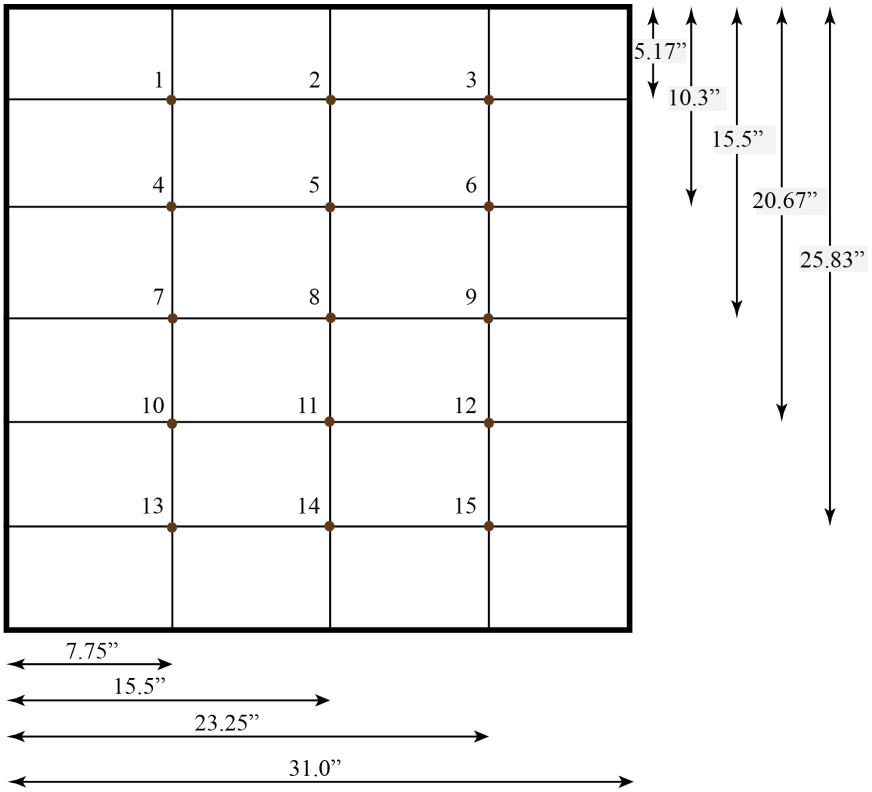

Fig. E.1: A sketch showing the positions of the inlet thermocouples. With the test section in the buoyancy aided orientation (inlet down), up in the image is north.

Appendix F

Boundary Conditions Statistics

```
clear all; close all; clc;format long;
%% Shaun Harris wrote this code Dec. 19, 2013
% email: shaun.r.harris@gmail.com
% feel free to contact if you have many questions

%% User Input
% put a 0 if you have 6 .csv files in one folder for your case or
% put a 1 if you have 5 temperature files in one folder and the heat flux
Filetype=input(['Put a 0 if you have all 6 .csv files in one folder \n'...
    ' Put a 1 if you have 5 temperature files in one spot and the heat'...
    ' flux files in another \n']);
%% if 0... input after running code is a 0
% 5 temperature .csv files under one folder and flux .csv files somewhere else
% Selecting files:  This program will ask you to select 2 seperate folders
%
% First folder:  Select the folder that is above a series of folders  that
% contain the 5 temperature .csv files
% Should be named HeatedWallTemp.csv, InletTemp.csv, RightWallTemp.csv,
% LeftWallTemp.csv and TopWallTemp.csv
%
% Second folder:  Select a folder that is above a series of .csv heat flux
% files that you want the stats for.  Make sure no other .csv files are in
% there
%
%% if 1... input after running code is a 1
% 6 .csv files in the same folder
% This code will ask you to select one folder.  Select the folder that is
```

```
% above a series of folders  that contain the 6 .csv files HeatedWallTemp.csv,
% InletTemp.csv, and etc. in each of the folders.  Make sure no other folders
% are in the folder.

%% After running code.  The variables can be identified
% HW_Mean_Temp is the heated wall average temperatures at each of the
% positions x y and z of multiple laser positions
% HW_SD is the heated wall standard deviation at each of the positions x y
% and z of multiple laser positions
% HW_PU is the heated wall precision uncertainty at each of the positions x
% y and z of multiple laser positions...v is used for the precision
% uncertainty claculation
%% Select files
% This section will bring in the all the temp data into your workspace
tempName={'\HeatedWallTemp.csv';'\InletTemp.csv';'\LeftWallTemp.csv';...
    '\RightWallTemp.csv';'\TopWallTemp.csv'};% Specific Temp file names
sprintf('%s','          Select the case you want to use')
if Filetype
    folder=uigetdir('', ...
        'Select Temperature .csv folder above the series of folders they are in');
    % find folder that contains all different positions
    dirListing=dir(folder); % array of all the names of the files in the folder
    FlxName=uigetdir(folder,'Select Heat Flux .csv folder for the case');
    %find folder that contains the flux files
    dirListingFlux=dir(fullfile(FlxName,'*csv'));
    % cell array of all names of the flux files in the folder
elseif ~Filetype
    tempName={'\HeatedWallTemp.csv';'\InletTemp.csv';'\LeftWallTemp.csv';...
        '\RightWallTemp.csv';'\TopWallTemp.csv'};% Specific Temp file names
    flxName={'\HeatFlux.csv'};
    folder=uigetdir;  % find folder that contains all different positions
    dirListing=dir(folder); %array of all the names of the files in the folder
    dirListingFlux=dirListing;
    FlxName=folder;
else
```

```
    sprintf('%s',['You need to read the introduction for this '
    'code and input a 1 or 0 for the Filetype'])
end
tic
% initialize a few arrays
b=0;
for d=3:length(dirListing)
    if dirListing(d).isdir
        b=b+1;
    end
end
c=0;
if Filetype
    for d=1:length(dirListingFlux)
        if ~dirListingFlux(d).isdir
            c=c+1;
        end
    end
else
    for d=3:length(dirListingFlux)
        if ~dirListingFlux(d).isdir
            c=c+1;
        end
    end
end
fluxName=cell(1,c);
M_flux=cell(1,c);
fileName=cell(5,b);
M_temp=cell(5,b);
%% loop through files and open and save in workspace as
if Filetype
    % corresponding fileName and M_temp arrays
    j=1;
    k=1;
    for d=3:b+2
```

```
        if dirListing(d).isdir % if file  in selected file is a folder.
            % If it is then run if statement
            for i=1:5
                fileName(i,k)={strcat(fullfile(folder,...
                    dirListing(d).name),tempName(i))};
        % full file name for each of the temp/flux files 2 below selected file
                [Num]=csvread(fileName{i,k}{1,1},1,0);
                M_temp{i,k}=Num;
                j=j+1;
            end
            k=k+1;
        else
            k=k+0;
        end
    end
    How_Many_Folders_Opened=k-1; % show how many folders in the selected file
    How_Many_Data_Temp_Sets=j-1;  % show how many temperature files you've opened

    % loop through for flux files
    k=1;
    for d=1:c
        if ~dirListingFlux(d).isdir % if file in selected folder is a .csv file
            fluxName(1,k)={fullfile(FlxName,dirListingFlux(d).name)};% for flux
            [Numb]=csvread(fluxName{1,k},0,0);
            M_flux{1,k}=Numb;
            k=k+1;
        end
    end
    How_Many_Flux_Files_Opened=k-1;
    clear j i k d Num ans Numb;  % clear extra variables
elseif ~Filetype
    j=1;
    k=1;
    for d=3:b+2
        if dirListing(d).isdir % if file  in selected file is a folder.
```

```
            %If it is then run if statement
            fluxName(1,k)={strcat(fullfile(folder,dirListing(d).name),...
                flxName(1))};% for flux
            [Numb]=csvread(fluxName{1,k}{1,1},0,0);
            M_flux{1,k}=Numb;
            for i=1:5
                fileName(i,k)={strcat(fullfile(folder,...
                    dirListing(d).name),tempName(i))};
           % full file name for each of the temp/flux files 2 below selected file
                [Num]=csvread(fileName{i,k}{1,1},1,0);
                M_temp{i,k}=Num;
                j=j+1;
            end
            k=k+1;
        else
        end
    end
    How_Many_Folders_Opened=k-1; % show how many folders in the selected file
    How_Many_Data_Temp_Sets=j-1;  % show how many temperature files you've opened
    clear j i d Num ans Numb;  % clear extra variables
else
    sprintf('%s','Seriously.... read the introduction')
end
%% Computing Temp Data next 3 sections also
% Mean temperature/Standard Deviation/Precision Uncertainty .csv files
[~,p]=size(M_temp); % size of array of temp files
[~,r]=size(M_flux); % size of array of flux files
% average temperature x y z temperature
[m,~]=size(M_temp{1,1});  % sizes of all walls
[m2,~]=size(M_temp{2,1});
[m3,~]=size(M_temp{3,1});
[m4,~]=size(M_temp{4,1});
[m5,~]=size(M_temp{5,1});
[~,n2]=size(M_flux{1,1}); % size of flux file
```

```
% initialize a few more arrays
HW_temp=zeros(length(1:m),length(1:p));
I_temp=zeros(length(1:m2),length(1:p));
LW_temp=zeros(length(1:m3),length(1:p));
RW_temp=zeros(length(1:m4),length(1:p));
TW_temp=zeros(length(1:m5),length(1:p));
HF=zeros(length(1:r),length(1:n2));
for j=1:p %loop for matrices for each wall temperatures cooresponding to positions
    HW_temp(1:m,j)=M_temp{1,j}(:,4);
    I_temp(1:m2,j)=M_temp{2,j}(:,4);
    LW_temp(1:m3,j)=M_temp{3,j}(:,4);
    RW_temp(1:m4,j)=M_temp{4,j}(:,4);
    TW_temp(1:m5,j)=M_temp{5,j}(:,4);
end
clear j;
for j=1:r
    HF(j,1:n2)=M_flux{1,j}(1,:); %and flux
end
%% average value of each wall and flux
HW_Mean_Temp=mean(HW_temp,2);
I_Mean_Temp=mean(I_temp,2);
LW_Mean_Temp=mean(LW_temp,2);
RW_Mean_Temp=mean(RW_temp,2);
TW_Mean_Temp=mean(TW_temp,2);
HF_MEAN=mean(HF);

% average temperature for each case for plots
HW_Mean_Case=mean(HW_temp);
I_Mean_Case=mean(I_temp);
LW_Mean_Case=mean(LW_temp);
RW_Mean_Case=mean(RW_temp);
TW_Mean_Case=mean(TW_temp);
%% standard deviation
HW_SD=(std(HW_temp,0,2));
I_SD=(std(I_temp,0,2));
```

```
LW_SD=(std(LW_temp,0,2));
RW_SD=(std(RW_temp,0,2));
TW_SD=(std(TW_temp,0,2));
HF_SD=std(HF);
%% precision uncertainty with 95% confidence interval = v*SD/sqrt(N)
mu=p-1; % mu is N-1
% table of mu values
v=[1:20;12.706 4.303 3.182 2.776 2.571 2.447 2.365 2.306 2.262 2.228 2.201...
    2.179 2.160 2.145 2.131 2.12 2.11 2.101 2.093 2.086]';
% precision uncertainty equations for each wall
HW_PU=v(mu,2)*HW_SD/sqrt(p);
I_PU=v(mu,2)*I_SD/sqrt(p);
LW_PU=v(mu,2)*LW_SD/sqrt(p);
RW_PU=v(mu,2)*RW_SD/sqrt(p);
TW_PU=v(mu,2)*TW_SD/sqrt(p);
HF_PU=v(mu,2)*HF_SD/sqrt(r);
clear j l m m2 m3 m4 m5 n n2 m6; % clear extra variables
%% Output
% write headers
% open files to write text headers to
fileIDHW=fopen(fullfile(folder,'Heated_Wall_MEAN_SD_PU.csv'),'w');
fileIDI=fopen(fullfile(folder,'Inlet_MEAN_SD_PU.csv'),'w');
fileIDLW=fopen(fullfile(folder,'Left_Wall_MEAN_SD_PU.csv'),'w');
fileIDRW=fopen(fullfile(folder,'Right_Wall_MEAN_SD_PU.csv'),'w');
fileIDTW=fopen(fullfile(folder,'Top_Wall_MEAN_SD_PU.csv'),'w');
fileIDHF=fopen(fullfile(FlxName,'HF_MEAN_SD_PU.txt'),'w');

% print headers
Head={'X','Y','Z','Tave','SD_T','P_T'};
Head2={'X','Flux','SD_Flux','P_Flux'};
fprintf(fileIDHW,'%s,%s,%s,%s,%s,%s\n',Head{1,:});
fprintf(fileIDI,'%s,%s,%s,%s,%s,%s\n',Head{1,:});
fprintf(fileIDLW,'%s,%s,%s,%s,%s,%s\n',Head{1,:});
fprintf(fileIDRW,'%s,%s,%s,%s,%s,%s\n',Head{1,:});
fprintf(fileIDTW,'%s,%s,%s,%s,%s,%s\n',Head{1,:});
```

```
fprintf(fileIDHF,'%s\t%s\t%s\t%s\n',Head2{1,:});
% close files
fclose('all');

% First get the master arrays
HW_Master_MeanTemp_SD_PU=[M_temp{1,1}(:,1),M_temp{1,1}(:,2),...
    M_temp{1,1}(:,3),HW_Mean_Temp,HW_SD,HW_PU];
I_Master_MeanTemp_SD_PU=[M_temp{2,1}(:,1),M_temp{2,1}(:,2),...
    M_temp{2,1}(:,3),I_Mean_Temp,I_SD,I_PU];
LW_Master_MeanTemp_SD_PU=[M_temp{3,1}(:,1),M_temp{3,1}(:,2),...
    M_temp{3,1}(:,3),LW_Mean_Temp,LW_SD,LW_PU];
RW_Master_MeanTemp_SD_PU=[M_temp{4,1}(:,1),M_temp{4,1}(:,2),...
    M_temp{4,1}(:,3),RW_Mean_Temp,RW_SD,RW_PU];
TW_Master_MeanTemp_SD_PU=[M_temp{5,1}(:,1),M_temp{5,1}(:,2),...
    M_temp{5,1}(:,3),TW_Mean_Temp,TW_SD,TW_PU];
HF_Master_MeanTemp_SD_PU=[.1617,.7777,1.3936;HF_MEAN;HF_SD;HF_PU]';
% includes x coordinates for heat flux sensors
% then write them to files
dlmwrite(fullfile(folder,'Heated_Wall_MEAN_SD_PU.csv'),HW_Master_MeanTemp_SD_PU,...
    '-append','precision',7); % for heated Wall
dlmwrite(fullfile(folder,'Inlet_MEAN_SD_PU.csv'),I_Master_MeanTemp_SD_PU,...
    '-append','precision',7);
dlmwrite(fullfile(folder,'Left_Wall_MEAN_SD_PU.csv'),LW_Master_MeanTemp_SD_PU,...
    '-append','precision',7);
dlmwrite(fullfile(folder,'Right_Wall_MEAN_SD_PU.csv'),RW_Master_MeanTemp_SD_PU,...
    '-append','precision',7);
dlmwrite(fullfile(folder,'Top_Wall_MEAN_SD_PU.csv'),TW_Master_MeanTemp_SD_PU,...
    '-append','precision',7);
dlmwrite(fullfile(FlxName,'HF_MEAN_SD_PU.txt'),HF_Master_MeanTemp_SD_PU,...
    'delimiter','\t','-append','precision',7);


%% Plot Average Temperature for each of the cases
% xaxis=case#   yaxis=Temp_average or HFSreading  Used to find outliers of cases
figure('Name','Heated Wall Average Temp For Each Case');
```

```
plot(1:p,HW_Mean_Case,'x','MarkerSize',12)
xlabel('Case Name'),ylabel('Average Temperature in Kelvin')
title('Heated Wall Average Temp')
set(gca,'XTick',1:p);set(gca,'XTickLabel',{dirListing(3:p+2).name},'FontSize',8)

figure('Name','Inlet Average Temp For Each Case');
plot(1:p,I_Mean_Case,'x','MarkerSize',12)
xlabel('Case Name'),ylabel('Average Temperature in Kelvin')
title('Inlet Average Temp')
set(gca,'XTick',1:p);set(gca,'XTickLabel',{dirListing(3:p+2).name},'FontSize',8)

figure('Name','Left Wall Average Temp For Each Case');
plot(1:p,LW_Mean_Case,'x','MarkerSize',12)
xlabel('Case Name'),ylabel('Average Temperature in Kelvin')
title('Left Wall Average Temp')
set(gca,'XTick',1:p);set(gca,'XTickLabel',{dirListing(3:p+2).name},'FontSize',8)

figure('Name','Right Wall Average Temp For Each Case');
plot(1:p,RW_Mean_Case,'x','MarkerSize',12)
xlabel('Case Name'),ylabel('Average Temperature in Kelvin')
title('Right Wall Average Temp')
set(gca,'XTick',1:p);set(gca,'XTickLabel',{dirListing(3:p+2).name},'FontSize',8)

figure('Name','Top Wall Average Temp For Each Case');
plot(1:p,TW_Mean_Case,'x','MarkerSize',12)
xlabel('Case Name'),ylabel('Average Temperature in Kelvin')
title('Top Wall Average Temp')
set(gca,'XTick',1:p);set(gca,'XTickLabel',{dirListing(3:p+2).name},'FontSize',8)

% Flux plot
figure('Name','Heat Flux Sensors per case')
plot(1:r,HF(:,1),'o','MarkerSize',12)
hold all
plot(1:r,HF(:,2),'d','MarkerSize',12)
plot(1:r,HF(:,3),'x','MarkerSize',12)
```

```
xlabel('Case Name'),ylabel('HFS reading in W / m^2'),title('Heat Flux Sensors')
legend('HFS 1','HFS 2','HFS 3')
if Filetype
    set(gca,'XTick',1:r);set(gca,'XTickLabel',{dirListingFlux(1:r).name},'FontSize',8)
else
    set(gca,'XTick',1:r);set(gca,'XTickLabel',{dirListingFlux(3:r+2).name},'FontSize',8)
end
%% clear extra variables
clear fileIDHW fileIDI fileIDLW fileIDRW fileIDTW  fileIDHF ans Head
clear Head2 p mu r FlxName HF_Mean HF_PU HF_SD HW_Mean_Temp HW_PU HW_SD
clear I_Mean_Temp I_PU I_SD LW_Mean_Temp LW_PU LW_SD RW_Mean_Temp RW_PU
clear RW_SD TW_Mean_Temp TW_PU TW_SD tempName b c k
toc
```

Appendix G

Inlet Analysis Code

```
clear all;  close all;  clc;

%% User input
proloc =23; % j—index for epsilon profile (increasing from top)
Serial='4.3'; %Name of the sheet to be used for the excel file for the Ustats
z = —0.0762;    % Z—coordinate in meters
% 3in=0.0762m, 5in=0.127m, 5.35in=0.13589m, 5.7in=0.14478m
Export = 0; % Export data in *.csv files? (1 for Yes/0 for No)
BL = 65;    % The number of data points from each edge to write

TrimTop = 1;
TrimBottom = 1;
TrimLeft = 1;
TrimRight = 1;

sprintf('%c','Select the MatLab Stats file')
[f1,p] = uigetfile('.mat');  % Ask user to choose velocity file
load(strcat(p,f1));
% sprintf('%c','Select the Tecplot file for the RMS (Standard Deviation):')

tic;
x=X'; x=x(:);
y=Y'; y=y(:);
vx1=v_ave'; vx1=vx1(:);vx1(isnan(vx1))=0;
vy1=u_ave'; vy1=vy1(:);vy1(isnan(vy1))=0;
vx2=uut'; vx2=sqrt(vx2(:));vx2(isnan(vx2))=0;
vy2=vvt'; vy2=sqrt(vy2(:));vy2(isnan(vy2))=0;
```

```
nu = 1.632E-5;  % kinematic viscosity at 1400 m elevation
[h,w]=size(u_ave);
%w=length(vx1);   % width
%h=length(vx2);   % height

%% Allocate and initialize
x_2D=zeros(w,h);
y_2D=zeros(w,h);
u=zeros(w,h);
v=zeros(w,h);
Uz=zeros(w,h);
Uxy=zeros(w,h);
SDx=zeros(w,h);
SDy=zeros(w,h);
SDz=zeros(w,h);
SDxy=zeros(w,h);

du_dx = zeros(w,1);
du_dy = zeros(w,1);
dv_dx = zeros(w,1);
dv_dy = zeros(w,1);

%% Run through data and sort
xcount=0;
for i=1:h
    for j=1:w
        xcount = xcount+1;
        x_2D(j,i)=x(xcount);
        y_2D(j,i)=y(xcount);
        u(j,i)=vx1(xcount)% u, v are in the x, y direction according to DaVis
        v(j,i)=vy1(xcount);
        Uz(j,i)=vx1(xcount);    % Assume w = v
        Uxy(j,i)=sqrt( vx1(xcount)^2 + vy1(xcount)^2 + vx1(xcount)^2 );
        SDx(j,i)=vx2(xcount);
```

```
        SDy(j,i)=vy2(xcount);
        SDz(j,i)=vx2(xcount);   % Assume SDz=SDy
        SDxy(j,i)=sqrt( vx2(xcount)^2 + vy2(xcount)^2 + vx2(xcount)^2 );
    end
end

%% Adaptive trimming to masked area
[imin,imax,jmin,jmax] = TrimToMask(v');

% iupper is the y index at the upper boundary (lowest index)
ilower = imin - TrimBottom;

% ilower is the y index at the lower boundary (highest index)
iupper = imax + TrimTop;

jlower = jmin + TrimLeft;
jupper = jmax - TrimRight;

xlower = x_2D(jlower,1);
xupper = x_2D(jupper,1);
ylower = y_2D(1,ilower);
yupper = y_2D(1,iupper);

xshift = x_2D(jlower,1);
x_2D = x_2D - xshift;   % Shift x_2D array so y=0 is at the left
xlower = xlower - xshift;
xupper = xupper - xshift;

%% Calculate epsilon based on gradients of fluctuating terms

% dx = abs( x_2D(1,1) - x_2D(2,1) );%Spacing between vectors in mm given by DaVis
dx = 305./(jupper-jlower+2);  % Spacing between vectors in mm given by geometry

for i=1:w
   du_dy(i) = 1000.*( SDx(i,proloc+1) - SDx(i,proloc-1) )/(2.*dx);
```

```
   dv_dy(i) = 1000.*( SDy(i,proloc+1) - SDy(i,proloc-1) )/(2.*dx);
end
for i=2:w-1
   du_dx(i) = 1000.*( SDx(i+1,proloc) - SDy(i-1,proloc) )/(2.*dx);
   dv_dx(i) = 1000.*( SDy(i+1,proloc) - SDy(i-1,proloc) )/(2.*dx);
end
du_dx(1) = 1000.*( -SDx(3,proloc) + ...
    4.*SDx(2,proloc) - 3.*SDx(1,proloc) )/(2.*dx);
du_dx(w) = 1000.*( 3.*SDx(w,proloc) - ...
    4.*SDx(w-1,proloc) + SDx(w-2,proloc) )/(2.*dx);
dv_dx(1) = 1000.*( -SDy(3,proloc) + ...
    4.*SDy(2,proloc) - 3.*SDy(1,proloc) )/(2.*dx);
dv_dx(w) = 1000.*( 3.*SDy(w,proloc) - ...
    4.*SDy(w-1,proloc) + SDy(w-2,proloc) )/(2.*dx);

% Sharp and Adrian's approximation for the epsilon profile
epsilon = nu*( 2.*du_dx.^2 + 2.*dv_dy.^2 + ...
    3.*du_dy.^2 + 3.*dv_dx.^2 + 2.*du_dy.*dv_dx );

%% Calculate the Turbulence Kinetic Energy
TKE = 0.5*SDxy(:,proloc)'.^2;

%% Transpose
x_2D=x_2D';
y_2D=y_2D';
u=u';
v=v';
Uxy=Uxy';
SDx=SDx';
SDy=SDy';
SDxy=SDxy';
TKE = TKE';

%% Plotting
% Plot contour of velocity magnitude
```

```
figure('Name','Velocity Magnitude'); contourf(x_2D,y_2D,Uxy,50,...
    'edgecolor','none'); hold on;
% quiver(x_2D,y_2D,u,v,3);
plot([x_2D(proloc,1) x_2D(proloc,w)],[y_2D(proloc,1) y_2D(proloc,w)],'r');
Uxymax = max(max(Uxy(iupper:ilower,jlower:jupper)));
Uxymin = min(min(Uxy(iupper:ilower,jlower:jupper)));
h1 = colorbar('EastOutside');
caxis([Uxymin Uxymax]); %shading interp
set(get(h1,'ylabel'),'String','Velocity (m/s)')
axis equal; axis([xlower,xupper,ylower,yupper])
xlabel('y (mm)');   ylabel('x (mm)');

% Plot contour of SD
figure('Name','Standard Deviation'); contourf(x_2D,y_2D,SDxy,50,...
    'edgecolor','none'); hold on;
% quiver(x_2D,y_2D,u,v,3);
plot([x_2D(proloc,1) x_2D(proloc,w)],[y_2D(proloc,1) y_2D(proloc,w)],'r');
SDxymax = max(max(SDxy(iupper:ilower,jlower:jupper)));
SDxymin = min(min(SDxy(iupper:ilower,jlower:jupper)));
h1 = colorbar('EastOutside');
caxis([SDxymin SDxymax]); %shading interp
set(get(h1,'ylabel'),'String','Standard Deviation (m/s)')
axis equal; axis([xlower,xupper,ylower,yupper])
xlabel('y (mm)');   ylabel('x (mm)');

% plot velocity magnitude across a profile
figure('Name','Velocity Magnitude across a profile');...
    plot(x_2D(proloc,:),Uxy(proloc,:));
axis([xlower,xupper,min(Uxy(proloc,jlower:jupper)),...
    max(Uxy(proloc,jlower:jupper))]);
xlabel('y (mm)');   ylabel('Velocity (m/s)');

% plot SD across a profile
figure('Name','Standard Deviation across a profile');
plot(x_2D(proloc,:),SDxy(proloc,:));
```

```
axis([xlower,xupper,min(SDxy(proloc,jlower:jupper)),...
    max(SDxy(proloc,jlower:jupper))]);
xlabel('y (mm)');   ylabel('Standard Deviation, \sigma (m/s)');

% plot TKE across a profile
figure('Name','TKE across a profile'); plot(x_2D(proloc,:),TKE);
axis([xlower,xupper,min(TKE(jlower:jupper)),max(TKE(jlower:jupper))]);
xlabel('y (mm)');   ylabel('TKE');

% plot epsilon across a profile
figure('Name','Epsilon across a profile'); plot(x_2D(proloc,:),epsilon(:));
axis([xlower,xupper,min(epsilon(jlower:jupper)),max(epsilon(jlower:jupper))]);
xlabel('y (mm)');   ylabel('\epsilon');

%% Write u, v, and w to *.csv file

if Export == 1
%write.xlsx file for variables on seperate sheets depending on ...
% what stats file you have chosen
%The Variables of v and u are switched.  DaVis program interprets the
%upward trajectory as v, and in our data we want it to be u.  That is why
%they are switched here.
xlswrite('ProfilesfromUstats.xlsx',{'Position' 'u_ave' 'Uu' 'uut'
    'Uuu_plus' 'v_ave' 'Uv' 'vvt' 'Uvv_plus' 'uvt' 'Uuv_plus' 'Position2'
    'u_ave2' 'Uu2' 'uut2' 'Uuu_plus2' 'v_ave2' 'Uv2' 'vvt2' 'Uvv_plus2'
    'uvt2' 'Uuv_plus2'},Serial,'A1:V1'), warning off MATLAB:xlswrite:AddSheet;

% M_Uxy = zeros(jupper-jlower+1,6);
M_Uxy = zeros(2*BL,6);
% M_Uxy(:,2) = 0.001*x_2D(proloc,jlower+1:jupper+1);
M_Uxy(1:BL,2) = 0.001*(dx:dx:BL*dx);  % Spread by geometry
M_Uxy(BL+1:2*BL,2) = 0.001*((jupper-jlower+2-BL)*dx:dx:305.-dx);
M_Uxy(:,3) = z;
M_Uxy(1:BL,4) = v(proloc,jlower:jlower+BL-1);%vfrom DaVis is actually u in Star
M_Uxy(BL+1:2*BL,4) = v(proloc,jupper-(BL-1):jupper);
```

```
M_Uxy(1:BL,5) = u(proloc,jlower:jlower+BL−1);%ufrom DaVis is actually v in Star
M_Uxy(BL+1:2*BL,5) = u(proloc,jupper−(BL−1):jupper);
M_Uxy(1:BL,6) = u(proloc,jlower:jlower+(BL−1));% we must assume that w=v
M_Uxy(BL+1:2*BL,6) = u(proloc,jupper−(BL−1):jupper);
dlmwrite('Inlet−uvw.csv',M_Uxy,'delimiter',',','precision',4,'−append')



%% Write k to *.csv file

K1 = zeros(2*BL,4);
K1(1:BL,2) = 0.001*(dx:dx:BL*dx);  % Spread by geometry
K1(BL+1:2*BL,2) = 0.001*((jupper−jlower+2−BL)*dx:dx:305.−dx);
K1(:,3) = z;
K1(1:BL,4) = TKE(jlower:jlower+(BL−1));
K1(BL+1:2*BL,4) = TKE(jupper−(BL−1):jupper);
dlmwrite('Inlet−k.csv',K1,'delimiter',',','precision',4,'−append')


%% Write epsilon to *.csv file

eps1 = zeros(2*BL,4);
eps1(1:BL,2) = 0.001*(dx:dx:BL*dx);  % Spread by geometry
eps1(BL+1:2*BL,2) = 0.001*((jupper−jlower+2−BL)*dx:dx:305.−dx);
eps1(:,3) = z;
eps1(1:BL,4) = epsilon(jlower:jlower+(BL−1));
eps1(BL+1:2*BL,4) = epsilon(jupper−(BL−1):jupper);
dlmwrite('Inlet−epsilon.csv',eps1,'delimiter',',','precision',4,'−append')

load(strcat(p,f1));
xlswrite('ProfilesfromUstats.xlsx',{'=OFFSET(A$5,5*(ROW()−2),0)'},...
    Serial,'L5:L5'), warning off MATLAB:xlswrite:AddSheet;

v_ave(isnan(v_ave))=0;
Uv(isnan(Uv))=0;
```

```
vvt(isnan(vvt))=0;
Uvv_plus(isnan(Uvv_plus))=0;

u_ave(isnan(u_ave))=0;
Uu(isnan(Uu))=0;
uut(isnan(uut))=0;
Uuu_plus(isnan(Uuu_plus))=0;

uv_ave(isnan(uv_ave))=0;
Uuv(isnan(Uuv))=0;
uvt(isnan(uvt))=0;
Uuv_plus(isnan(Uuv_plus))=0;

uvuvt(isnan(uvuvt))=0;
Uuvuv_plus(isnan(Uuvuv_plus))=0;

profile=[X(proloc,:)',v_ave(proloc,:)',Uv(proloc,:)',...
    vvt(proloc,:)',Uvv_plus(proloc,:)'];
profilev=[X(proloc,:)',u_ave(proloc,:)',Uu(proloc,:)',uut(proloc,:)',...
    Uuu_plus(proloc,:)'];
profileuv=[X(proloc,:)',uv_ave(proloc,:)',Uuv(proloc,:)',...
    uvt(proloc,:)',Uuv_plus(proloc,:)'];
profilemag=[X(proloc,:)',uv_ave(proloc,:)',Uuv(proloc,:)',...
    uvuvt(proloc,:)',Uuvuv_plus(proloc,:)'];
profilewhole=[X(proloc,:)',v_ave(proloc,:)',Uv(proloc,:)',...
    vvt(proloc,:)',Uvv_plus(proloc,:)',u_ave(proloc,:)',Uu(proloc,:)',...
    uut(proloc,:)',Uuu_plus(proloc,:)',uvt(proloc,:)',Uuv_plus(proloc,:)'];

xlswrite('ProfilesfromUstats.xlsx',profilewhole,Serial,'A2:K173'), ...
    warning off MATLAB:xlswrite:AddSheet;
end
toc;
```

Appendix H

Interpolator Code for StarCCM+

```
% Code to interpolate the PIV data to a fine grid for input to Star—CCM+

close all; clear all; clc
tic;
%% Read in the files to be interpolated.
%  Open the velocity, epsilon, and k files
sprintf('%c','Select the .csv file for the average velocity:')
[f1,p] = uigetfile('.csv');  % Ask user to choose velocity file
[data]=xlsread([p,f1]);
x_o=data(:,1);  y_o=data(:,2);  z_o=data(:,3);
u_o=data(:,4);  v_o=data(:,5);  w_o=data(:,6);

sprintf('%c','Select the .csv file for the epsilon:')
[f1,p] = uigetfile('.csv');  % Ask user to choose velocity file
[epsdata]=xlsread([p,f1]);
eps_o=epsdata(:,4);

sprintf('%c','Select the .csv file for the k:')
[f1,p] = uigetfile('.csv');  % Ask user to choose velocity file
[kdata]=xlsread([p,f1]);
k_o=kdata(:,4);

values=1; i=1;
while y_o(i)<y_o(i+1)
    values=values+1;
    i=i+1;
end
```

```
%%
originalsize=size(y_o);
y_1=zeros(values+2,1);
y_1(2:values+1)=y_o(1:values);
y_1(values+2)=0.3048;

z_1=zeros(values+2,1);
z_1(1:values)=z_o(values+1:values*2);
z_1(values+2)=0.1524;
z_1(values+1)=-0.1524;

data_1=zeros(originalsize+(values*4)+8,6);
epsdata2=zeros(originalsize+(values*4)+8,4);
kdata2=zeros(originalsize+(values*4)+8,4);

data_1(1:originalsize,:)=data;
epsdata2(1:originalsize,:)=epsdata;
kdata2(1:originalsize,:)=kdata;

count=0;
for i=originalsize+1:values+2+originalsize
    count=count+1;
    data_1(i,1)=0;
    data_1(i,2)=y_1(count);
    data_1(i,3)=-0.1524;
    data_1(i,4)=0;
    data_1(i,5)=0;
    data_1(i,6)=0;
%     epsdata2(i,1)=0;
%     epsdata2(i,2)=y_1(count);
%     epsdata2(i,3)=-0.1524;
%     epsdata2(i,4)=0;
    kdata2(i,1)=0;
    kdata2(i,2)=y_1(count);
```

```
    kdata2(i,3)=-0.1524;
    kdata2(i,4)=0;
end
count=0;
for i=originalsize+values+3:(values*2)+4+originalsize
    count=count+1;
    data_1(i,1)=0;
    data_1(i,2)=y_1(count);
    data_1(i,3)=0.1524;
    data_1(i,4)=0;
    data_1(i,5)=0;
    data_1(i,6)=0;
%     epsdata2(i,1)=0;
%     epsdata2(i,2)=y_1(count);
%     epsdata2(i,3)=0.1524;
%     epsdata2(i,4)=0;
    kdata2(i,1)=0;
    kdata2(i,2)=y_1(count);
    kdata2(i,3)=0.1524;
    kdata2(i,4)=0;
end
count=0;
for i=originalsize+(values*2)+5:(values*3)+6+originalsize
    count=count+1;
    data_1(i,1)=0;
    data_1(i,2)=0;
    data_1(i,3)=z_1(count);
    data_1(i,4)=0;
    data_1(i,5)=0;
    data_1(i,6)=0;
%     epsdata2(i,1)=0;
%     epsdata2(i,2)=0;
%     epsdata2(i,3)=z_1(count);
%     epsdata2(i,4)=0;
    kdata2(i,1)=0;
```

```
    kdata2(i,2)=0;
    kdata2(i,3)=z_1(count);
    kdata2(i,4)=0;
end
count=0;
for i=originalsize+(values*3)+7:(values*4)+8+originalsize
    count=count+1;
    data_1(i,1)=0;
    data_1(i,2)=0.3048;
    data_1(i,3)=z_1(count);
    data_1(i,4)=0;
    data_1(i,5)=0;
    data_1(i,6)=0;
%     epsdata2(i,1)=0;
%     epsdata2(i,2)=0;
%     epsdata2(i,3)=z_1(count);
%     epsdata2(i,4)=0;
    kdata2(i,1)=0;
    kdata2(i,2)=0;
    kdata2(i,3)=z_1(count);
    kdata2(i,4)=0;
end

%% Define the Fine Grid
% yp=[0.0018:0.0002:0.3032]';
y=y_1;%[0.00:0.0002:0.3048]';
% zp=[-0.1507:0.0002:0.1507]';
number=size(y,1);
z=[-0.1524:((0.1524*2)/(number-1)):0.1524]';


%% Interpolate the data to a fine grid
Fu = TriScatteredInterp(data_1(:,3),data_1(:,2),data_1(:,4));
[qx,qy] = meshgrid(z,y);
u = Fu(qx,qy);
```

```
Fv = TriScatteredInterp(data_1(:,3),data_1(:,2),data_1(:,5));
[qx,qy] = meshgrid(z,y);
v = Fv(qx,qy);
figure
contourf(v)
title('v')

Fw = TriScatteredInterp(data_1(:,3),data_1(:,2),data_1(:,6));
[qx,qy] = meshgrid(z,y);
w = Fw(qx,qy);

Feps = TriScatteredInterp(epsdata2(:,3),epsdata2(:,2),epsdata2(:,4));
[qx,qy] = meshgrid(z(2:131),y_o(1:130));
eps1 = Feps(qx,qy);
eps1(isnan(eps1))=0;
figure
contourf(eps1)
title('epsilon')

Fk = TriScatteredInterp(kdata2(:,3),kdata2(:,2),kdata2(:,4));
[qx,qy] = meshgrid(z,y);
k1 = Fk(qx,qy);
k1(isnan(k1))=0;
figure
contourf(k1)
title('TKE')
%% Now we want to make the left and right side the same as the top side
eps=eps1;
eps(:,1:70)=eps1(:,1:70)+flipdim(eps1(end-69:end,:)',2);
eps(:,end-69:end)=eps1(:,end-69:end)+eps1(end-69:end,:)';
figure
contourf(eps)
title('epsilon with left and right sides same as top');
```

```
k=k1;
k(:,1:70)=k1(:,1:70)+flipdim(k1(end-69:end,:)',2);
k(:,end-69:end)=k1(:,end-69:end)+k1(end-69:end,:)';
figure
contourf(k)
title('TKE with left and right sides same as top');

%% Write the files
Vel=zeros(number*number,6);
epsilon=zeros(number*number,4);
turb=zeros(number*number,4);
omega1=zeros(number*number,4);
omega2=zeros(number*number,4);

count=0;
for i=1:number
    for j=1:number
        count=count+1;
        Vel(count,:)=[0,y(i),z(j),u(i,j),v(i,j),w(i,j)];
%         epsilon(count,:)=[0,y(i),z(j),eps(i,j)];
        turb(count,:)=[0,y(i),z(j),k(i,j)];
    end
end
count=0;
for i=1:number-2
    for j=1:number-2
        count=count+1;
%         Vel(count,:)=[0,y(i),z(j),u(i,j),v(i,j),w(i,j)];
        epsilon(count,:)=[0,y(i),z(j),eps(i,j)];
%         turb(count,:)=[0,y(i),z(j),k(i,j)];
    end
end

small=min(Vel);
smalleps=min(epsilon);
```

```
smallk=min(turb);

Vel(isnan(Vel))=small(6);
epsilon(isnan(epsilon))=smalleps(4);
turb(isnan(turb))=smallk(4);

% Create Omega for Transition Model
omega1(:,1:3) = epsilon(:,1:3);
omega2(:,1:3) = epsilon(:,1:3);

B = 0.09;                          % Cmu parameter found in turbulence solvers
for i = 1:length(epsilon(:,1))
    omega1(i,4) = epsilon(i,4)/turb(i,4);
    omega2(i,4) = epsilon(i,4)/(B*turb(i,4));
end

% Write the velocity inlet file
header=['X,Y,Z,u,v,w,'];
outid = fopen('Inlet—uvw—interp.csv', 'w+');
fprintf(outid, '%s', header);
fprintf(outid, '\n');
fclose(outid);

dlmwrite('Inlet—uvw—interp.csv',Vel,'delimiter',',','precision',4,'—append')

% Write the epsilon file for the inlet
header=['X,Y,Z,epsilon,'];
outid2 = fopen('Inlet—epsilon—interp.csv', 'w+');
fprintf(outid2, '%s', header);
fprintf(outid2, '\n');
fclose(outid2);

dlmwrite('Inlet—epsilon—interp.csv',epsilon,'delimiter',',','precision',4,'—append')

% Write the k file for the inlet
```

```
header=['X,Y,Z,k,'];
outid3 = fopen('Inlet-k-interp.csv', 'w+');
fprintf(outid3, '%s', header);
fprintf(outid3, '\n');
fclose(outid3);

dlmwrite('Inlet-k-interp.csv',turb,'delimiter',',','precision',4,'-append')

% Write the omega files for the inlet
header=['X,Y,Z,w,'];
outid4 = fopen('Inlet-w1-interp.csv', 'w+');     % Omega 1 formulation (w = e/k)
fprintf(outid4, '%s', header);
fprintf(outid4, '\n');
fclose(outid4);

dlmwrite('Inlet-w1-interp.csv',omega1,'delimiter',',','precision',4,'-append')

outid5 = fopen('Inlet-w2-interp.csv', 'w+');      % Omega 2 formulation (w = e/Bk)
fprintf(outid5, '%s', header);
fprintf(outid5, '\n');
fclose(outid5);

dlmwrite('Inlet-w2-interp.csv',omega2,'delimiter',',','precision',4,'-append')
toc;



% Code to interpolate the Temperature data to a fine grid for input to Star-CCM+


close all; clear all; clc;
tic;
%% Read in the files to be interpolated.
%  Open the velocity, epsilon, and k files
sprintf('%c','Select the .csv file for the inlet temperature:')
[f1,p] = uigetfile('.csv');  % Ask user to choose velocity file
[inlet]=xlsread([p,f1]);
```

```
inletT=inlet(:,4);

inletz=inlet(:,3);

inlety=inlet(:,2);


sprintf('%c','Select the .csv file for the plate temperature:')

[f1,p] = uigetfile('.csv');  % Ask user to choose velocity file

[plate]=xlsread([p,f1]);

plateT=plate(:,4);

platex=plate(:,1);

platez=plate(:,3);


%% Define the Fine Grid for the plate

platex_fine=[0:0.001:1.859]';

platez_fine=[-0.1507:0.001:0.1507]';


% and for the inlet temperature

inlety_fine=[0.076:0.0005:.229]';

inletz_fine=[-0.102:0.0005:0.102]';


%% Interpolate the data to a fine grid

Fu = TriScatteredInterp(inlety,inletz,inletT);

[qx,qy] = meshgrid(inlety_fine,inletz_fine);

InletT = Fu(qx,qy);


Fv = TriScatteredInterp(platex,platez,plateT);

[qx,qy] = meshgrid(platex_fine,platez_fine);

PlateT = Fv(qx,qy);


%% Sort to write out the files


TempI=zeros(size(InletT,1)*size(InletT,2),4);

TempPlate=zeros(size(PlateT,1)*size(PlateT,2),4);


count=0;

for i=1:size(InletT,1)
```

```
    for j=1:size(InletT,2)
        count=count+1;
        TempI(count,:)=[0,inlety_fine(j),inletz_fine(i),InletT(i,j)];
    end
end

count=0;
for i=1:size(PlateT,1)
    for j=1:size(PlateT,2)
        count=count+1;
        TempPlate(count,:)=[platex_fine(j),0,platez_fine(i),PlateT(i,j)];
    end
end
smallTP=min(TempPlate);
TempPlate(isnan(TempPlate))=smallTP(4);

%% Write the inlet temperature file
header=['X,Y,Z,Temp,'];
outid = fopen('Inlet-Temp-interp.csv', 'w+');
fprintf(outid, '%s', header);
fprintf(outid, '\n');
fclose(outid);

dlmwrite('Inlet-Temp-interp.csv',TempI,'delimiter',',','precision',7,'-append')

header=['X,Y,Z,Temp,'];
outid = fopen('HeatedWall-Temp-interp.csv', 'w+');
fprintf(outid, '%s', header);
fprintf(outid, '\n');
fclose(outid);

dlmwrite('HeatedWall-Temp-interp.csv',TempPlate,'delimiter',',','precision',7,'-append')
toc;
```

Appendix I

Code to Compute Correlations and Momentum Thickness

```
%% Clear and close everything
clc; close all;

%  This program will let you select the plate temperature .csv file, then
%  it plots the temperature contour and provides the Forced and Mixed
%  correlations, given the inputs below.  The last part provides several
%  non-dimensional and dimensional parameters for the case.
%%
opposed = 0;  % If for an opposed case, opposed = 1
U   = 4.489; %m/s free stream 2.62  4.489
rho = 1.0128;
mu  = 1.8187*10^(-5);
nu = mu/rho;

u_data1 = data1(:,2);
x_data1 = data1(:,1);

u_data2 = data2(:,2);
x_data2 = data2(:,1);

u_data3 = data3(:,2);
x_data3 = data3(:,1);
%% Selecting the csv files
sprintf('%c','Select the Heated Plate Temp file')
[f0,p0] = uigetfile('*.csv','Select the csv file');

Ai=xlsread(strcat(p0,f0));
```

```
 xi=Ai(:,1);
 yi=Ai(:,3);
 ti=Ai(:,4);

%find unique x and y grid points
ai=sort(unique(xi(6:end)));
bi=sort(unique(yi(6:end)));
Ni=length(xi);

%initialize matrices
Ti=zeros(length(bi),length(ai));
Xi=zeros(length(bi),length(ai));
Yi=zeros(length(bi),length(ai));

%generate grid matrix
[Xi,Yi]=meshgrid(ai,bi);

y_dum=[-0.152;yi(1:5);0.152];
X=cat(2,zeros(7,1),Xi);
Y=cat(2,y_dum,Yi);

%generate variable matrices (nans where no data available)
for ni=1:Ni
    Ii=find(bi==yi(ni));
    Ji=find(ai==xi(ni));
    Ti(Ii,Ji) = ti(ni);
end
T = cat(2,[0;ti(1:5);0],Ti);
%%
%Plot Plate Temp
figure('Name','Plate Temp'); contourf(X,Y,T,200);colorbar; shading flat;...
    caxis([290 430]);xlabel('x [m]','FontName','Times New Roman');
ylabel('z [m]','FontName','Times New Roman');title('Plate Temp [K]');
axis image
filename=strcat(p0(end-2:end-1),'.jpg');
```

```
saveas(gcf,filename,'jpg')
%Save figure to be used in the movie later
% [I0,mapI0]=getframe(gcf);
%% Now plot the centerline temperature and correlations for the heat flux
T_center = T(4,:);

% Forced convection correlations
% from Kays and Crawford 12-18, turbulent flow
cp  = 1005;
Pr  = 0.7;
k   = 26.37*10^-3;

Gr_L = (9.81/295).*(T_center-295).*X(4,:).^3./(mu/rho)^2;
Ra_L = Pr*Gr_L;
Re_x = rho*U.*X(4,:)./mu;
St = (0.0287*Re_x.^(-0.2))'./(0.169*Re_x.^(-0.1)*(13.2*Pr-9.25)+0.85)';
h = rho*U*cp*St;
Nu_Kays = h.*X(4,:)'./k;
Flux_Kays = h.*(T_center'-(21+273));

% Incropera Nusselt number correlation
% Eqn 7.36, Nu for Turbulent flow over isothermal plate
Nu_x = 0.0296.*Re_x.^(4/5)*Pr^(1/3);
h_inc = Nu_x'.*k./X(4,:)';
Flux_Incropera = h_inc.*(T_center'-(21+273));

figure
plot(X(4,:),Flux_Kays); hold on;
plot(X(4,:),Flux_Incropera,'r'); hold on;

%% Compute the Mixed Correlations
%  Using the popular notion that Nu = Nu_f +- Nu_n

% Compute the natural convection correlation, 9.26 in Incropera
Nu_x_nat = (0.825+(0.387.*Ra_L.^(1/6))/((1+0.492/Pr)^(9/16))^(8/27)).^2;
```

```
% Compute the mixed convection Nusselt number by either adding (aided) or
%  subtracting (opposed) the natural and forced correlations

Nu_x_mixed = (Nu_x.^3 + Nu_x_nat.^3).^(1/3);
if opposed==1
    Nu_x_mixed = (Nu_x.^3 - Nu_x_nat.^3).^(1/3);
end

Nu_x_mixed2 = (Nu_Kays.^3 + Nu_x_nat'.^3).^(1/3);
if opposed==1
    Nu_x_mixed2 = (Nu_Kays.^3 - Nu_x_nat'.^3).^(1/3);
end

% Compute heat flux for mixed
Flux_mixed1 = (Nu_x_mixed'.*k./X(4,:)').*(T_center'-294);
Flux_mixed2 = (Nu_x_mixed2.*k./X(4,:)').*(T_center'-294);

plot(X(4,:),Flux_mixed1,'k'); hold on;
plot(X(4,:),Flux_mixed2,'g');
legend('Kays','Incropera','Incropera Mixed','Kays Mixed')

%% Compute the Case Dimensionless Parameters
[rte,index1]=min(abs(X(4,:)-.1617345));
X1 = X(4,index1);
[rte,index2]=min(abs(X(4,:)-.7776845));
X2 = X(4,index2);
[rte,index3]=min(abs(X(4,:)-1.3936345));
X3 = X(4,index3);

T1 = T_center(index1);
T2 = T_center(index2);
T3 = T_center(index3);

Re_Dh = rho*U*(0.3048)/mu;
```

```
Re_1  = rho*U*0.1617345/mu;
Re_2  = rho*U*0.7776845/mu;
Re_3  = rho*U*1.3936345/mu;

Gr_1 = 9.81/340*(T1-295)*0.1617345^3/nu^2;
Gr_2 = 9.81/340*(T2-295)*0.7776845^3/nu^2;
Gr_3 = 9.81/340*(T3-295)*1.3936345^3/nu^2;

delta2_1 = trapz(x_data1./1000,...
    (u_data1./U).*(1.-(u_data1./U)));
delta2_1b = 0.664*sqrt(nu*X1/U);
Re_delta2_1 = U*delta2_1/nu;

delta2_2 = trapz(x_data2./1000,...
    (u_data2./U).*(1.-u_data2./U));
delta2_2b = 0.664*sqrt(nu*X2/U);
Re_delta2_2 = U*delta2_2/nu;

delta2_3 = trapz(x_data3./1000,...
    (u_data3./U).*(1.-u_data3./U));
delta2_3b = 0.664*sqrt(nu*X3/U);
Re_delta2_3 = U*delta2_3/nu;
```

Appendix J

Shear Velocity Code to Compute u_τ

```
% Code to fit data to the Spaulding Profile and find u_tau

% Drag data into the workspace — A Ustats file will work best
u=data(:,2);
y=data(:,1); % in mm
opposed = 0; % opposed= 1 if the data is opposed, 0 if aided
if opposed == 1
    u = flipdim(u,1);
    y = flipdim(y,1);
end

rho = 1.0215;
mu  = 1.83∗10^(—5);
k=0.41;
B=5;
% nu=(1.773E—5);
nu = 1.79E—5;
P = 653.5; %torr
T = 273+23.6;  %K
phi=0.34; %Relative Humidity

utau=0.254;
uplus=u/utau;
yplus=0.001∗y∗utau/nu;
Spaul=uplus+exp(—k∗B)∗(exp(k∗uplus)—1—k∗uplus—(k∗uplus).^2/2—(k∗uplus).^3/6);

%% Compute the Spaulding Profile
```

```
points=80;
LowerPoint=10;

A0 = [0      % y0 in meters
    0.41     % kappa
    5        % B
    .2];     % u_tau

Alb = [-0.1 0.1 3 0];     % lower bound
Aub = [0.1 1 9 1];    % upper bound

for l=1:100 % Repeat least squares curve fit so bad initial guess is overcome
    % Fitting 4 constants ydata is u velocity, function yields y in Kendall
    % paper
    F = @(A,ydata)...
        A(1) + nu/A(4)*(ydata/A(4) + exp(-A(2)*A(3))*(exp(A(2)*ydata/A(4))...
        - 1 - A(2)*ydata/A(4)...
        - 0.5*(A(2)*ydata/A(4)).^2 - (A(2)*ydata/A(4)).^3/6. ));

    [A,resnorm] = lsqcurvefit(F,A0,u(LowerPoint:points),...
        0.001*y(LowerPoint:points),Alb,Aub)

%     % Fitting 2 constants
%     kappa = 0.41;
%     B = 5.0;
%
%     F = @(A,ydata)...
%         A(1) + nu/A(4)*(ydata/A(4) + exp(-kappa*B)*(exp(kappa*ydata/A(4))...
%         - 1 - kappa*ydata/A(4)...
%         - 0.5*(kappa*ydata/A(4)).^2 - (kappa*ydata/A(4)).^3/6. ));
%
%     [A,resnorm] = lsqcurvefit(F,A0,u(1:points),...
%         0.001*y(1:points),Alb,Aub)

    A0 = A;
```

```
end
%% Compute Uncertainty of the Wall Shear
[ShearUncertainty,nu] = ShearVelocityUncertaintyfunc(T,P,phi,y,u,data,opposed);
U_utau = mean(ShearUncertainty(10:end-10));
%% Non-dimensionalize experimental profile
yPlus = ( 0.001*y - A(1) )*A(4)/nu;  % Convert mm to m by *0.001
uPlus = u/A(4);

%% Spalding profile
yPlus_Spal = ( F(A,u) - A(1) )*A(4)/nu;

%% Law of the wall
uPlus_LofW = log( (0.001*y - A(1) )*A(4)/nu )/A(2) + A(3);

% Plot non-dimensional profiles
figure; semilogx(yPlus(LowerPoint:points), uPlus(LowerPoint:points), 'x');
 axis([1,max(yPlus),...
     0,max(uPlus)]);
xlabel('y^+');   ylabel('u^+');
hold on; semilogx(yPlus_Spal, uPlus,'r');
semilogx(yPlus(1:18), yPlus(1:18),'g');
semilogx(yPlus(10:end), uPlus_LofW(10:end), 'm');
% semilogx(Spaul, uPlus,'k');
legend('Experiments','Spalding','u^+ = y^+','Law of the Wall','Location','Best');

%% Now we want to confrim the linearity of the total shear stress, from Adrian 07

uv = data(:,10);
dudy = u(2:end);
for i=1:size(u,1)-1;
    dudy(i) = (u(i+1)-u(i))/(y(i+1)-y(i))*1000;
    tau(i) = -rho*uv(i) + mu*dudy(i);
end
% tau=tau';
tau_linefunc=fit(y(2:end),tau(1:end)','poly1');
```

```
tau_line=tau_linefunc(y);


figure
plot(y(2:end),tau'); hold on;
plot(y,-rho*uv,'k')
plot(y(2:end),mu*dudy,'r')
plot(y,tau_line,'g')
xlabel('y');    ylabel('\tau');
```

Appendix K

Copyright Permissions

Copyright permission from Engineering Laboratory Design, Inc. for use of Wind Tunnel Drawings in Appendix B. From email correspondence:

Hello Barton and Jared,

You may use the drawings that we furnished with the wind tunnel in your papers. Indicate that the images are "Used with permission" and credit Engineering Laboratory Design, Inc.

Thanks for requesting permission.

Regards,

Sig Anderson

Sigurd W. Anderson, President
Engineering Laboratory Design, Inc. 2021 South Highway
61 PO Box 278 Lake City, MN 55041 USA
mariner@eldinc.com
651-345-4515
800-795-8536
FAX 651-345-5095
www.eldinc.com

Vita

Jeff Harris

Education and Training

- Ph.D. Mechanical Engineering, *Utah State University, Logan, UT*, 2014
    - Dissertation: A Computational Fluid Dynamics Validation Experiment for Forced and Mixed Convection on a Vertical Heated Plate
    - Thermal/Fluids emphasis, 3.90 GPA
- M.S. Mechanical Engineering, *Utah State University, Logan, UT*, 2012
    - Topic: Relative Importance of Some Error Sources in Particle Image Velocimetry
    - Thermal/Fluids emphasis, 3.92 GPA
- B.S. Mechanical Engineering, *Utah State University, Logan, UT*, 2010
    - Aerospace emphasis, Math Minor, 3.86 GPA
- Modeling, Experimentation, and Validation School, *Idaho National Laboratory, Idaho Falls, ID*, 2010
    - Studied safety analysis, risk assessment, and validation techniques in nuclear science

Peer-Reviewed Papers and Presentations

- Harris, J., Lance, B., Smith, B. Experimental Validation Data for CFD of Forced Convection on a Vertical Flat Plate. *Journal of Fluids Engineering.* Submitted for review April 2014.

- Lance, B. and Harris, J. Mixed Convection Validation and Simulation, American Nuclear Society 2014 Student Conference, April 35, 2014, State College, PA.

- Harris, J., Lance, B., Smith, B. Design of Apparatus for Validation Experiments, ANS Annual Meeting, Atlanta, GA, 2013.

- Lance, B., Harris, J., et. al. Validation Study on Forced and Mixed Convection in the Rotatable Buoyancy Tunnel. ASME FEDSM, Incline Village, NV, 2013.

- Smith, B., Lance, B. Harris, J. Iverson, J. Spall, R. The RoBuT for CFD Validation of Natural, Mixed, and Forced Convection, ASME V&V Symposium, Las Vegas, NV, 2013.

- Harris, J., Lance, B., Smith, B., Spall, R. Transient Mixed Convection Validation Facility and Study, NURETH-15, Pisa, Italy, 2013.

- Harris, J., Lance, B., Iverson, J. Forced Convection Validation Experiment and Simulation. ANS Student Conference, Boston, MA, 2013 - awarded Best Overall Graduate Paper

- Harris, J., Wilson, B., Smith, B. Investigation of Relative Importance of Some Error Sources in Particle Image Velocimetry, ASME Fluids Engineering Summer Meeting, Puerto Rico, USA, 2012.

- Harris, J., Nani, D., Jones, K., Khodier, M., Smith, B. Investigation of the Uncertainty of a Validation Experiment due to Uncertainty in its Boundary Conditions, NURETH-14, 2011.

- Wilson, B., Smith, B., Spall, R., Harris, J. Validation of Unsteady CFD in a Confined Row of Cylinders, FEDSM2010-ICNMM2010, Proceedings of the ASME Fluids Engineering Conference, Montreal, Canada, 2010.

- Rational Radial Distortion Models of Camera Lenses with Analytical Solution for Distortion Correction, Lili Ma, YangQuan Chen, and Kevin L. Moore, *International Journal of Information Acquisition, Accepted.*

- A Small Mobile Robot for Security and Inspection Operations, N.S. Flann, K. L. Moore, and Lili Ma, *Control Engineering Practice*, vol. 10, pp. 1265-1270, 2002.

Non-Peer-Reviewed Papers and Presentations

- Harris, J., Lance, B., Smith, B. Experimental Validation of Simulations for Buoyancy Opposed Convection, APS Division of Fluid Dynamics Meeting, Pittsburgh, PA, 2013
- Harris, J., Lance, B. Design and Implementation of Simulation Validation Experiments for Passive Cooling Features in Nuclear Reactors. USU Graduate Research Symposium, Logan, UT, 2013 - Honorable Mention for Best Oral Presentation
- Wilson, B., Harris, J., Smith, B. Uncertainty in Velocity Fluctuations for Two-Component PIV Measurements, APS Division of Fluid Dynamics, Baltimore, Maryland, 2011.
- Wilson, B., Harris, J., Smith, B., Spall, R. E. Unsteady Validation Metrics for CFD in a Cylinder Array, Proceedings of the CFD4NRS, Washington D.C., USA, 2010.

Awards

- College of Engineering Graduate Researcher of the Year, 2014
- College of Engineering Outstanding Graduate Scholar, 2014
- Nuclear Regulatory Commission Fellowship Recipient, 2012
- Founding Vice-President of USU Student Section of the American Nuclear Society, 2012
- Graduate Teaching Assistant of the Year, 2011
- Outstanding Senior, Mechanical and Aerospace Engineering, 2010
- Nuclear Regulatory Commission Scholarship Recipient, 2009

- Tau Beta Pi Scholarship Recipient, 2009
- Academic Excellence Award, Mechanical and Aerospace Engineering, 2008
- USU Presidential Scholarship Recipient, 2004

Professional Activities

- Student Host GLOBAL 2013: International Nuclear Fuel Cycle Conference
- Reviewer American Society of Mechanical Engineers IMECE Conference, 2013
- Reviewer American Society of Mechanical Engineers HTFENMM Conference, 2012